A Study on Phased Array Feeds for Paraboloidal Reflector Antennas

by

Malan Anton Xander Ruppert

Thesis presented in partial fulfilment of the requirements for the degree of Master of Engineering (Electronic) in the Faculty of Engineering at Stellenbosch University

Supervisor: Prof. D.I.L. De Villiers
Co-supervisor: Dr. R.D. Beyers

December 2017

Declaration

By submitting this thesis electronically, I declare that the entirety of the work contained therein is my own, original work, that I am the sole author thereof (save to the extent explicitly otherwise stated), that reproduction and publication thereof by Stellenbosch University will not infringe any third party rights and that I have not previously in its entirety or in part submitted it for obtaining any qualification.

Date: .....December 2017.....

Abstract

This thesis presents a general study on the use and applications of paraboloidal reflectors utilizing a dense phased array feed (PAF), in the underlying context for use with a receiving Earth station antenna for satellite communication.

A theoretical treatment of fundamental concepts useful in the understanding and analysis of PAF system is given, including illustrative examples regarding focal field distribution sampling with an array antenna. The important topic of embedded element patterns, which plays a vital role in including mutual coupling effects in the analysis, is discussed in some detail.

A versatile linear numerical framework is created using accurate full-wave simulations and linear microwave-network equations, and combined into a convenient simulation model which can be used to perform various parameter studies on PAF systems. The model allows effects such as various front-end LNA parameters, and beamforming techniques to be investigated. The possibility of including passive array elements, or combining active elements, can also to be investigated.

The simulation model is applied to an example 15-element dipole PAF, and and a discussion is given on various results regarding beamsteering, optimal beamforming, and receiver noise matching.

The possibility of utilizing passive elements along with mutual coupling to reduce array receiver costs is investigated. It is found that more array elements are not always better, given the fact that element contributions to overall system noise outweigh their contribution to gain.

Finally, a detailed investigation is carried out on the various trade-off effects between different array configurations and system noise in the context of scanning in a single angular plane. A valuable result is obtained showing identical system SNR performance for arrays using either 9- or 45 elements.

Opsomming

Hierdie tesis bied 'n algemene ondersoek oor die gebruik en aanwending van paraboloiëde weerkaatser-antennas, wat gebruik maak van brandpuntvlaksamestelling (BFS) voer antennas, in die onderliggende konteks van die gebruik daarvan in 'n ontvanger grondstasie antenna vir satellietkommunikasie.

'n Teoretiese behandeling word gegee van die fundamentele begrippe wat nuttig is in die verstaan en analise van BFS stelsels, insluitende illustratiewe voorbeelde van die toetsing van die brandpuntverspreiding op so 'n weerkaatser-antenna. Die belangrike aspek van ingebedde element stralingspatrone, wat 'n belangrike rol speel om wedersydse koppeling tussen antennas te kan ondersoek, word ook bespreek.

'n Handige stel numeriese gereedskap word gegenereer met behulp van akkurate volgolf simulasies en liniêre mikrogolf netwerk vergelykings, en word gekombineer in 'n gerieflike simulasie model wat gebruik kan word om verskeie parameter studies op BFS stelsels uit te voer. Met die model kan verskillende aspekte soos 'n variasie van lae ruis versterker parameters, asook bundelvormingstegnieke ondersoek word. Die gebruik van passiewe elemente, of die geval van aktiewe elemente wat gekombineer word, kan ook ondersoek word.

Die simulasiemodel word toegepas op 'n 15-element dipool BFS stelsel as voorbeeld, en verskeie resulte soos bundelstuur en optimale bundelvorming word bespreek. 'n Voorbeeld van ontvanger ruis aanpassing word ook bespreek.

Die moontlike gebruik van passiewe elemente met wedersydse koppeling, met die doel om ontvanger kostes te verminder, word ondersoek. Die resultate wys dat meer elemente in 'n samestelling nie noodwendig beter is nie, aangesien sommige elemente se bydrae tot die algehele stelsel ruis meer beduidend is as hul bydrae tot antenna aanwins.

'n In-diepte ondersoek word gedoen oor die effek op stelsel ruis tussen verskillende samestelling modelle en hoeveelheid elemente, in die konteks van enkel vlak bundelstuur. 'n Waardevolle resultaat word aan die lig gebring wat identiese sein-tot-ruis verhouding aantoon vir samestellings van 9- en 45

elemente.

Acknowledgements

This study would be incomplete without expressing my gratitude towards the following people:

- My supervisors, Prof de Villiers and Dr Beyers, for their invaluable guidance and knowledge; thank you for keeping me on the right track and always putting things in perspective when I could find none.
- My parents, for always being supportive and allowing me to follow my own passions (and make my own mistakes!), while putting up with my inner-child.
- My brother, Carl, for always being so passionately interested in what I do.
- Anmarie, for her amazing friendship and support, always tolerating my strange ways.
- Everyone in E206, thanks for all the chats and support.
- VASTech, for their financial support, allowing the undertaking of this thesis.

Dedications

To my parents, Max & Annette.

Contents

List of Figures

List of Tables

Nomenclature & Notation

Constants

$k_b =$ 1.38×10^{-23} Boltzmann constant . . . . . $[\mathrm{JK}^{-1}]$
$\eta =$ 376.73 Freespace impedance . . . . . $[\Omega]$
$T_o =$ 290 Reference temperature . . . . . $[\mathrm{K}]$

Vector Notation and Matrix Operators

$\vec{\boldsymbol{f}}$ Field vector
$\hat{\mathbf{a}}$ hat, unit vector
$\mathbf{U}$ Identity matrix
$\mathbf{A}^T$ Transpose of $\mathbf{A}$
$\mathbf{A}^\dagger$ Conjugate transpose of $\mathbf{A}$

Abbreviations

BOR_1 Body of revolution type-1
CFM Conjugate field match
DBS Direct-broadcast satellites
DSP Digital signal processing
EEP Embedded element pattern
FFD Focal field distribution
FoV Field of view
GEO Geosynchronous Earth orbit
HPBW Half-power beamwidth
LNA Low noise amplifier
MLFMM Multi-level fast multipole method
MoM Method of Moments
PAF Phased array feed
PCS Personal communication satellites
SNR Signal-to-noise ratio

Chapter 1

Introduction

1.1 Phased Array Feeds for Reflectors

Reflector antennas utilizing single-element feeds are limited to radiating in a single direction at a given time, offering little capability in terms of beam-scanning other than mechanically displacing the feed or steering of the entire antenna structure. Alternatively, reflectors can be fed by an array of antennas, resulting in multiple highly directional beams. Conventional horn cluster feeds operate in a one-horn-per-beam manner [1], essentially creating a set of fixed beams, where as reflectors using densely spaced phased array feeds (PAF) utilize smaller array elements, typically spaced half-wavelengths apart. Each antenna element contributes to all radiation beams, essentially creating a 'radio-camera'. For a parabolic reflector shape, the result is a high gain system with steering capability within a small angular range.

While the use of a dense array antenna as a feed for a reflector is not a new concept [2, 3], recent interest in the technology's use for radio astronomy applications, primarily due to the possible instantaneous *field of view* (FoV), has seen a substantial influx of research efforts and contributions to the field [4]. Examples of current projects utilizing PAF for radio astronomy observations include the Australian Square Kilometer Array Pathfinder (ASKAP), consisting of low-profile checkerboard array feeds [5], and the APERture Tile In Focus (APERTIF) project in Netherlands, composed of broadband Vivaldi elements [6].

The versatility of beam-steering, increased FoV and beam-shaping provided by PAFs come at the cost of decreased sensitivity, as noise generated by receivers connected to each element couples to neighbouring elements, to eventually be amplified and correlated to the receiver output. Ohmic losses due to the large number of elements is also problematic [7]. The stringent sensitivity requirements for astronomical observations has therefore driven research groups

to develop accurate models of the effects of mutual coupling on system noise [8, 9].

1.2 Applications in Satellite Communications

Reflector antennas using feed arrays find their use in both the uplink and downlink side of satellite communication links. Multiple beam reflectors are currently being used for direct-broadcast satellites (DBS), personal communication satellites (PCS), as well as military and high-speed internet satellites [10]. Beamshaping capabilities of PAFs allow efficient use in radiated power by forming contoured spot-beams, also called footprints, in specific geographic areas. Efficient usage of available power is crucial to the ever increasing global demand of high-speed data and internet.

Earth station reflector antennas fitted with dense PAFs also offer several attractive applications and advantages over single feed systems. Beam steering allows the ability for a single Earth station to resolve several satellites simultaneously [11], avoiding scenarios of multiple single-dish-single-satellite connections [12]. In addition, while satellites in geostationary orbits (GEO) remain mostly stationary when viewed from Earth, small aberrations in position do occur, and beam steering can be used to maintain strong signal links. When incorporated with digital signal processing (DSP) techniques and hardware, PAFs provide rapid electronic reconfiguration of radiation beams, which allow antennas to adapt to changing signal and noise environments, and link fails. A study done in [13] has also shown the capability of PAFs in mitigating unwanted interferences, and could be used to increase the total capacity in a communications link.

1.3 About this Thesis

The underlying purpose of this thesis is to present an efficient and general numerical simulation framework for analysing phased array feed receiver systems, on which future projects can build. As the primary figure of merit for receiving systems is the achievable signal-to-noise ratio (SNR), rather than system gain, the simulation model requires the effects of receiver generated noise, external background noise, and antenna ohmic losses to be accurately modelled and understood.

Secondly, while not specifically focused on a single design, optimization or application of phased array feeds, some general applications of fitting an Earth

station paraboloidal reflector antenna with an array feed for satellite communications are investigated. These applications could include the ability to resolve several satellites along the geosynchronous Earth orbit simultaneously through beam steering, cancelling interference from unwanted signals, and beam shaping to provide broad radiation patterns while maintaining high gain.

The major contributions of this thesis are listed below:

- A versatile set of numerical tools which can be used to conduct various parameter studies of PAFs and array antennas in general. The developed model can be used to simulate and study the effects on receiver sensitivity due to different beamforming strategies, different LNA component parameters, as well as the effects of including passive elements or combining active elements. The numerical tools assume linear operation of the entire system.
- A comprehensive example showing some capabilities of paraboloidal reflector utilizing a PAF, using a 15-element dipole array model.
- Results of an initial attempt at reducing array feed receiver costs by utilizing passive elements.
- A detailed study on the various trade-off effects between array size, receiver noise, and receiver topology in order to determine the optimal number of elements for beamsteering in a single angular plane.

1.4 Layout of Thesis

The thesis begins in Chapter 2 with an overview of the general theory and concepts useful in understanding and analysing PAF systems. Specific attention is given to the concept of embedded element patterns, which plays a vital role in including the effects of mutual coupling between array elements in the analysis, as well as the system characterisation of array receivers in terms of G/T.

Chapter 3 focuses on the simulation and modelling of PAFs. Various simulation strategies are discussed for array and reflector antennas, and an efficient simulation procedure is described. It is shown how full-wave simulation results can be used to obtain an accurate array receiver network model, and details are given on the modelling of various noise contributions at the receiver output. Some examples using the developed numerical simulation model are shown using a 15-element dipole PAF as prototype.

Chapter 4 explores the possibility of reducing array receiver costs by utilizing passive elements. An important observation is made that more array elements are not always preferable, as the increase in receiver noise caused by a large number of receiver chains could dominate the overall system sensitivity.

Chapter 5 follows up on the results from Chapter 4 by conducting a study on the optimal number of elements for scanning in a one-dimensional plane. A detailed discussion is presented regarding the various trade-off effects between system gain and overall noise temperature.

The thesis concludes in Chapter 6 with a summary of the main results, and recommendations for future work.

Chapter 2

Theoretical Framework

This chapter outlines some theoretical concepts useful in the understanding and analysis of *phased array feeds* (PAF) for paraboloidal reflectors. General antenna terms and notations used throughout the thesis are discussed in Section 2.1. Section 2.2 gives a brief account on the theory of prime-focus paraboloidal reflector antennas, including the definition of aperture efficiency for aperture antennas. Since the thesis is primarily focused on an receiving antenna, a discussion on the general forms of the field distributions scattered by a paraboloidal reflector due to incident plane waves is also included. Section 2.3 presents general expressions important in array antenna theory, followed by a numerical example of an array antenna when used as a feed for a paraboloidal reflector. Section 2.4 includes a discussion on the important concept of embedded elements patterns, which is critical in accurately modelling mutual coupling effects between array elements. Array signal processing and beamforming concepts are addressed in Section 2.5, and the definition of conjugate field match and optimal noise performance beamforming weights are given. Finally, the G/T_{sys} figure of merit for receiving antennas is discussed in Section 2.6.

2.1 General Antenna Terms and Notation

This section briefly covers some notation used throughout the thesis. The radiated electric fields observed at a distance r in the far-field region of any general antenna isolated in freespace can be expressed in the separable form

$$\vec{\boldsymbol{E}}(\theta,\phi) = \frac{e^{-jkr}}{r}\vec{\boldsymbol{f}}(\theta,\phi), \tag{2.1}$$

where k is the *wavenumber* defined as

$$k = \frac{2\pi}{\lambda}. \tag{2.2}$$

with λ the wavelength of the frequency of interest. All field vectors in this thesis are denoted by arrows $\vec{\cdot}$. The field vector $\vec{\boldsymbol{f}}(\theta, \phi)$ will be called the far-field radiation pattern, or just radiation pattern, throughout the thesis. When considering the far-field radiation patterns the radial dependence of the electric field (e^{jkr}/r) can be dropped, and only the direction dependent radiation patterns $\vec{\boldsymbol{f}}(\hat{\mathbf{r}})$ need to be considered.

The *radiation intensity* $U(\theta, \phi)$, defined as the radiated power per unit solid angle, is

$$U(\theta, \phi) = \frac{1}{2\eta} |\vec{\boldsymbol{f}}(\theta, \phi)|^2. \tag{2.3}$$

The total power radiated by the antenna P_{rad} can thus be expressed as the integration of (2.3) over all angles

$$P_{\text{rad}} = \frac{1}{2\eta} \iint_{\Omega_o} |\vec{\boldsymbol{f}}(\theta, \phi)|^2 d\Omega_o \tag{2.4}$$

where Ω_o is a short-hand notation for (θ, ϕ). The antenna directivity D_o, usually expressed in dBi, is obtained as

$$D_o = 10 \log_{10} \left(\frac{4\pi U(\theta, \phi)}{P_{\text{rad}}} \right) \tag{2.5}$$

2.2 Paraboloidal Reflector

The goal of this section is to cover some paraboloidal reflector antenna theory in the context of PAFs, and is based mostly on [14].

2.2.1 Geometry

Consider the side view of a rotationally symmetric paraboloidal reflector in Figure 2.1. Two coordinate systems, (x_f, y_f, z_f) and (x, y, z), both coinciding with the reflector focal point, are assigned to the configuration, with $\hat{\mathbf{z}}_f$ pointing towards the reflector vertex, and $\hat{\mathbf{z}}$ coinciding with the reflector's boresight radiation direction, implying that $\hat{\mathbf{z}}_f = -\hat{\mathbf{z}}$, $\hat{\mathbf{x}}_f = -\hat{\mathbf{x}}$, and $\hat{\mathbf{y}}_f = \hat{\mathbf{y}}$ (not shown in Figure 2.1). These coordinate systems will be used throughout the thesis to separate analyses in terms of the feed or reflector coordinate systems. The paraboloidal profile is described by

$$\mathbf{r}_s(\theta_f, \phi_f) = \frac{2F}{1 + \cos\theta_f} \hat{\mathbf{r}}_f, \qquad \text{for} \begin{cases} 0 < \theta_f < \theta_o \\ 0 < \phi_f < 2\pi \end{cases}, \tag{2.6}$$

where F is the *focal length*, and the angle θ_o, termed the *subtended half-angle*, is measured from the reflector vertex to its rim. Since a rotationally symmetric

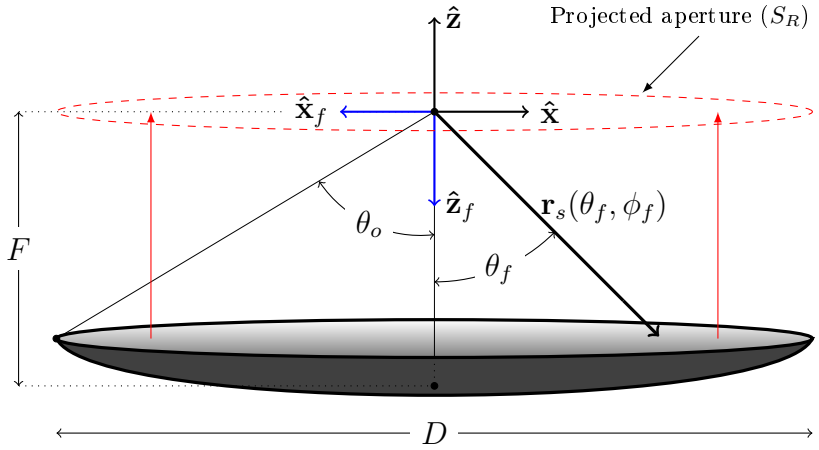

Figure 2.1: Rotationally symmetric paraboloidal reflector geometry

case is considered here, equation (2.6) is valid for a full rotation of ϕ_f. Used together with the reflector *diameter* D, F and θ_o can be used to specify any paraboloidal reflector shape and size. These variables are related according to

$$D = 4F\tan(\theta_o/2). \tag{2.7}$$

Common practice is to use D and the ratio F/D as the reflector specification variables, and typical values of F/D for radio frequency reflectors range from 0.25 to 1.

2.2.2 Directivity and Aperture Efficiency

Reflector antennas are classified as aperture-type antennas, since the projected area of the dish can be viewed as an equivalent aperture S_R in free-space, The maximum achievable directivity (standard, or reference directivity [15]) of a large aperture is known to be [14]

$$D_{o,(\max)} = \frac{4\pi A}{\lambda^2}, \tag{2.8}$$

where A is the physical aperture area. For a paraboloidal reflector, the projected area of the dish can be viewed as an equivalent aperture S_R in free-space, since most of the radiated energy passes through its surface. In this case the aperture area can be given in terms of the reflector diameter D as

$$A = \pi\left(\frac{D}{2}\right)^2. \tag{2.9}$$

A feed antenna radiating an electric field $\vec{\boldsymbol{E}}_f$ placed in front of the reflector in Figure 2.1, with its phase centre coinciding with the coordinate origin, is used to illuminate the dish. To achieve the maximum directivity of (2.8) with

the feed and reflector, the illumination must be such that *all* the radiated feed power is reflected, and that the electromagnetic fields scattered across the projected reflector aperture S_R be uniform with constant phase. This is physically impossible for feed and reflectors of finite electrical size, and the loss of directivity is quantified by the antenna *aperture efficiency* [15],

$$\eta_{ap} = \frac{D_o}{D_{o,(\max)}}, \tag{2.10}$$

where D_o is the actual obtained directivity in the direction of maximum radiation. The aperture efficiency can further be partitioned into various sub-efficiencies [16, 17], although care must be taken when using these from various authors[1].

Here, three sub-efficiencies are briefly discussed, the first being the *spillover efficiency* η_{sp}, defined as the ratio of radiated feed power incident on the reflector to that of the total radiated feed power,

$$\eta_{sp} = \frac{\iint_{\Omega_{\theta_o}} |\vec{\boldsymbol{f}}_f(\theta_f, \phi_f)|^2 d\Omega_{\theta_o}}{\iint_{\Omega_o} |\vec{\boldsymbol{f}}_f(\theta_f, \phi_f)|^2 d\Omega_o} \tag{2.11}$$

where Ω_o is a short-hand notation for (θ, ϕ) direction, and Ω_{θ_o} indicates the angular region spanned by the reflector. Equation (2.11) includes both co- and cross-polarizations. The spill-over efficiency should be minimized to avoid wasted feed power in the transmit case, and to reduce warm background noise received by the feed in the receive case.

Second is the *illumination efficiency* η_{ill}, which accounts for the loss of directivity due to non-uniform amplitude *and* phase illumination of the reflector aperture S_R. From Figure 2.1, with the aperture fields across S_R denoted by $\vec{\boldsymbol{E}}_{S_R}$, η_{ill} is,

$$\eta_{ill} = \frac{1}{A} \frac{\left| \iint_{S_R} \left[\vec{\boldsymbol{E}}_{S_R}(x, y) \cdot \hat{\mathbf{co}} \right] dS_R \right|^2}{\iint_{S_R} |\vec{\boldsymbol{E}}_{S_R}(x, y) \cdot \hat{\mathbf{co}}|^2 dS_R} \tag{2.12}$$

and includes only the desired co-polar component.

Finally, the *polarisation efficiency* η_{pol} accounts for losses due to undesired

[1] In the literature there are different naming conventions for various sub-efficiencies, and cases where different authors use similar names to mean different things. Readers can refer to [18] for an interesting discussion on this topic.

cross-polarisation contributions as,

$$\eta_{pol} = \frac{\iint_{S_R} \left| \vec{\boldsymbol{E}}_{S_R}(x,y) \cdot \hat{\mathbf{co}} \right|^2 dS_R}{\iint_{S_R} |\vec{\boldsymbol{E}}_{S_R}(x,y)|^2 dS_R} \tag{2.13}$$

Used together, the product of (2.11), (2.12) and (2.13) form the aperture efficiency,

$$\eta_{ap} = \eta_{sp}\eta_{ill}\eta_{pol} \tag{2.14}$$

The sub-efficiencies are useful for detailed feed design, for example when trying to determine the culprits of inefficient radiation or performance. However, for most of this thesis it is sufficient to work mainly with η_{ap} directly, and to consider η_{sp} when investigating spill-over noise. The aperture efficiency will briefly be investigated by using analytical feed patterns in the following section.

Analytical Feed Study

As a brief example, some analytical feed radiation patterns can be considered of the following form,

$$\vec{\boldsymbol{E}}_f = \frac{e^{-jkr}}{r}\vec{\boldsymbol{f}}_f(\theta_f, \phi_f),$$
$$\text{where} \qquad \vec{\boldsymbol{f}}_f(\theta_f, \phi_f) = f_E(\theta_f)\sin\phi_f\hat{\boldsymbol{\theta}}_f + f_H(\theta_f)\cos\phi_f\hat{\boldsymbol{\phi}}_f. \tag{2.15}$$

Equation (2.15) can be labelled as a $\hat{\mathbf{y}}$-polarised *body-of-revolution* radiation pattern of type 1 (BOR_1) [14], and it is convenient analytically since only the E- and H-plane patterns[2] are required to fully specify the total radiation pattern. Figure 2.2 shows some feed patterns of the form,

$$f_E(\theta_f) = f_H(\theta_f) = \cos^n(\theta_f/2). \tag{2.16}$$

Increasing the factor n in (2.16) results in narrower feed patterns. The three vertical lines in Figure 2.2 indicate subtended half angles θ_o for F/D ratios 0.3, 0.4 and 0.5, and the different sub-efficiencies are shown in Figure 2.3 as a function of n for these same F/D ratios. Evidently, broader feed patterns result in more efficient illumination of the reflector aperture, at the cost of increased spill-over power, and lower spill-over efficiency. This trade-off gives rise to an optimal aperture efficiency typically between $70-80\%$, which is quite a well-known result [14, 19]. Note that the polarisation efficiency is unity in all cases due the completely symmetrical patterns [14].

[2]Linear y-polarised co-polar antennas are used throughout the thesis, and the E- and H-planes correspond to $\phi = 90°$ and $\phi = 0°$ planes, respectively.

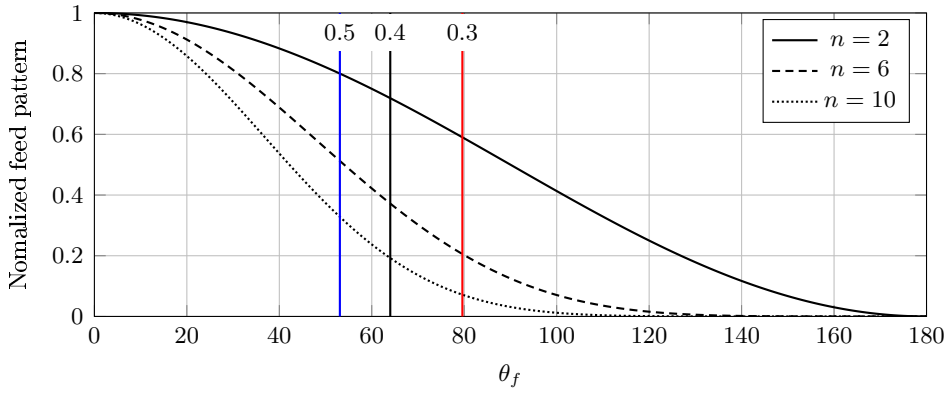

Figure 2.2: Normalized feed radiation patterns of the form $\cos^n(\theta_f/2)$

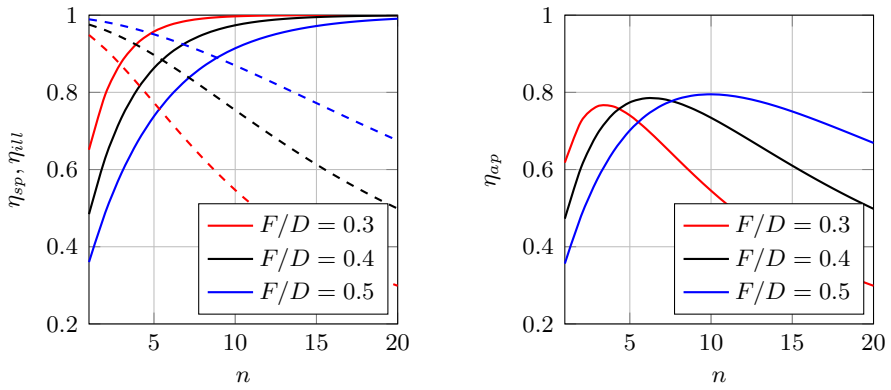

(a) Spill-over (solid) and illumination (dashed) efficiencies.

(b) Aperture efficiency

Figure 2.3: Various efficiencies resulting from feed patterns of the form $\cos^n(\theta_f/2)$, as a function of n.

Out of interest, it can been shown that an aperture efficiency $\eta_{ap} = 1$ can be obtained with a feed pattern of the form [20],

$$f_E(\theta_f) = f_E(\theta_f) = \begin{cases} \sec^2(\theta_f/2), & 0 \leq \theta_f \leq \theta_o \\ 0, & \theta_f \geq \theta_o \end{cases} \tag{2.17}$$

which has a sharp cut-off at the reflector rim where $\theta_f = \theta_o$. Illustrations of the above mentioned feed patterns are shown in Figure 2.4, where the dotted black line indicates the reflector rim for $F/D = 0.4$ as seen from the feed coordinate system, meaning all radiation seen below the line is intercepted by the reflector. Note the sharp cut-off exactly at the reflector rim in Figure 2.4d for the $\sec^2(\theta_f/2)$ radiation pattern.

The feed patters from Figure 2.4 were applied as equivalent point sources to a reflector with parameters $D = 100\lambda$ and $F/D = 0.4$ in FEKO [], and the re-

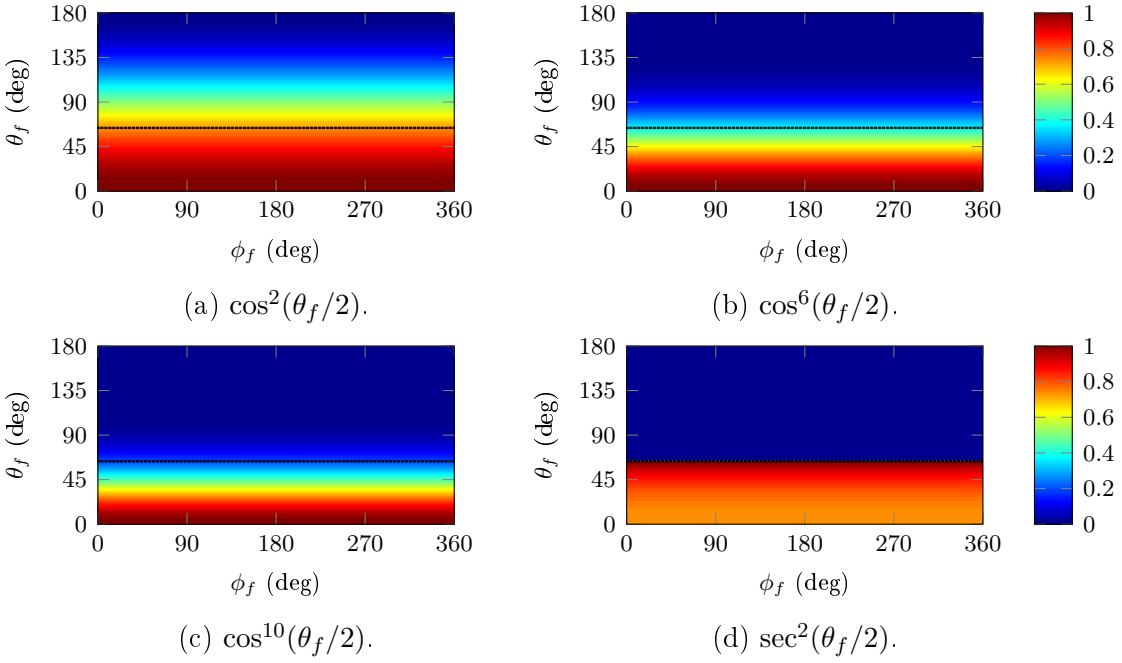

(a) $\cos^2(\theta_f/2)$. (b) $\cos^6(\theta_f/2)$.

(c) $\cos^{10}(\theta_f/2)$. (d) $\sec^2(\theta_f/2)$.

Figure 2.4: Various normalized feed patterns, with dotted black line indicating reflector rim as seen from the feed coordinate system.

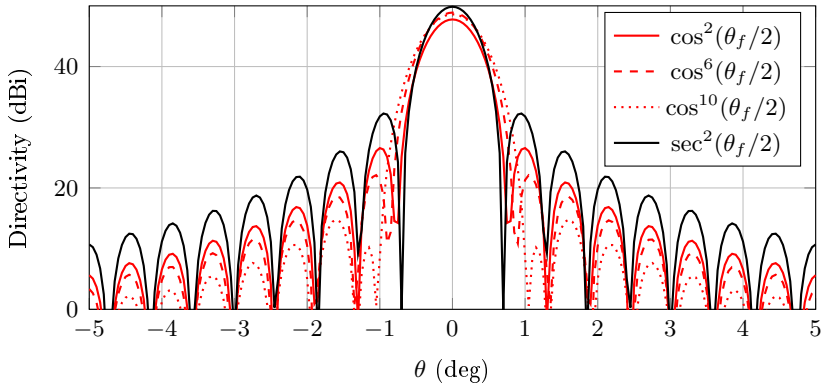

Figure 2.5: Directivity achieved for ($\phi = 0$) of the radiation patterns from Figure 2.4 for a reflector with $D = 100\lambda$ and $F/D = 0.4$.

sulting directivity calculated using PO solver is shown in Figure 2.5. As can be seen, the directivity from the $\sec^2(\theta_f/2)$ pattern is $D_o = D_{o,(\max)} = 49.9$ dBi, with a relative sidelobe level of around -17.6 dB, which is a known result for a uniformly excited circular aperture [14, Chapter 7] [20]. The best performing $\cos^n$ radiation pattern, in terms of directivity, has $n = 6$, followed closely by $n = 10$ which has a somewhat broader beam, but with lower side-lobes due to the narrower illumination of the reflector aperture.

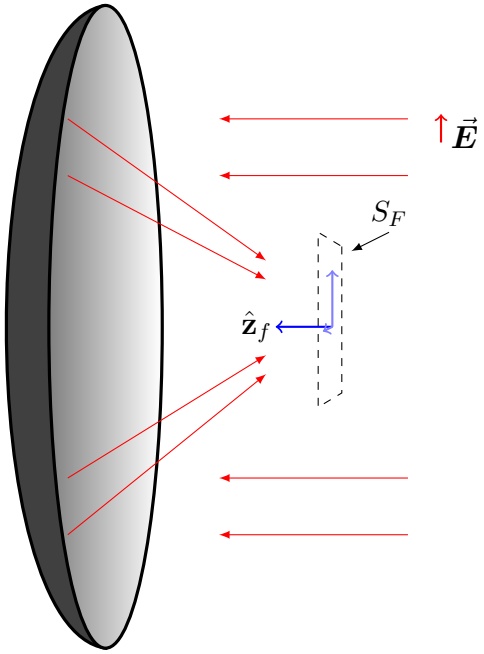

Figure 2.6: Paraboloidal reflector receiving an incident plane wave

2.2.3 Focal Field Distributions for Incident Plane Waves

Considering some plane-wave $\vec{\boldsymbol{E}}$ incident on the reflector as shown in Figure 2.6, it is of interest to know the electric and magnetic *focal field distributions* (FFD) scattered in the focal plane aperture S_F of the paraboloidal reflector, since this is typically where the feed is located. From Figures 2.1 and 2.6, S_F coincides with the (x_f, y_f) plane at $z_f = 0$.

Analytical expressions for the FFD are quite cumbersome, but examples can be found in the literature [21, 22]. Here, FEKO [23] has been used to simulate plane-waves incident on a reflector using *physical optics* [14], and the resulting electric field distribution $\vec{\boldsymbol{E}}_{S_F}$ in the focal plane obtained are obtained

$$\vec{\boldsymbol{E}}_{S_F}(x_f, y_f) = E_x(x_f, y_f)\hat{\mathbf{x}}_f + E_y(x_f, y_f)\hat{\mathbf{y}}_f + E_z(x_f, y_f)\hat{\mathbf{z}}_f. \tag{2.18}$$

As will be shown in the next section, the FFD of $\vec{\boldsymbol{E}}_{S_F}$ in S_F takes the general form of an Airy-like pattern [21]; that is, the distribution consists of a centre main lobe, surrounded by concentric rings of decreasing amplitude. On-axis- and oblique incident plane-waves will be discussed.

On-axis incident plane wave

The electric field components of (2.18) due to a normally incident $\hat{\mathbf{y}}$ polarised plane-wave ($-\hat{\mathbf{z}}$ propagation direction in the case of Figure 2.1) on a reflector

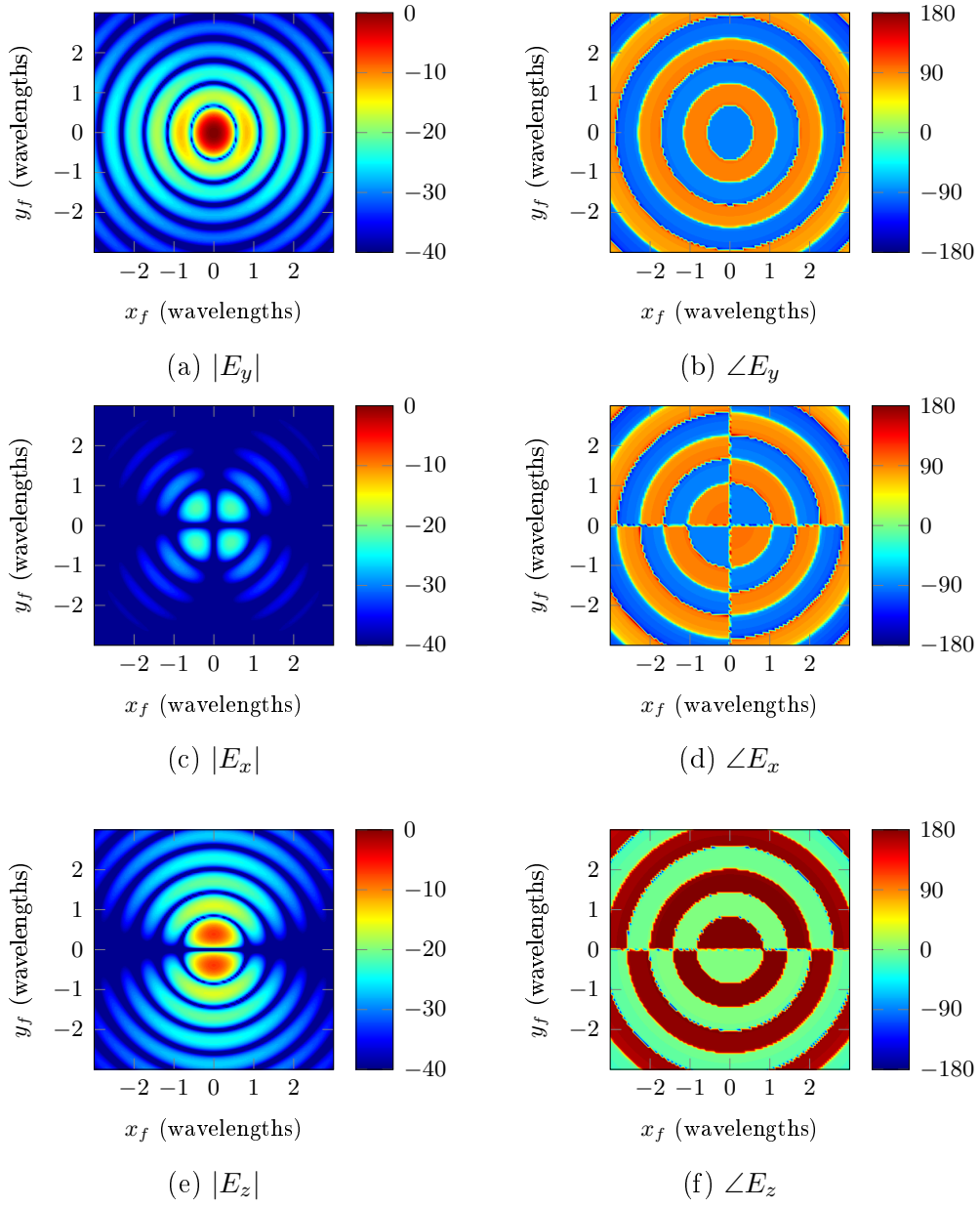

(a) $|E_y|$ (b) $\angle E_y$

(c) $|E_x|$ (d) $\angle E_x$

(e) $|E_z|$ (f) $\angle E_z$

Figure 2.7: Electric field components (magnitude and phase) for on-axis plane wave for $F/D = 0.4$. Magnitudes are normalized to $|E_y(0,0)|$.

with $D = 100\lambda$ and $F/D = 0.4$ are plotted in Figure 2.7 in dB-scale. The E_y component follows the above mentioned Airy-like pattern, consisting of a main-lobe, with concentric side-lobe rings and alternating phase, and is generally the desired component. Also present is a relatively small cross-polar E_x field component (Figure 2.7c), which has a null in the centre, and maximums along $\pm 45°$ planes. Also, notice the non-zero E_z component in Figure 2.7e, causing some of the non-rotational symmetry in E_y. With all components combined, the FFD is seen to be completely co-polar in the centre.

Off-axis incident plane wave

To illustrate the effect of plane waves incident on the reflector from oblique angles, Figure 2.8 shows the electric fields components from (2.18) for a y-polarised plane wave incident at an off-axis angle of $1.4°$ on the same $D = 100\lambda$ and $F/D = 0.4$ reflector as before. The FFD shifts along the focal plane, and although the different components retain their general shape, there is some distortion and increased side-lobes in the direction of the shift.

It has been shown [24] that the physical distance of the Airy-pattern shift can remain somewhat independent on the reflector diameter D when considering incident angles in terms of half-power beamwidths (HPBW), where one HPBW $= 70D/\lambda$ (deg), up to roughly 7-HPBW, and increasing D only adds a scaling factor to all components. Thus, the $1.4°$ results illustrated in Figure 2.8 correspond to $\approx$ 2HPBW for $D = 100\lambda$. Note that for a plane-wave incident from $\hat{\mathbf{x}}$ direction, the FFD shifts in the $\hat{\mathbf{x}}_f$ direction.

This purpose of this section has illustrated some general characteristics of the electric FFD for a paraboloidal reflector receiving some incident plane wave. The key results are knowing the general forms of the FFD components, and realizing that these components shift across the reflector focal plane as the incident signal angles shifts off-axis. Knowledge of the FFD will be used in Section 2.3 to determine the required excitations for the elements of an array antenna acting as a reflector feed.

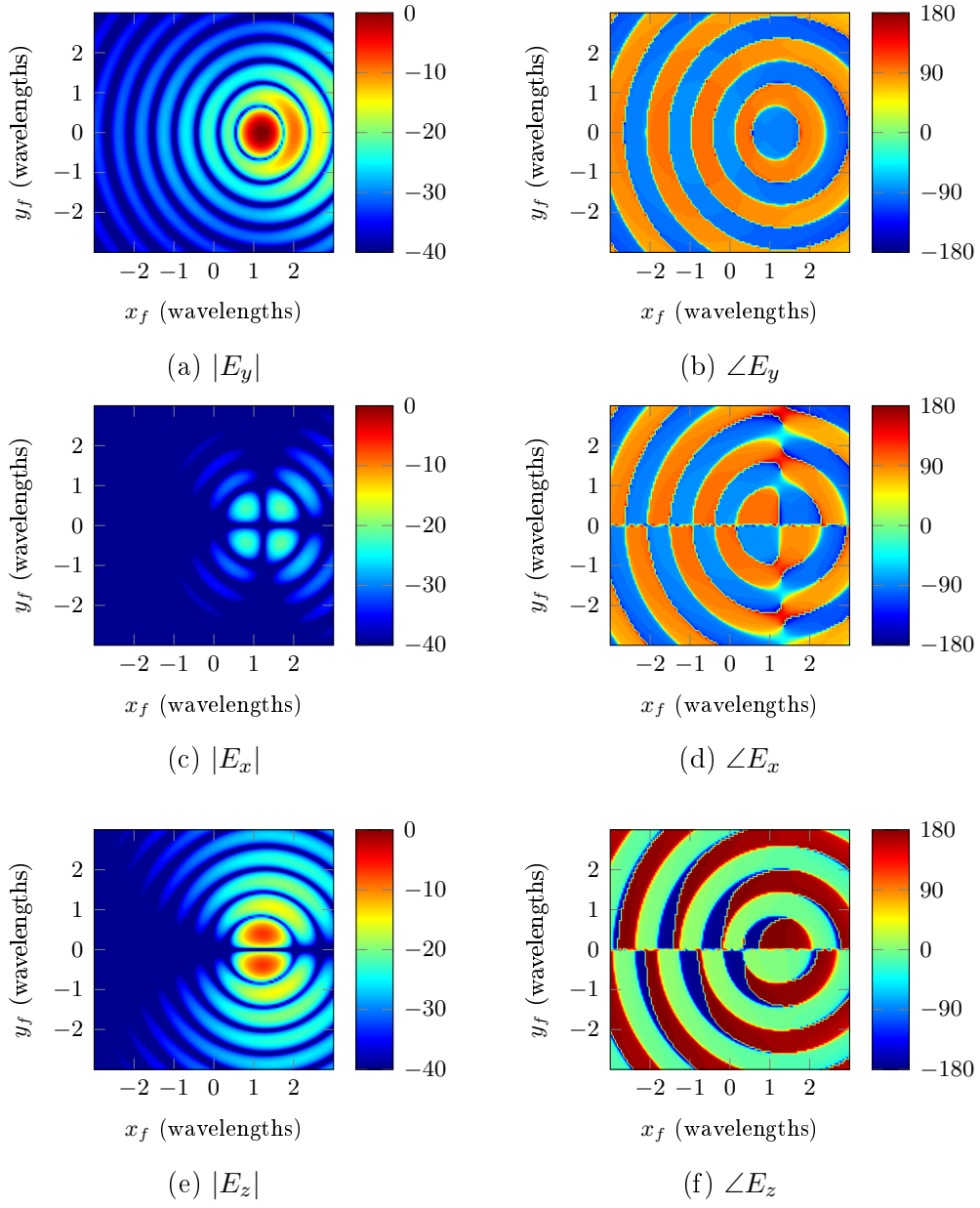

(a) $|E_y|$ (b) $\angle E_y$

(c) $|E_x|$ (d) $\angle E_x$

(e) $|E_z|$ (f) $\angle E_z$

Figure 2.8: Normalized electric field component E_y for 1.4 degrees off-axis plane wave.

2.3 Array Antenna Theory

This section is dedicated to some array antenna theory. Section 2.3.1 covers some general array concepts such as array factor and pattern multiplication. In Section 2.3.2 an example is given showing how a PAF is used to 'sample' the FFD from Section 2.2.3 for efficient radiation and reception.

2.3.1 Array Factor

An antenna array is a collection of antennas, typically spaced closely, and operated together in some desired way. Each antenna in the array is referred to as an *element*. The *array factor* (AF) plays an important role in array antenna theory. The IEEE definition of the array factor reads [15]:

> *The radiation pattern of an array antenna when each array element is considered to radiate isotropically.*

An example of a rectangular planar array consisting of isotropic point sources, lying in the (x_f, y_f) plane, is shown in Figure 2.9. Assuming some relative weighted excitation w_n of each isotropic element n, the array factor is expressed as [14],

$$\mathrm{AF}(\hat{\mathbf{r}}) = \sum_{n=1}^{N_x N_y} w_n e^{jk\mathbf{r}_n \cdot \hat{\mathbf{r}}}, \tag{2.19}$$

where generally $w_n = \alpha_n e^{j\beta_n}$ is a complex quantity. The vector $\mathbf{r}_n$ indicates the position of element n. In the planar case of Figure 2.9, with $\mathbf{r}_n = x_n\hat{\mathbf{x}}_f + y_n\hat{\mathbf{y}}_f$, and by introducing a matrix notation, (2.19) can be expressed as,

$$\mathrm{AF}(\hat{\mathbf{r}}) = \mathrm{AF}(\theta, \phi) = \mathbf{w}^T\mathbf{a}(\theta, \phi) \tag{2.20}$$

where the vector $\mathbf{a} \in \mathbb{C}^{N_x N_y \times 1}$ contains the elements,

$$\mathbf{a}(\theta, \phi) = \begin{bmatrix} e^{jk(x_1 \sin\theta\cos\phi + y_1 \sin\theta\sin\phi)} \\ e^{jk(x_2 \sin\theta\cos\phi + y_2 \sin\theta\sin\phi)} \\ \vdots \\ e^{jk(x_N \sin\theta\cos\phi + y_N \sin\theta\sin\phi)} \end{bmatrix}. \tag{2.21}$$

If it can be assumed that all array elements have identical radiation patterns $\vec{\boldsymbol{f}}_{elem}$, the total array radiation can be expressed as

$$\vec{\boldsymbol{f}}_{feed} = \vec{\boldsymbol{f}}_{elem}\mathrm{AF}(\theta, \phi), \tag{2.22}$$

a result typically referred to as *pattern multiplication*. It is a convenient model, especially for array synthesis since the array geometry and excitation information is fully encapsulated only in the AF. Equation (2.22) neglects the effect of mutual coupling, which is discussed in Section 2.4. The following section discusses array antennas in the context of their use as feed for a paraboloidal reflector antenna.

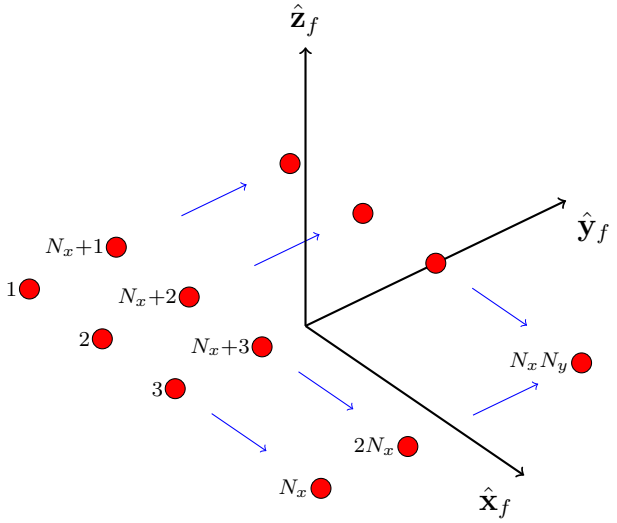

Figure 2.9: Planar array layout and indexing scheme

2.3.2 Array Excitation of Sampled Focal-Plane-Aperture

The discussion on array antennas here is focused on their use as feeds for reflectors, and thus there are some differences from classical phased array antenna theory. Roughly speaking, the array feed is required to 'mimic' the amplitude and phase of the Airy-like FFDs presented in the previous section, for efficient radiation and reception. Thus, the concept of amplitude tapering and progressive linear phasing between elements to control side-lobe levels and scanning, which is commonly applied in classical phased arrays, is not of much use in this context.

As an example, consider a theoretical array feed for which all elements have radiation patterns according to

$$\vec{\boldsymbol{f}}_{elem} = \cos(\theta/2)^2[\sin\phi\hat{\boldsymbol{\theta}} + \cos\phi\hat{\boldsymbol{\phi}}], \tag{2.23}$$

which is of the same BOR_1 type considered in (2.16). The array factor is defined according to (2.20) and laid out as in Figure 2.9. The excitation weights w_n are obtained by sampling the E_y-component of the electric FFD from Section 2.2.3 at the location of array elements, and taking its conjugate,

$$w_n = \delta(x_f - x_n, y_f - y_n)\vec{\boldsymbol{E}}^*_{S_F}(x_f, y_f). \tag{2.24}$$

The resulting feed radiation pattern is then obtained using (2.22). Figure 2.10 shows $|E_y(x_f, y_f)|$ along with the sampled points for array feeds of sizes (3×3), (5×5), (7×7), and (9×9) with $\lambda/2$ element spacing in all cases. The resulting feed radiation patterns are shown in Figure 2.11. As expected, the patterns

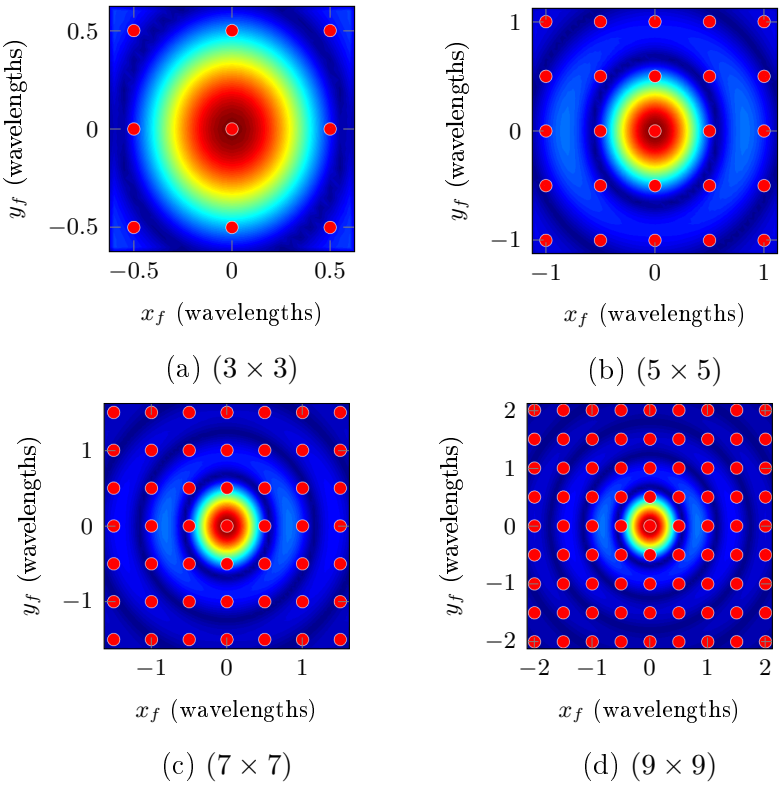

Figure 2.10: Illustration of sampling locations for on-axis radiation with array feed.

seem to approach a $\sec^2(\theta_f/2)$ form similar to (2.17) as the focal plane is sampled more completely. This is due to the on-axis plane wave excitation being the receive equivalent of the maximal on-axis gain for a transmitting case. The finite size of the reflector results in FFDs of an infinite extent, wheras an infinite reflector (the Geometric Optics limit) would result in a delta function point FFD. One could perhaps reason that sampling the focal plane aperture to infinity could approach a perfect η_{ap}, although feed blockage would certainly become a problem in this case.

Shown in Figure 2.12 is the resulting achieved directivity when applying the feed patterns from Figure 2.11 to the same $D = 100\lambda$ and $F/D = 0.4$ reflector used in Section 2.2.2. As expected, larger feeds results in narrower radiation patterns and increased directivity, although the effects thereof become less noticeable beyond (7×7) array size. This illustrates a priority of resolving the FFD main-lobe and first side-lobe, but shows that the benefits of increasing the array size would, beyond some point, diminish.

In terms of scanning performance, Figure 2.13 shows the FFD and (7×7) array element sampling locations in the case of 1- and 3-BW off-axis incident

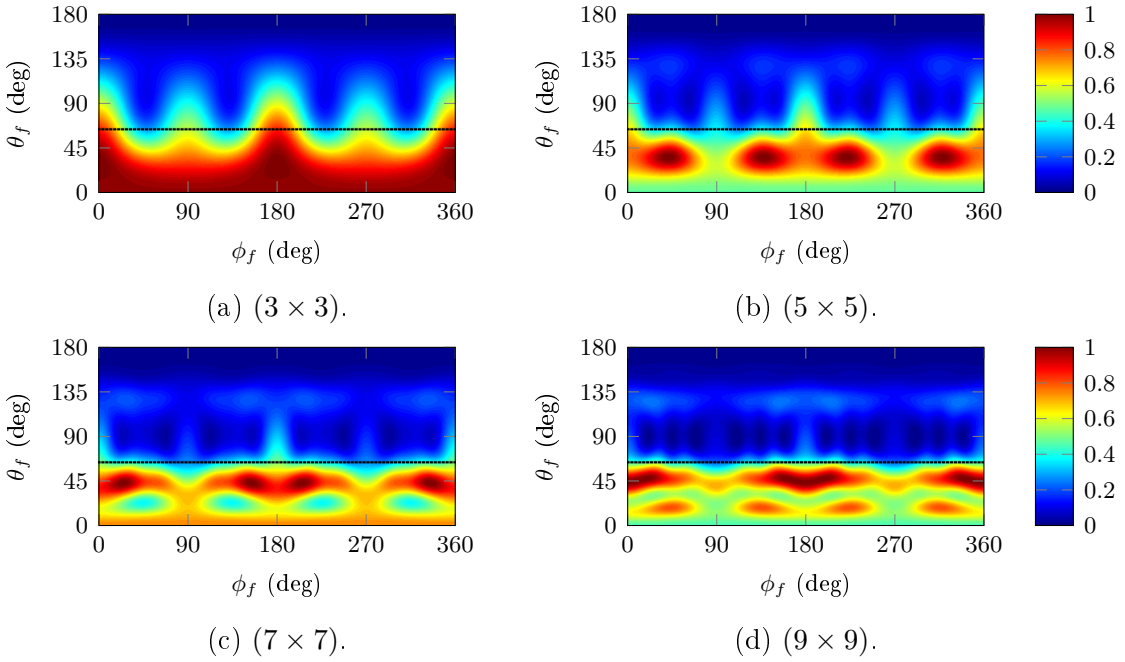

(a) (3×3). (b) (5×5).

(c) (7×7). (d) (9×9).

Figure 2.11: Resulting normalized radiation patterns achieved with theoretical array feed for on-axis radiation.

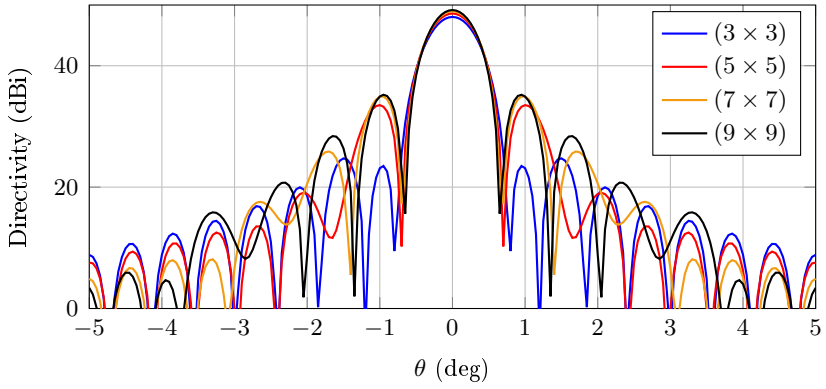

Figure 2.12: Achieved directivity from sampling focal plane for on-axis radiation and $D = 100\lambda$, $F/D = 0.4$.

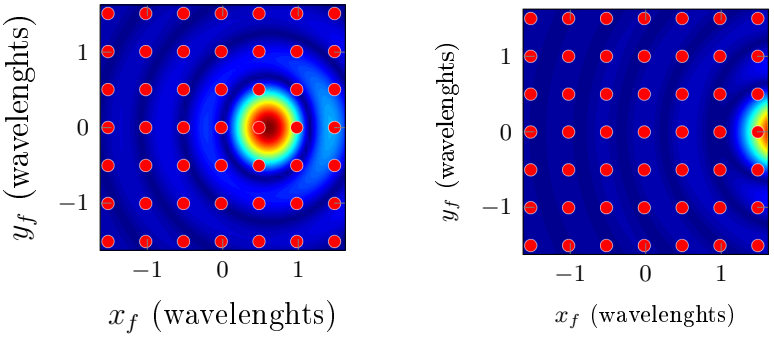

(a) 1-BW incidence (b) 3-BW incidence

Figure 2.13: Element sampling locations for 1-BW and 3-BW radiation with (7×7) array feed.

plane waves. For $D = 100\lambda$, the incident angles correspond to 0.7° and 2.1° off-axis respectively. In the case of 1-BW, the array size is able to fully resolve the FFD main-lobe, as well as the first side-lobe distortion. However, the case of 3-BW off-axis shows the main-lobe being only partially resolved. The resulting directivity for these two cases is shown in Figure 2.14. As expected, the excitation from Figure 2.13a results in a desired 0.7° radiation direction, where as radiation to 2.1° (3-BW) from sampling in Figure 2.13b is not entirely possible, as the array size is insufficient in fully resolving the complete shifted Airy-pattern. This example shows how the array size imposes a limit on the available scan range.

There are several factors have not been discussed here, such as the effects of different reflector shapes and element spacing. However, the present section has mainly been included to illustrate the concept of sampling the FFD with an array feed, and to show that the required element excitation for efficient radiation and reception generally follows FFD magnitude and phases. Element spacings of $\lambda/2$ will always be considered in this thesis, since it is desired to obtain continuous performance across an angular region of interest[3]. For the interested reader, more comprehensive studies on the effects of F/D ratios and densely spaced arrays for on- and off-axis scanning can be found in [25, 10].

[3]Larger element spacings ($\geq \lambda$), for example in the case feed horn clusters mentioned in Section 1.1, would lead to performance 'dips' across the scan-able angular region, as the FFDs crosses points inefficiently sampled by array elements.

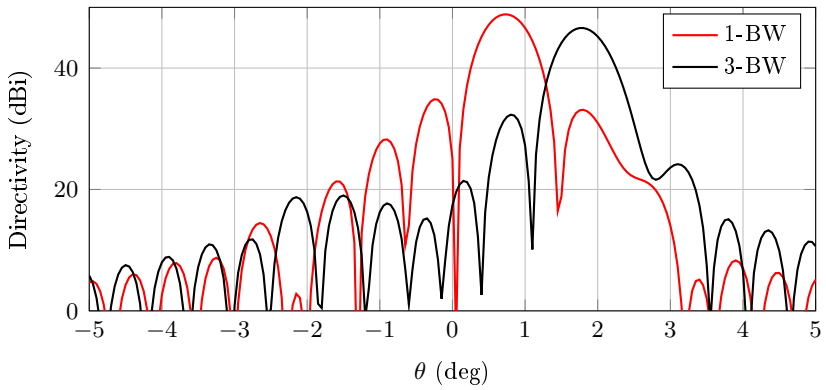

Figure 2.14: Achieved directivity in $\phi = 0$ for 1-BW and 3-BW radiation with array feed for $D = 100\lambda$, $F/D = 0.4$.

2.4 Mutual Coupling and Embedded Element Patterns

Prior to this section, the effects of mutual coupling among array elements have been ignored. The reality is that each array element generally experiences different boundary conditions from that of others, which leads to changes in the radiation pattern, input impedance, and overall performance of that element compared to when it is considered in isolation.

A convenient way to account for mutual coupling among array elements in an analysis is to work with what is known as *embedded element patterns*, which is mainly the subject of this section. The discussion here is mostly a duplicate of that found in [26, Section 2], and is included mainly for the purpose of convenience to the reader, as it is an important concept present throughout the thesis.

2.4.1 Definition of Embedded Environments

Consider the configuration in Figure 2.15, which shows an N element array antenna, along with generators represented by Norton equivalent circuits attached to each element port. The discussion to follow is valid as long as it can be assumed that the antenna array ports are defined at some point where single-mode voltages and currents can be defined, and that the coupling matrix is symmetric i.e. reciprocal. It is convenient to present some fixed definitions for the discussion to follow. The definitions below apply to any element $n \in \{1, 2, ..N\}$ of the array under consideration:

Embedded element pattern (EEP): The radiation pattern of element n achieved with a Norton equivalent source I_n^S of unit current at ele-

ment n with all other elements passively terminated with their generator impedances:

$$\vec{\boldsymbol{E}}_n^{e,Nrt}(\mathbf{r}) = \frac{e^{-jkr}}{r}\vec{\boldsymbol{f}}_n^{e,Nrt}(\hat{\mathbf{r}})I_n^S. \tag{2.25}$$

Short-circuit embedded element pattern (SC-EEP): The radiation pattern of element n, with unit voltage V_n supplied to port n, and zero voltage at all other ports:

$$\vec{\boldsymbol{E}}_n^{sc}(\mathbf{r}) = \frac{e^{-jkr}}{r}\vec{\boldsymbol{f}}_n^{sc}(\hat{\mathbf{r}})V_n. \tag{2.26}$$

Open-circuit embedded element pattern (OC-EEP): The radiation pattern of element n, with unit current I_n supplied to port n, and zero currents at all other ports:

$$\vec{\boldsymbol{E}}_n^{oc}(\mathbf{r}) = \frac{e^{-jkr}}{r}\vec{\boldsymbol{f}}_n^{oc}(\hat{\mathbf{r}})I_n. \tag{2.27}$$

When considering the far-field radiation patterns the radial dependence of the electric field (e^{jkr}/r) can be dropped, and only the direction dependent radiation patterns $\vec{\boldsymbol{f}}(\hat{\mathbf{r}})$ need to be considered.

While many works have devoted attention to the OC-EEPs using an impedance formulation, the focus in Section 2.4.2 is on the SC-EEPs and an admittance representation, the main reasons being that: 1) SC-EEP descriptions are uncommon in the literature 2) it is, in some cases, more convenient to work with port voltages and short circuits in numerical tools[4]. In Section 2.4.3 a relationship is provided between the open- and short-circuit cases.

2.4.2 Short-Circuit Embedded Element Patterns

Since the short-circuited case is based on voltage driven elements, it is convenient to work with the Norton equivalent generator circuits of Figure 2.15 and an admittance matrix of the array mutual coupling described by,

$$\mathbf{I} = \mathbf{Y}_A\mathbf{V}, \tag{2.28}$$

where $\mathbf{I} \in \mathbb{C}^{N\times 1}$ and $\mathbf{V} \in \mathbb{C}^{N\times 1}$ are column vectors[5] containing the port currents and voltages, I_n and V_n, respectively, and $\mathbf{Y}_A \in \mathbb{C}^{N\times N}$ is the array

[4]It is not always clear how to define open-circuits in computer aided design tools. Short circuits are, however, always easily defined with impedances of zero value, and open-circuits correspondingly with admittances of zero value.

[5]Upper-case letters will be used for voltages and currents in this section, as this is a common convention when working with network matrices. The remainder of the thesis will make use of lower-case characters for these values.

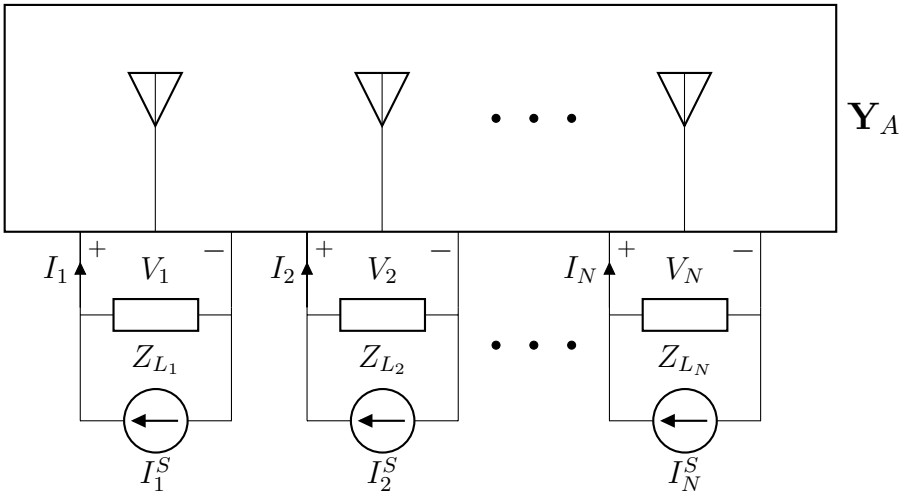

Figure 2.15: Array antenna excited with Norton equivalent sources.

admittance matrix. By stacking the Norton equivalent sources I_n^S of all N elements in a column vector $\mathbf{I}^S$, and using the constraint condition that,

$$I_n^S = I_n + V_n/Z_{L_n} \tag{2.29}$$

for all elements, (2.28) can be rewritten in terms of the Norton current sources as

$$\mathbf{I}^S = (\mathbf{Y}_A + \mathbf{Z}_L^{-1})\mathbf{V}, \tag{2.30}$$

where $\mathbf{Z}_L \in \mathbb{C}^{N\times N}$ is a diagonal matrix containing the generator loads Z_{L_n} of the individual ports. Assuming that $\mathbf{Y}_A$ and $\mathbf{Z}_L$ are known, it is straightforward to calculate the required Norton sources that results in, for example, a unit voltage at port n, and zero on all other ports. In this case, $\mathbf{V}$ can be replaced with a column vector $\mathbf{e}_n \in \mathbb{N}^{N\times 1}$ with a single unit entry at index n and zeros elsewhere. Then, the required Norton current sources must be

$$\mathbf{I}_{(\mathbf{e}_n)}^S = (\mathbf{Y}_A + \mathbf{Z}_L^{-1})\mathbf{e}_n. \tag{2.31}$$

Recalling the definitions mentioned in equations (2.25) - (2.27), an excitation according to (2.31) would radiate a far-field that is the superposition of EEPs $\vec{\boldsymbol{f}}_n^{e,Nrt}$ from (2.25), weighted accordingly by the elements of $\mathbf{I}_{(\mathbf{e}_n)}^S$. Additionally, according to (2.26) and $\mathbf{e}_n$, this excitation also radiates the SC-EEP $\vec{\boldsymbol{f}}_n^{sc}$ of element n, so that the two scenarios are equal:

$$\vec{\boldsymbol{f}}_n^{sc} = \sum_{n=1}^{N} I_{n_{(\mathbf{e}_n)}}^S \vec{\boldsymbol{f}}_n^{e,Nrt} \tag{2.32}$$

or in matrix form:[6]

$$\vec{\boldsymbol{f}}_n^{sc} = \mathbf{e}_n^T(\mathbf{Y}_A + \mathbf{Z}_L^{-1})\mathbf{F}^{e,Nrt}, \tag{2.33}$$

[6]It should be noted that in (2.33), the transpose operation (^{T}) has been omitted for $\mathbf{Y}_A$ and $\mathbf{Z}_L^{-1}$, since these are symmetrical and diagonal matrices, respectively.

where $\mathbf{F}^{e,Nrt}$ is a column vector containing the EEPs $\vec{\boldsymbol{f}}_n^{e,Nrt}$ of all elements. Noting that $\mathbf{e}_n^T$ simply acts as a selector for the SC-EEP of element n, (2.33) can be generalized to all SC-EEPs:

$$\mathbf{F}^{sc} = (\mathbf{Y}_A + \mathbf{Z}_L^{-1})\mathbf{F}^{e,Nrt}, \tag{2.34}$$

with $\mathbf{F}^{sc}$ the column vector containing all SC-EEPs $\vec{\boldsymbol{f}}_n^{sc}$. Next, the receive case is investigated to find the induced currents on the antenna element ports due to an incident plane wave.

Induced currents in the receiving case

It is possible to find the induced currents on the antenna ports due to some incident plane-wave $\vec{\boldsymbol{E}}_0$ propagating in direction $-\hat{\mathbf{r}}$ by using the reciprocity principle, along with the Norton equivalent receive circuit [27]. When all the antennas are short-circuited, the current through port n due to $\vec{\boldsymbol{E}}_0$ incident from direction (Ω_o), with some polarization $\hat{\boldsymbol{p}}$, is obtained from the corresponding SC-EEP $(\vec{\boldsymbol{f}}_n^{sc})$ as,

$$I_n^{sc}(\hat{\boldsymbol{p}}, \Omega_o) = -j\frac{4\pi}{k\eta}[\hat{\boldsymbol{p}} \cdot \vec{\boldsymbol{f}}_n^{sc}(\Omega_o)]. \tag{2.35}$$

where unit amplitude has been assumed for $|\vec{\boldsymbol{E}}_0|$. Similarly, when all antenna ports are loaded according to $\mathbf{Z}_L$, the induced current through each load Z_{L_n} can be found with current-division and the corresponding EEP $(\vec{\boldsymbol{f}}_n^{e,Nrt})$ as

$$I_n^{Z_L}(\hat{\boldsymbol{p}}, \Omega_o) = \frac{-j}{Z_{L_n}}\frac{4\pi}{k\eta}[\hat{\boldsymbol{p}} \cdot \vec{\boldsymbol{f}}_n^{e,Nrt}(\Omega_o)]. \tag{2.36}$$

Equations (2.35) and (2.36) fully satisfy the formulas found in [27]. It then follows easily from (2.34), that

$$\mathbf{I}^{Z_L} = \mathbf{Z}_L^{-1}(\mathbf{Y}_A + \mathbf{Z}_L^{-1})^{-1}\mathbf{I}^{sc}, \tag{2.37}$$

which shows that the currents induced in an array loaded by any general $\mathbf{Z}_L$ and receiving a plane wave $\vec{\boldsymbol{E}}_0$ can be obtained from knowledge of the SC-EEPS and array admittance matrix $\mathbf{Y}_A$. The voltages induced across the loads are then simply (2.37) multiplied to the left by $\mathbf{Z}_L$, which corresponds to [26, equation (6)].

2.4.3 Relation between different embedded environments

As mentioned before, the discussion here parallels that found in [26], where an expression similar to (2.34) is derived for the case of OC-EEPs as

$$\mathbf{F}^{oc} = (\mathbf{Z}_A + \mathbf{Z}_L)\mathbf{F}^{e,Thv}. \tag{2.38}$$

Table 2.1: A comparison for calculating different induced sources due to an incident plane wave on an array antenna from various EEPs. Matrix $\mathbf{U}$ denotes the identity matrix.

$C_k\times$	$\mathbf{F}^{oc}$	$\mathbf{F}^{sc}$	$\mathbf{F}^{e,Thv}$	$\mathbf{F}^{e,Nrt}$
$\mathbf{V}^{oc}=$	1	$\mathbf{Z}_A$	$(\mathbf{Z}_A+\mathbf{Z}_L)$	$(\mathbf{Z}_A\mathbf{Z}_L^{-1}+\mathbf{U})$
$\mathbf{V}^{Z_L}=$	$\mathbf{Z}_L(\mathbf{Z}_A+\mathbf{Z}_L)^{-1}$	$(\mathbf{Y}_A+\mathbf{Z}_L^{-1})^{-1}$	1	
$\mathbf{I}^{sc}=$	$\mathbf{Y}_A$	1	$(\mathbf{Y}_A\mathbf{Z}_L+\mathbf{U})$	$(\mathbf{Y}_A+\mathbf{Z}_L^{-1})$
$\mathbf{I}^{Z_L}=$	$(\mathbf{Z}_A+\mathbf{Z}_L)^{-1}$	$\mathbf{Z}_L^{-1}(\mathbf{Y}_A+\mathbf{Z}_L^{-1})^{-1}$		1

The EEPs in (2.38) are, however, defined by Thevenin sources with unit voltage (hence the included (^{Thv}) superscript) and therefore differs from the EEPs defined by equation (2.25) by a scaling factor which depends on the generator loads. In view of this, it is possible to express (2.34) in terms of $\mathbf{F}^{e,Thv}$ by simply scaling the Norton sources with $\mathbf{Z}_L$, which ultimately results in

$$\mathbf{F}^{sc}=(\mathbf{Y}_A\mathbf{Z}_L+\mathbf{U})\mathbf{F}^{e,Thv}. \tag{2.39}$$

From (2.38) and (2.39), it is then possible to relate the OC-EEPs and SC-EEPs:

$$\mathbf{F}^{oc}=(\mathbf{Z}_A+\mathbf{Z}_L)(\mathbf{Y}_A\mathbf{Z}_L+\mathbf{U})^{-1}\mathbf{F}^{sc}. \tag{2.40}$$

Using the identity [28]

$$(\mathbf{A}^{-1}+\mathbf{U})^{-1}=\mathbf{A}(\mathbf{A}+\mathbf{U})^{-1}, \tag{2.41}$$

followed by some manipulations, (2.40) simplifies to

$$\mathbf{F}^{oc}=\mathbf{Z}_A\mathbf{F}^{sc}. \tag{2.42}$$

The result above holds regardless of the values of the loads. Finally, it is noted that (2.42) can also rapidly be obtained by working directly with port currents $\mathbf{I}$ and port voltages $\mathbf{V}$ along with superposition, while disregarding the Thevenin and Norton circuits entirely [29]. In any case, the result is an insightful one to have.

A summary of comparisons for calculating induced sources with different EEPs due to a plane wave incident on the array is included in Table 2.1. The table is to be read as the row of interest being equal to C_k times the corresponding column intersect and header, C_k being defined as,

$$C_k=j\frac{4\pi}{k\eta}. \tag{2.43}$$

For example, $\mathbf{I}^{sc}=C_k(\mathbf{Y}_A\mathbf{Z}_L+\mathbf{U})\mathbf{F}^{e,Thv}$.

It should be clear that if any one of the embedded pattern sets (loaded, short- or open circuited) are known, along with the array coupling matrix and loads, all other sets can be derived accordingly. This concept has proved valuable for efficient full-wave simulation of an array feed in order to obtain the scattering parameters and all EEPs with a single MoM matrix solution. This is discussed more in Section 3.1.2.

2.5 Array Signal Processing and Beamforming

In the discussion of array antenna signal processing, it is helpful to forget, for a moment, about all the electromagnetic complexities regarding what happens at the antenna ports, and to consider a simplified representation similar to Figure 2.16. Of primary concern here is that, ultimately, there are signals arriving at receiver outputs, which may be stacked into a complex column vector $\mathbf{v} = [v_1, v_2, ...v_N]^T$, where v_n is the complex envelope representation [30] of the signal on the nth receiver chains.

In a typical scenario, $\mathbf{v}$ consists of non-deterministic contributions due to some signal of interest, interfering signals, receiver noise, and external background noise [31]:

$$\mathbf{v} = \mathbf{v}_{\text{sig}} + \mathbf{v}_{\text{int}} + \mathbf{v}_{\text{rec}} + \mathbf{v}_{\text{ext}}. \tag{2.44}$$

A fundamental tool in array signal processing is the use of signal and noise correlation matrices, defined as [30, 31]

$$\mathbf{R}_{\text{v}} = \text{E}\{\mathbf{v}\mathbf{v}^{\dagger}\} = \mathbf{R}_{\text{sig}} + \mathbf{R}_{\text{int}} + \mathbf{R}_{\text{rec}} + \mathbf{R}_{\text{ext}} \tag{2.45}$$

where signal and noise contributions have been assumed uncorrelated, and $\text{E}\{\cdot\}$ denotes the expectation operator. The signals from (2.44) are combined according to the complex weight vector $\mathbf{w}$ to obtain the beamformed output voltage v_{out} as

$$v_{out} = \mathbf{w}^{\dagger}\mathbf{v}, \tag{2.46}$$

where † denotes the conjugate transpose operator, and follows from convention in signal processing literature. The total beamformed output power can then be expressed using (2.46) and (2.45) as

$$P_{\text{out}} = \mathbf{w}^{\dagger}\mathbf{R}_{\text{sig}}\mathbf{w} + \mathbf{w}^{\dagger}\mathbf{R}_{\text{n}}\mathbf{w} \tag{2.47}$$

$$= P_{\text{sig}} + P_{\text{n}}, \tag{2.48}$$

where all noise contributions has been lumped into a single noise correlation matrix $\mathbf{R}_{\text{n}} = \mathbf{R}_{\text{int}} + \mathbf{R}_{\text{rec}} + \mathbf{R}_{\text{ext}}$. Two beamforming strategies which will be used throughout the thesis will briefly be defined.

2.5.1 Beamforming Strategies

Optimal beamforming techniques are concerned with obtaining the weights w_n required to steer the receiving beam in some desired direction by adding signals on individual receiver ports in phase while simultaneously mitigating noise contributions. Comprehensive treatments on the subject can be found, for example, in [32, 33, 30]. This thesis will primarily make use of only two techniques, namely *conjugate field match* (CFM) and maximum *signal-to-noise ratio* (max-SNR) beamformers.

CFM beamformer weights are perhaps the simplest to determine, since it requires only knowledge of the relative amplitude and phase shifts among the element receiver chains for some incident signal

$$\mathbf{w}_{\text{CFM}} = \mathbf{v}_{\text{sig}}(\Omega_s) \tag{2.49}$$

where $\mathbf{v}_{sig}(\Omega_s)$ is receiver output voltage vector due to some signal of interest incident from direction (Ω_s). This is typically also known as the conventional delay-and-sum beamformer [32], with the narrowband assumption that time delays can be achieved with simple phase-shifts.

Statistically optimal max-SNR beamforming weights can be formulated by expressing the SNR as a ratio of quadratic forms

$$\text{SNR} = \frac{\mathbf{w}^{\dagger}\mathbf{R}_{\text{sig}}\mathbf{w}}{\mathbf{w}^{\dagger}\mathbf{R}_{\text{n}}\mathbf{w}}. \tag{2.50}$$

Maximizing the expression in (2.50) in terms of $\mathbf{w}$ results in a general eigenvalue problem [30]. When the signal of interested is assumed as a point source, the maximum SNR beamforming weights are obtained as [34, 33, 30]

$$\mathbf{w}_{\text{SNR}} = \mathbf{R}_n^{-1}\mathbf{v}_{\text{sig}}(\Omega_s) \tag{2.51}$$

Equations (2.49) and (2.51) will be used in upcoming chapters to compare the difference in system performance due to different beamforming weights.

2.6 System Characterisation for Receiving Antennas

Since this thesis is primarily concerned with receiving antennas, the final section in Chapter 2 is concerned with the primary figure of merit for communication receivers, which is the obtainable *signal-to-noise ratio* (SNR) at the system output. In antenna analysis, SNR for a single port antenna is expressed

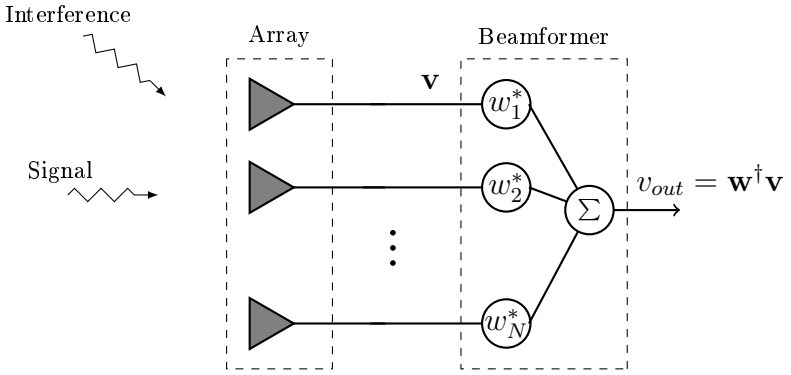

Figure 2.16: General beamformer topology

as the ratio of antenna gain G and equivalent system noise temperature T_{sys} according to [35, 14]

$$\frac{G}{T_{\text{sys}}} = \frac{\eta_{ap}\eta_{rad}D_{\text{o,(max)}}}{T_{\text{rec}} + (1-\eta_{rad})T_{\text{a}} + \eta_{rad}T_{\text{ext}}}. \tag{2.52}$$

where η_{rad} and η_{ap} are the radiation and aperture efficiencies respectively, T_{a} the ambient temperature of the antenna, and T_{rec} is the equivalent receiver noise temperature, mainly due to first-stage *low noise amplifiers* (LNA). The parameter T_{ext} is the antenna external background noise temperature (brightness temperature), which is obtained by integrating the antenna power pattern over the surrounding brightness scene

$$T_{\text{ext}} = \frac{\iint_{\Omega_o} T_b(\theta,\phi)|\vec{\boldsymbol{f}}_f(\theta_f,\phi_f)|^2 d\Omega_o}{\iint_{\Omega_o} |\vec{\boldsymbol{f}}_f(\theta_f,\phi_f)|^2 d\Omega_o}. \tag{2.53}$$

While the system G/T_{sys} is well known and defined for single port antennas, similar characterisation of an array receiver is not so straightforward. The difficulty lies in the fact that final output for a multi-element receiver, typically the beamformer output, is preceded by arbitrary gain factors due to various amplifier gains, mixer conversion losses, and potential digital conversion factors.

While sensitivity definitions for array receivers have made appearances in the literature [36, 37], the IEEE standards and definitions for antenna [15] has only recently been updated with terms meant specifically to deal with these issues. Some details for these terms have been included in Appendix B for the interested reader. These will be used throughout the thesis. Readers are encouraged to refer to [15] for a comprehensive treatment regarding these terms.

Chapter 3

Modelling of Phased Array Feed Systems

The purpose of this chapter is to describe the phased array feed system modelling approach that has been used for this thesis. The model has been aimed at being quite general, and can be used to perform various parameter studies. An overall illustration of the developed system model is shown in Figure 3.1.

As mentioned in Section 2.4, accurate modelling of an array receiver requires knowledge of the embedded element patterns, along with the array coupling matrix. These parameters are obtained through full-wave electromagnetic (EM) simulations of the reflector and array feed using HyperWorks software package FEKO [38] (blue box in Figure 3.1). Section 3.1.1 presents a general discussion on possible simulation approaches for a reflector and feed antenna. Some attention has been devoted in developing various Lua scripts[1] that automates an efficient simulation procedure once an PAF model as been constructed, and a brief description regarding this is given in Section 3.1.2. The exact details of the scripts have been included in Appendix A.

The full-wave simulation results can then be imported into MATLAB, and from there it is possible to investigate different aspects of the receiver chains connected to the array elements (red box in Figure 3.1). Section 3.2 outlines some details on the numerical implementation of the receiver network model used in the thesis, which is based on a scattering parameter formulation.

In Section 3.4 a simulation example is conducted using a 15-element dipole array feed. The example includes beamsteering in different directions, and noise matching techniques.

[1] FEKO allows users the ability to incorporate their own Lua scripts for specific automation tasks. Comprehensive documentation can be found in FEKO's user manaul [38].

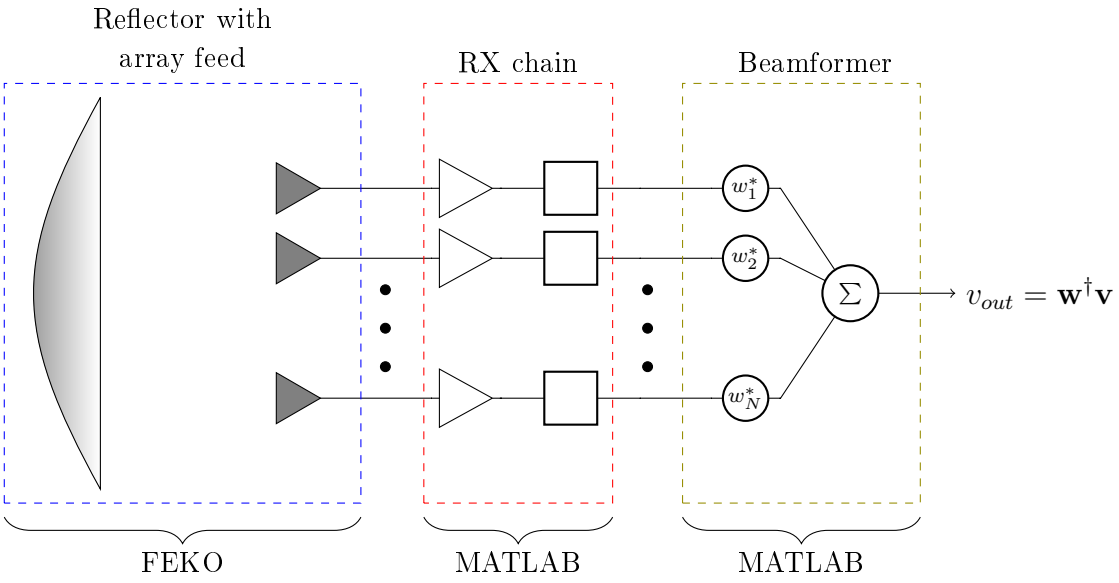

Figure 3.1: Depiction of the developed array feed receiver system.

3.1 PAF Simulation with FEKO

In this section, the simulation of a PAF system in FEKO, with the focus on obtaining the EEPs and coupling parameters of the array is discussed. Section 3.1.1 presents the definitions of primary and secondary patterns used throughout thesis, and a discussion on possible simulation strategies for array and reflector antennas in FEKO. Section 3.1.2 gives an explanation of an efficient simulation procedure for obtaining the antenna coupling parameters and EEPs.

3.1.1 Primary and Secondary EEPs and Simulation Approaches

Throughout the thesis, it will be necessary to distinguish between the EEPs of the array antenna with and without the presence of a reflector. Thus, the term *primary embedded element patters* will refer to the EEPs of the array feed without the presence of a reflector. Correspondingly, the term *secondary embedded elements patterns* will refer to when the EEPs include the focusing effect of a reflector.

There are generally two approaches possible for simulating a PAF. The first and most accurate approach entails simulating the full-system together, which results in obtaining the secondary EEPs directly. FEKO offers various hybridised solvers, and in this case the array would typically be solved using

the MoM, and the reflector according to *physical optics* (PO), in which case FEKO then calculates the coupling between the MoM- and PO regions. Alternatively, FEKO's *multi-level fast multipole method* (MLFMM) solver can be used to solve and simulate the entire system. The secondary EEPs are highly directive and possess many side-lobes, which requires many data points in order to give an accurate representation of the full radiation patterns.

Alternatively, the primary EEPs can first be obtained by simulating the array feed in isolation using the MoM. These EEPs can then be saved and applied as equivalent far-field *point sources* to the reflector antenna (similar to the analytical feed point sources discussed in Section 2.2.2) in order to obtain the secondary EEPs with PO. While this approach does not take into account any reflector and feed interaction or feed blockage effects, it allows different reflector geometries to be investigated quickly for the same array feed, as PO simulation with point sources is computationally much cheaper. Additionally, the primary EEPs posses much smoother angular variation, as opposed the the secondary patters, allowing fewer data points for accurate representation. This also simplifies antenna external noise integrals, discussed in Section 3.2.2.

3.1.2 Efficient Simulation Procedure

FEKO is well-equipped with tools meant specifically for analysing array antennas, such as the domain Green's function method (DGFM) [39] for large finite array arrays, or periodic boundary conditions (PBC), which allows simulating an element as if embedded in an infinite array [38]. However, while these tools are convenient for studying the full-operation of arrays, where all elements are excited in some desired way, it is the *individual* embedded element patterns and coupling matrix that are of primary concern for phased arrays feeds, since after knowing these parameters the effects of different excitations and beamforming strategies can be studied in post-processing.

In view of the above, the best way forward was to create several Lua scripts that allows simplifying the setting up of simulation requests and exporting of data once an array model has been created. In terms of FEKO's terminology, a *S-parameter configuration* is required to obtain the array port scattering parameters, in additional to N separate *Standard configurations* for computing the element far-field EEPs, N being the number of elements[2]. It would, however, be unreasonable to re-solve the system MoM matrix for each separate configuration. Fortunately, FEKO allows this problem to be avoided by

[2]The reason for separate configurations for each array element is that the excitation scheme for each EEP is unique. For example, the configuration for the EEP of element n requires unit excitation of that element, with all other elements terminated either with loads, open- or short circuits

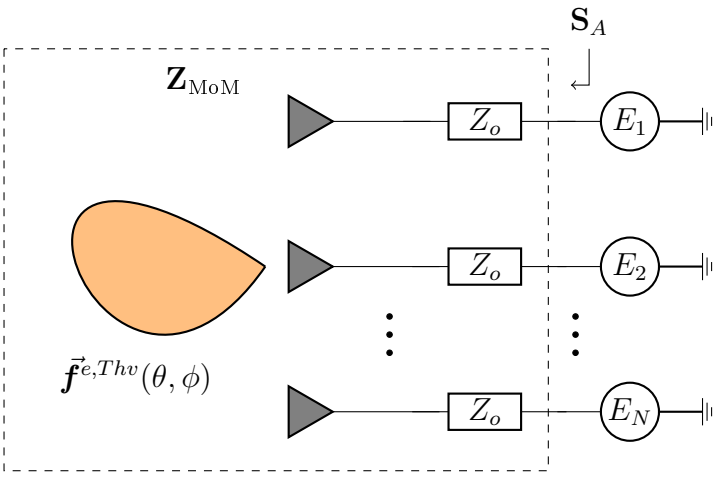

Figure 3.2: Illustration of simulation procedure.

properly setting up the simulation model and understanding the simulation workflow.

The simulation procedure is depicted in Figure 3.2. By simulating the *S-parameter configuration* first, characteristic impedances Z_o are placed at each port. The MoM matrix is set-up and solved with the included characteristic impedances as

$$\{\mathbf{J}\} = \{\mathbf{Z}_{\text{MoM}}\}^{-1}\{\mathbf{E}\} \tag{3.1}$$

and the array scattering matrix $\mathbf{S}_A$ is calculated. By keeping the characteristic impedances in place[3], each consecutive *Standard configuration* necessitates only a change on the right-hand-side excitation vector $\{\mathbf{E}\}$ in (3.1), in order to compute the far-field data points for each array element, effectively simulating the Thevenin equivalent set of EEPs $\mathbf{F}^{e,Thv}$ (see Section 2.4.3). This procedure saves a considerable amount of time, as the inversion of MoM-impedance matrix $\{\mathbf{Z}_{\text{MoM}}\}$ makes up a large-part of the total-run time. Details on Lua scripts can be found in Appendix A.

3.2 Array Receiver Network Model

The previous section discussed various methods of simulating PAFs in FEKO. To briefly review these results, after simulating the phased array feed system in FEKO, one is left the primary and/or secondary Thevenin equivalent EEPs ($\mathbf{F}^{e,Thv}$), as well as the antenna scattering parameter matrix $\mathbf{S}_A$. Any corresponding EEP set can then be obtained with the help of Table 2.1. For

[3]This is an option that must be activated in the *S-parameter configuration*. See [38].

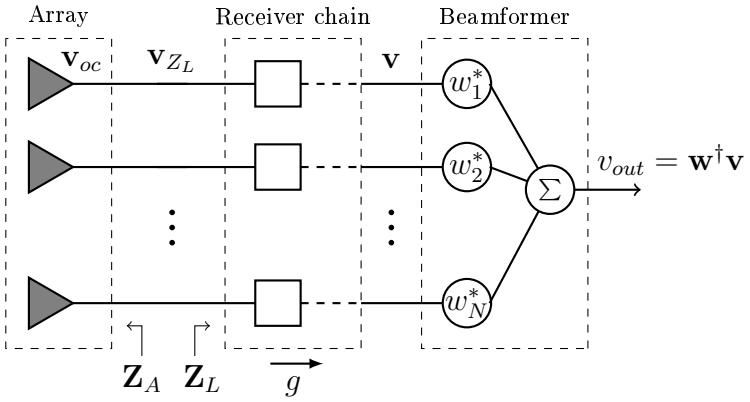

Figure 3.3: Impedance based network model for a receiving antenna array.

example, the array impedance matrix $\mathbf{Z}_A$ is easily obtained from $\mathbf{S}_A$ as [35]

$$\mathbf{Z}_A = Z_o(\mathbf{U} + \mathbf{S}_A)(\mathbf{U} - \mathbf{S}_A)^{-1}, \tag{3.2}$$

and, by using Table 2.1, the OC-EEPs can be obtained by

$$\mathbf{F}^{oc} = Z_o(\mathbf{Z}_A + Z_o\mathbf{U})^{-1}\mathbf{F}^{e,Thv}, \tag{3.3}$$

where $\mathbf{F}^{e,Thv}$ is the EEPs simulated in FEKO, and Z_o is the reference impedance for $\mathbf{S}_A$.

The main focus of Section 3.2 revolves around using the EEPs and coupling matrix to construct an array receiver network model which can be used to study the effects of different receiver chains, and to accurately model receiver and external noise. Section 3.2.1 presents a general array receiver model, which is convenient for describing the reciprocity relation for array receivers. The numerical receiver implemented in the thesis is, however, based on a scattering parameter formulation, which is discussed in Section 3.2.2.

3.2.1 General Network and Reciprocity Relations

A general N element receiving array is shown in Figure 3.3, which is based on an impedance representation and open-circuit voltages [40]. For a plane wave incident on the PAF receiver system, the induced open-circuit voltage on array element $n \in \{1, 2, .., N\}$ can be determined with the corresponding OC-EEP and the help of Table 2.1 as,

$$v_{oc,n}(\hat{\boldsymbol{p}}, \Omega_o) = C_k \left[\hat{\boldsymbol{p}} \cdot \vec{\boldsymbol{f}}_{oc,n}(\Omega_o)\right] \tag{3.4}$$

where all $\vec{\boldsymbol{f}}_{oc,n}$ are secondary EEPs, hence includes the reflector focusing effect. The array elements are loaded according to a diagonal impedance matrix $\mathbf{Z}_L$,

with entries corresponding to the input impedances seen looking into each receiver chain. The voltages appearing at the receiver output $\mathbf{v}$ can then be expressed as,

$$\mathbf{v} = g\mathbf{Z}_L(\mathbf{Z}_A + \mathbf{Z}_L)^{-1}\mathbf{v}_{oc} \tag{3.5}$$

where g is some relative voltage gain from receiver input to output. It is common in the literature to lump the receiver chain into a single linear transformation matrix $\mathbf{Q} \in \mathbb{C}^{N\times N}$, as

$$\mathbf{Q} = g\mathbf{Z}_L(\mathbf{Z}_A + \mathbf{Z}_L)^{-1} \tag{3.6}$$

which transfers open-circuit voltages at the array elements to the receiver output. This allows the beamformed output voltage v_{out} to be conveniently expressed in terms of the induced open-circuit voltages as,

$$v_{out} = \mathbf{w}^\dagger\mathbf{v} = \mathbf{w}^\dagger\mathbf{Q}\mathbf{v}_{oc} \tag{3.7}$$

From equation (3.7) follows an important reciprocity expression for an array antenna: By using (3.4), the beamformed output voltage can be expressed in terms of the OC-EEPs as

$$v_{out}(\Omega_o) = C_k\mathbf{w}^\dagger\mathbf{Q}\mathbf{F}^{oc}(\Omega_o), \tag{3.8}$$

keeping in mind to the inner product with $\hat{\mathbf{p}}$ to include the dependence on polarisation. In words, (3.8) shows that the beamformed output voltage, as a function of its response to incident plane waves, is proportional to the linear combination of the array OC-EEPs weighted accordingly by 'currents' $\mathbf{i} \in \mathbb{C}^{1\times N}$ as,

$$\mathbf{i} = C_k\mathbf{w}^\dagger\mathbf{Q}. \tag{3.9}$$

The impedance network description is useful for presenting and understanding the reciprocity relations mentioned above.

The next step in the array receiver model is defining the various signal and noise correlation matrices, and several network formulation can be found in the literature [40, 9, 8, 41, 42]. A choice was made to use a scattering parameter formulation for this thesis, which is discussed in the next section.

3.2.2 Scattering Parameter Formulation

When a detailed analysis of the front-end receiver network is required, a scattering parameter network formulation might be more appropriate. There are various reasons for this, including that, 1) S-parameters are commonly used in microwave circuit analysis, 2) manufacturers typically supply specifications of microwave components in terms of S-parameters, and so practical values can easily be included in the model, and 3) vector network analyser measurements

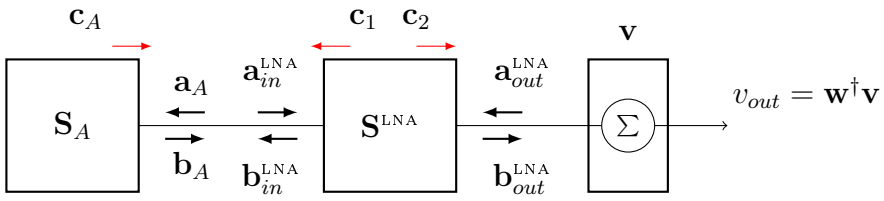

Figure 3.4: Simplified scattering parameter network model for a receiving antenna array.

are based on scattering parameters. Still, the choice ultimately remains merely a matter of preference. The results from Section 3.2.2 are based on [43, 8], and has mainly been used in the MATLAB code of the receiver chains in the thesis.

Shown in Figure 3.4 is a scattering parameter network description of a receiving array with low-noise-amplifiers (LNA) connected to all array ports. The network relationship equations can be set-up as,

$$\begin{bmatrix} \mathbf{b}_{out}^{\text{LNA}} \\ \mathbf{b}_{in}^{\text{LNA}} \\ \mathbf{b}_A \end{bmatrix} = \begin{bmatrix} \mathbf{S}_{22}^{\text{LNA}} & \mathbf{S}_{21}^{\text{LNA}} & \mathbf{0} \\ \mathbf{S}_{12}^{\text{LNA}} & \mathbf{S}_{11}^{\text{LNA}} & \mathbf{0} \\ \mathbf{0} & \mathbf{0} & \mathbf{S}_A \end{bmatrix} \begin{bmatrix} \mathbf{a}_{out}^{\text{LNA}} \\ \mathbf{a}_{in}^{\text{LNA}} \\ \mathbf{a}_A \end{bmatrix} + \begin{bmatrix} \mathbf{c}_2 \\ \mathbf{c}_1 \\ \mathbf{c}_A \end{bmatrix} \tag{3.10}$$

where all matrices and vectors ($\in \mathbb{C}$) are of size $(N \times N)$ and $(N \times 1)$ respectively. The matrix $\mathbf{S}_A$ is the array scattering matrix, and the four matrices $\mathbf{S}_{ij}^{\text{LNA}}$ $(i, j \in 1, 2)$ contain only diagonal entries corresponding to the scattering parameter values of the individual LNAs. Vector $\mathbf{c}_A$ represents independent internal generators of $\mathbf{S}_A$ due to received incident signals and thermal/background noise. Vectors $\mathbf{c}_1$ and $\mathbf{c}_2$ represent LNA input and output generated noise waves respectively, according to their equivalent noise wave representation [44].

For simplicity, the amplifier outputs will be assumed to be terminated in matched loads[4] ($\mathbf{a}_{out}^{LNA} = 0$). The goal is then to express $\mathbf{b}_{out}^{LNA}$ in terms of $\mathbf{c}_A$, $\mathbf{c}_1$ and $\mathbf{c}_2$. This can be done using a linear connection method from [45] or the equations derived in [8]. The resulting LNA output waves are,

$$\mathbf{b}_{out}^{\text{LNA}} = \mathbf{T}\mathbf{c}_A + \mathbf{T}\mathbf{S}_A\mathbf{c}_1 + \mathbf{c}_2, \tag{3.11}$$

where the matrix $\mathbf{T}$ has been introduced as

$$\mathbf{T} = \mathbf{S}_{21}^{\text{LNA}}(\mathbf{U} - \mathbf{S}_A\mathbf{S}_{11}^{\text{LNA}})^{-1}. \tag{3.12}$$

The matrix $\mathbf{T} \in \mathbb{C}^{N \times N}$ is similar to $\mathbf{Q}$ in (3.6), and can be viewed as a linear transformation matrix that transfers forward waves at the LNA inputs to their

[4]The assumption of matched amplifiers is not too far-fetched, since many commercial components are based on standard 50 Ω terminations. Even if some small mismatch exists, S_{12}^{LNA} of most amplifiers is typically small, and the matched case remains a reasonable assumption. Still, a more general scenario can be found in [8].

outputs after reflection and coupling effects. From (3.11), it is then possible to find the voltages at the beamformer input as [35]

$$\mathbf{v} = \frac{Z_o^* \mathbf{b}_{out}^{\text{LNA}}}{\sqrt{\text{Re}(R_o)}} = \sqrt{Z_o}(\mathbf{b}_{out}^{\text{LNA}}), \tag{3.13}$$

where Z_o is the S-parameter reference impedance, assumed to be real throughout. This last step is perhaps unnecessary; however, a large amount of array signal processing literature is based on voltage descriptions of signals, hence expressing final receiver outputs in terms of voltages $\mathbf{v}$ allows easy transitioning between microwave scattering parameter analysis and the representations used array signal processing. The array output waves $\mathbf{c}_A$ can always be related to the array open-circuits voltage $\mathbf{v}_{oc}$ from (3.4), as [43],

$$\mathbf{c}_A = \mathbf{L}\mathbf{v}_{oc} \tag{3.14}$$

$$\text{where,} \qquad \mathbf{L} = \sqrt{Z_o}(\mathbf{Z}_A + Z_o\mathbf{U})^{-1}. \tag{3.15}$$

Attention will briefly be given separately to $\mathbf{c}_A$ and the LNA noise waves $\mathbf{c}_1$ and $\mathbf{c}_2$. This is possible as long as it can be assumed that signals and noise generated by different phenomenon are uncorrelated.

Signal Propagation Through Receiver

In this case the system is considered noiseless so that $\mathbf{c}_1$ and $\mathbf{c}_2$ can be set to zero. Labelling the array antenna output waves due to some incident plane-wave signal as $\mathbf{c}_{A,\text{sig}}$, the receiver output voltages is obtained using (3.11) and (3.13),

$$\mathbf{v}_{\text{sig}} = \sqrt{Z_o}\mathbf{T}\mathbf{c}_{A,\text{sig}} \tag{3.16}$$

The signal correlation matrix can thus be expressed as

$$\begin{aligned}\mathbf{R}_{\text{sig}} &= \text{E}\{\mathbf{v}_{\text{sig}}\mathbf{v}_{\text{sig}}^\dagger\} = Z_o\mathbf{T}\text{E}\{\mathbf{c}_{A,\text{sig}}\mathbf{c}_{A,\text{sig}}^\dagger\}\mathbf{T}^\dagger \\ &= Z_o\mathbf{T}\mathbf{L}\text{E}\{\mathbf{v}_{oc}\mathbf{v}_{oc}^\dagger\}\mathbf{T}^\dagger\mathbf{L}^\dagger,\end{aligned} \tag{3.17}$$

where in the last line, $\mathbf{L}$ has been taken from (3.15) to obtain a expression in terms of open circuit voltages, and $\text{E}\{\cdot\}$ is the expectation operator, as before. The signal power at the beamformer output is then,

$$P_{\text{sig}} = \mathbf{w}^\dagger\mathbf{R}_{\text{sig}}\mathbf{w}. \tag{3.18}$$

In the case when the incident signal is a time-harmonic plane-wave due to a point source, the expectation operator $\text{E}\{\cdot\}$ can be dropped.

In this specific case, with matched LNA output, one could define a voltage gain $g = S_{21}^{\text{LNA}}/(1 + S_{11}^{\text{LNA}})$ and input impedance $Z_L = Z_o(1 + S_{11}^{\text{LNA}})/(1 - S_{11}^{\text{LNA}})$ for all receiver chains, and verify that

$$\mathbf{Q} = \sqrt{Z_o}\mathbf{T}\mathbf{L}, \tag{3.19}$$

where $\mathbf{Q}$ is from (3.6). This simply shows that the various network representation are equivalent. Of course, the results here applies to incident signals of interest as well as interfering signals.

External Thermal Noise

Noise fluctuations at the array elements due to some external brightness temperature distribution $T_{\mathrm{b}}(\Omega_o)$ can be represented as noise waves $\mathbf{c}_{A,\mathrm{ext}}$ emanating from the antenna ports, which propagates through the receiver chains in a similar way as $\mathbf{c}_{A,\mathrm{sig}}$ discussed before. Thus, the receiver output correlation matrix $\mathbf{R}_{\mathrm{ext}}$ due to $T_{\mathrm{b}}(\Omega_o)$ can be expressed as,

$$\begin{aligned}\mathbf{R}_{\mathrm{ext}} &= Z_o\mathbf{T}\mathrm{E}\{\mathbf{c}_{A,ext}\mathbf{c}_{A,ext}^{\dagger}\}\mathbf{T}^{\dagger} \\ &= Z_o\mathbf{T}\mathbf{L}\mathrm{E}\{\mathbf{v}_{oc,\mathrm{ext}}\mathbf{v}_{oc,\mathrm{ext}}^{\dagger}\}\mathbf{L}^{\dagger}\mathbf{T}^{\dagger}\end{aligned} \tag{3.20}$$

The entries of correlation matrix of $\mathrm{E}\{\mathbf{v}_{oc,\mathrm{ext}}\mathbf{v}_{oc,\mathrm{ext}}^{\dagger}\}$, which represent the correlation between open-circuit voltages induced at the antenna ports due to the brightness temperature distribution $T_{\mathrm{b}}(\Omega_o)$, can be obtained by integrating corresponding overlap of OC-EEPs as [40, 43, 34],

$$\mathrm{E}\{v_{oc,\mathrm{ext}}^{m}v_{oc,\mathrm{ext},n}^{n^*}\} = \frac{8k_b}{2\eta}\iint_{\Omega_o} T_{\mathrm{b}}(\Omega_o)[\vec{\boldsymbol{f}}_m^{oc}\cdot\vec{\boldsymbol{f}}_n^{oc^*}]d\Omega_o \tag{3.21}$$

The receiver output noise power is then

$$P_{\mathrm{ext}} = \mathbf{w}^{\dagger}\mathbf{R}_{\mathrm{ext}}\mathbf{w}. \tag{3.22}$$

The numerical model developed for the thesis makes use of brightness temperature Model 3 from [46].

LNA Noise Coupling

Following the same procedure discussed up till now, $\mathbf{c}_A$ is set to zero, and the receiver output voltage fluctuations $\mathbf{v}_{\mathrm{rec}}$ due to LNA noise is expressed in terms of $\mathbf{c}_1$ and $\mathbf{c}_2$ by using (3.11) and (3.13) according to

$$\mathbf{v}_{\mathrm{rec}} = \sqrt{Z_o}(\mathbf{T}\mathbf{S}_{\mathrm{A}}\mathbf{c}_1 + \mathbf{c}_2), \tag{3.23}$$

Note qualitatively in (3.23) how the noise waves $\mathbf{c}_2$ travel directly to the receiver output, while noise waves $\mathbf{c}_1$ first reflects and couples across the array via $\mathbf{S}_A$, to eventually be amplified via all neighbouring receiver chains to the receiver output according to $\mathbf{T}$. The LNA noise voltage correlation matrix $\mathbf{R}_{\mathrm{rec}}$ is expressed as,

$$\begin{aligned}\mathbf{R}_{\mathrm{rec}} &= \mathrm{E}\{\mathbf{v}_{\mathrm{rec}}\mathbf{v}_{\mathrm{rec}}^{\dagger}\} \\ &= Z_o\left(\mathbf{T}\mathbf{S}_{\mathrm{A}}\mathrm{E}\{\mathbf{c}_1\mathbf{c}_1^{\dagger}\}\mathbf{S}_{\mathrm{A}}^{\dagger}\mathbf{T}^{\dagger} + \mathbf{T}\mathbf{S}_{\mathrm{A}}\mathrm{E}\{\mathbf{c}_1\mathbf{c}_2^{\dagger}\} + \mathrm{E}\{\mathbf{c}_2\mathbf{c}_1^{\dagger}\}\mathbf{S}_{\mathrm{A}}^{\dagger}\mathbf{T}^{\dagger} + \mathrm{E}\{\mathbf{c}_2\mathbf{c}_2^{\dagger}\}\right).\end{aligned} \tag{3.24}$$

A safe assumption is that the noise generated by each amplifier is uncorrelated with that of others, so that $\mathrm{E}\{\mathbf{c}_i\mathbf{c}_j^\dagger\}$ $(i,j \in 1,2)$ are diagonal matrices. Then, knowing the noise parameters T_{min}, R_n and Γ_{opt} of the all the LNAs, the diagonal terms are easily evaluated with the help of equations found in [44] as,

$$\mathrm{E}\{|c_1|^2\} = k_b T_{\min}\left(|S_{11}^{\mathrm{LNA}}|^2 - 1\right) + \frac{k_b t|1 - S_{11}^{\mathrm{LNA}}\Gamma_{opt}|^2}{|1+\Gamma_{opt}|^2} \tag{3.25}$$

$$\mathrm{E}\{|c_2|^2\} = |S_{21}^{\mathrm{LNA}}|^2\left(k_b T_{\min} + \frac{k_b t|\Gamma_{opt}|^2}{|1+\Gamma_{opt}|^2}\right) \tag{3.26}$$

$$\mathrm{E}\{c_1 c_2^*\} = \frac{-S_{21}^{\mathrm{LNA}*}\Gamma_{opt} k_b t}{|1+\Gamma_{opt}|^2} + \frac{S_{11}^{\mathrm{LNA}}}{S_{21}^{\mathrm{LNA}}}\mathrm{E}\{|c_2|^2\}. \tag{3.27}$$

Finally, the receiver noise power at the beamformer output is obtained as

$$P_{\mathrm{rec}} = \mathbf{w}^\dagger \mathbf{R}_{\mathrm{rec}} \mathbf{w}. \tag{3.28}$$

In this case, only noise generated by front-end LNA have been considered significant, since noise contributions from stages appearing after the LNAs are generally negligible.

3.2.3 Summary

In summary, the current section has described the definitions and modelling of the various signal and noise correlation matrices at the receiver output due to some incident signal of interest, external background noise and receiver noise contributions. Once these have been determined, beamforming techniques as discussed in Section 2.5 can be applied and investigated.

3.3 Developed Simulation Workflow

Before continuing, a summary workflow of the numerical simulation model that has been developed in the thesis is included here for the reader's convenience. The workflow summary is shown in Figure 3.5.

Red circles indicate user input, while the blue boxes indicate mostly automated functions. The developed Lua scripts can be applied to an array model created in FEKO, which automates the setting up and exporting of the simulated EEPs $\mathbf{F}^{e,Thv}$ and array scattering matrix $\mathbf{S}_A$, as discussed in Section 3.1.2. These parameters are fed into MATLAB, and the user supplies the LNA scattering and noise parameters, along with the angular direction of interest, and the signal and noise correlation matrices $\mathbf{R}_{\mathrm{sig}}$ and $\mathbf{R}_{\mathrm{n}} = \mathbf{R}_{\mathrm{rec}} + \mathbf{R}_{\mathrm{int}} + \mathbf{R}_{\mathrm{ext}}$ are obtained. The correlation matrices can then be used to determine the beamforming weights $\mathbf{w}$, and the resulting system G/T_{sys} is obtained.

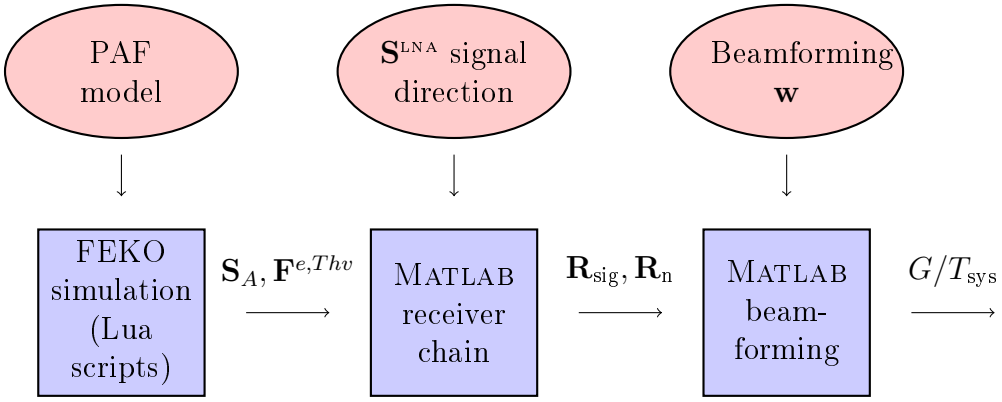

Figure 3.5: Summary workflow of the developed simulation model.

In the following section, an example is given with the purpose of illustrating the use of the developed simulation model.

3.4 15-Element Dipole PAF Example

In this section, a 15-element array of thick dipole elements, arranged in a (5×3) grid is used as an example to illustrate some of the capabilities of the developed numerical PAF modelling tools. The dipole elements are inspired from the many successful works conducted by Brigham Young University (BYU) and National Radio Astronomy Observatory (NRAO), using similar PAF elements for radio astronomy [47, 48].

The system in this example is designed to operate within the C-band downlink frequency range at a centre frequency of 4 GHz. The reflector parameters are chosen as $D = 4.5$ m, which corresponds to $\approx 60\lambda$ at 4 GHz, and $F/D = 0.36$. The array feed and full PAF system are shown in Figure 3.6a and 3.6b, respectively.

Section 3.4.1 will present a brief illustration of the simulated EEPs and scattering parameters. In Section 3.4.2, an example illustrating beam steering capabilities is given, as well as the effects of different beamforming strategies on the overall system G/T. Different receiver noise matching strategies are considered in Section 3.4.3.

3.4.1 FEKO Simulation Results

The antenna array from Figure 3.6a is first simulated in isolation, in order to obtain the primary EEPS. Figure 3.7 shows a qualitative illustration of the distorting effects that mutual coupling has on altering each individual pattern

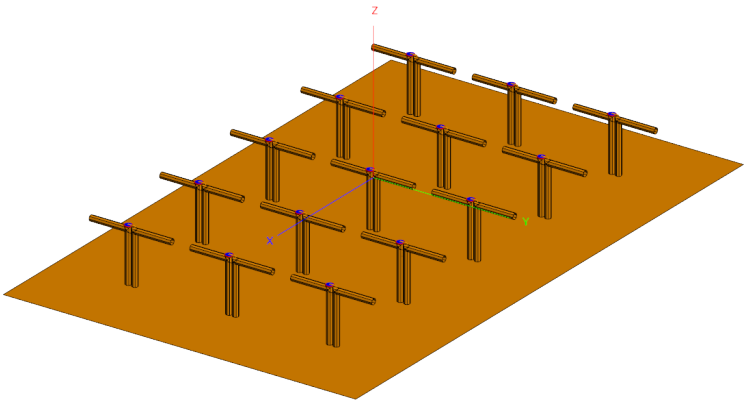

(a) (5×3) array of dipole elements above reflecting ground plane.

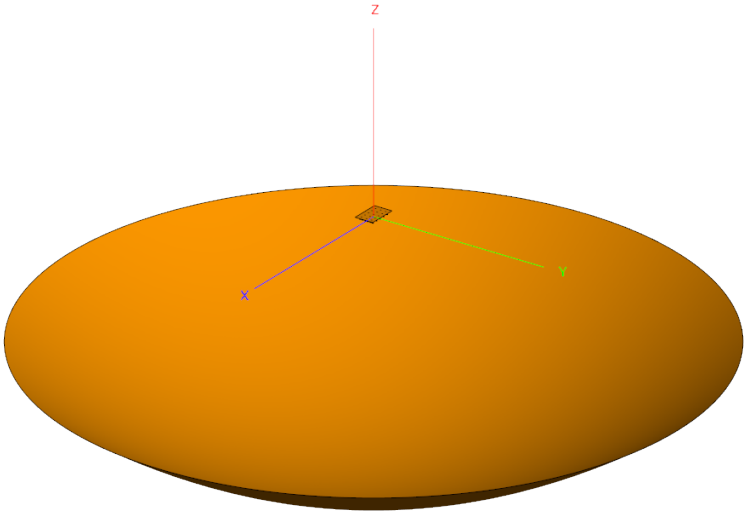

(b) Reflector with array feed

.

Figure 3.6: FEKO model for 15-element dipole PAF system.

from its isolated form, and shows the importance of working with EEPs and mutual coupling, rather than assuming identical radiation patterns for each element. The element indexing is the same as shown in Figure 2.9, with element 8 being the central element.

The primary EEPs were then applied as equivalent point sources to the reflector of Figure 3.6b, and the secondary EEPs[5] simulated using PO. Figure 3.8 shows the resulting secondary radiation patterns. Note how the individual element patterns radiate in different directions depending on their location in the focal plane. The radiation pattern of outer-most element 6 shown in Figure 3.8d gives an indication that beam steering to around 2.5° will be obtained.

[5]All other secondary EEPs are simply rotated versions of those shown in Figure 3.8, due to the symmetrical array layout.

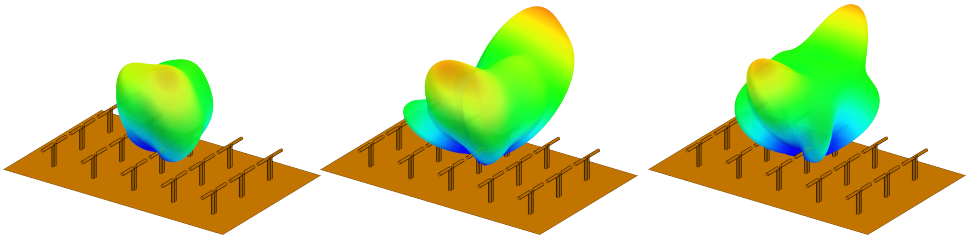

(a) Element 1. (b) Element 6. (c) Element 8.

Figure 3.7: Illustration of simulated primary EEPs of 15-element dipole array at 4 GHz.

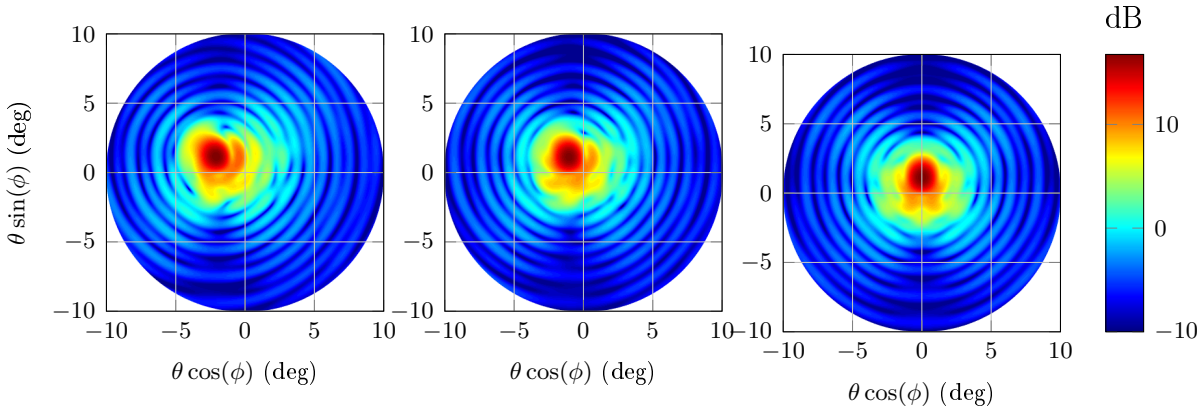

(a) Element 1. (b) Element 2. (c) Element 3.

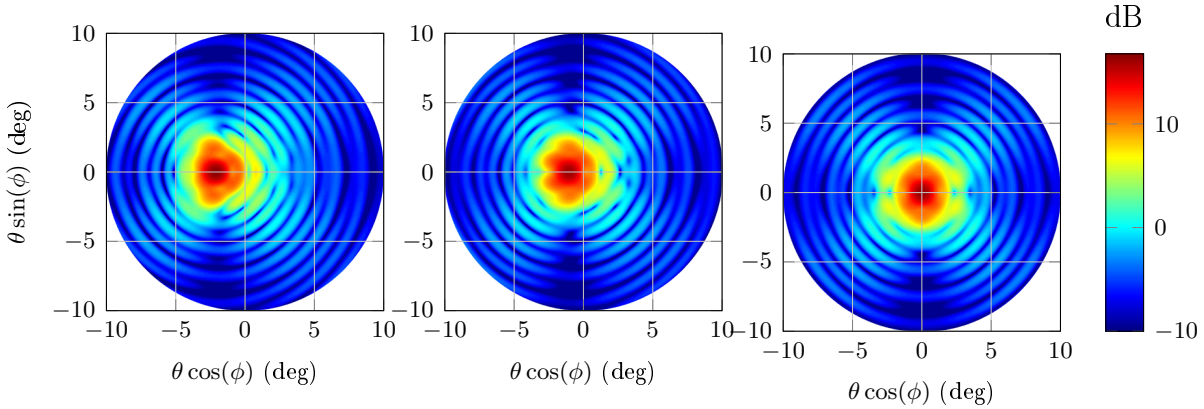

(d) Element 6. (e) Element 7. (f) Element 8.

Figure 3.8: Simulated secondary EEPs of different elements at 4 GHz.

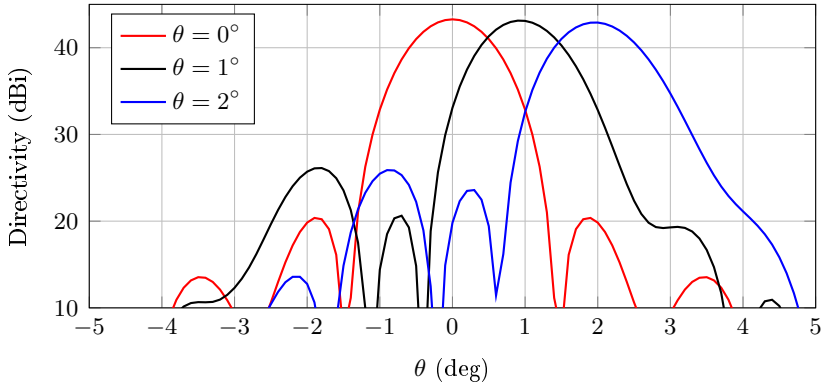

Figure 3.9: Directivity for on-axis, 1° and 2° off-axis using CFM beamforming weights for $\phi = 0°$ scanning.

The simulated EEPs and array coupling matrix are fed into MATLAB, along with LNA scattering and noise parameters. In the following sections, examples of beam scanning and receiver noise matching are given.

3.4.2 Beamforming Examples

The LNA scattering parameters in this example are assumed to be the same for all receiver chains, and defined according to

$$\mathbf{S}^{\text{LNA}} = \begin{bmatrix} 0.1 & 0 \\ 15 & 0 \end{bmatrix}. \tag{3.29}$$

In additional, noise parameters of $T_{\text{min}} = 35$ K, $R_n = 10\ \Omega$ and $\Gamma_{opt} = 0$ are assumed. Examples of beamsteering and choice of beamformer weights will be discussed next.

Beamsteering

Figure 3.9 shows the resulting directivity when beam steering along the H-plane ($\phi = 0$) for $\theta = 0°, 1°$ and 2° off-axis. For this case, CFM beamforming weights have been used according to

$$\mathbf{w} = \mathbf{v}_{\text{sig}}(\theta_d, \phi_d), \tag{3.30}$$

where θ_d is the desired scan direction. As can be seen, a relatively constant directivity is achieved for all scan-angles. The speculation in Section 3.4.1 that steering up to 2.5° also appears to be valid. Also noted is some distortion in the main-lobe starting to appear for 2° off-axis scanning, which is a result of the array feed begin unable to fully resolve the Airy-pattern first side-love, similar to the analytical case in Section 2.3.2, Figure 2.13.

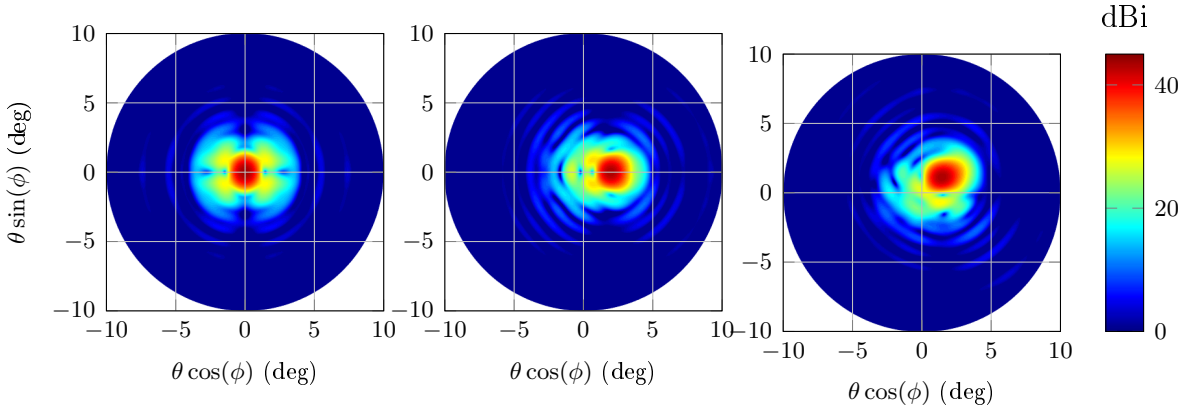

(a) $\theta = 0°, \phi = 0°$ (b) $\theta = 2°, \phi = 0°$ (c) $\theta = 2°, \phi = 45°$

Figure 3.10: Directivity obtaining for various scan angles using CFM beamforming.

A more general picture is shown in Figure 3.10, illustrating UV-plots for various scan-directions. Figures 3.10a and 3.10b correspond to the same 0° and 2° cases from Figure 3.9. Also included is a $\phi = 45°$ off-set scan for $\theta = 2°$, shown in Figure 3.10c. These results illustrate how the EEPs can be combined together in phase to radiate in certain directions, and through reciprocity, the ability of the beamforming weights to add signals incident from various directions coherently at the beamformer output.

Optimal beamforming

As a comparison between the effects of CFM- and maximum SNR beamforming weights, Figure 3.11 shows the normalized feed patterns resulting from CFM and maximum SNR beamforming weights for on-axis radiation. Apparent is the larger spill-over radiation (radiation above dotted line in Figure 3.11) for the CFM beamformer as opposed the max-SNR, which is seen to contain radiation more within the reflector. This is a result of minimizing spill-over noise. Additional distortions are also caused by mitigating receiver noise.

Figure 3.12 shows the on-axis directivity obtained due to the two beamforming strategies discussed above. As expected, the max-SNR results in some directivity loss, in addition to a wider main-beam lobe. This is due to the presence of mutual coupling

3.4.3 Receiver Noise Matching

The equivalent noise temperature T_{LNA} of an LNA, or generally any active 2-port component, can be expressed in terms of the component's *noise param-*

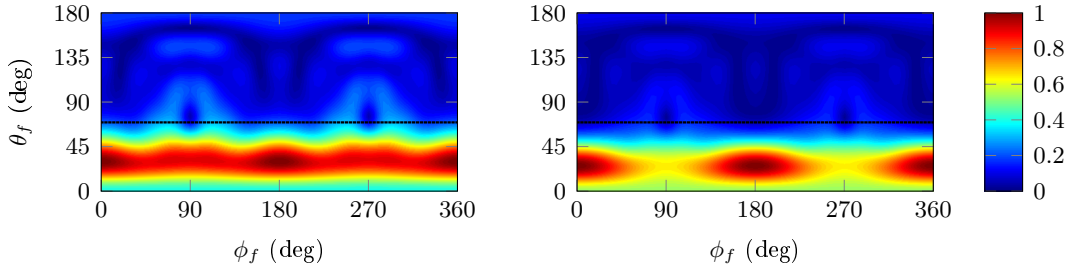

(a) $\mathbf{w} = \mathbf{w}_{\text{CFM}}$. (b) $\mathbf{w} = \mathbf{w}_{\text{SNR}}$

Figure 3.11: Normalized feed patterns resulting from various beamforming strategies for boresight reception ($\theta = 0°$, $\phi = 0°$); a) conjugate field matching b) optimal SNR

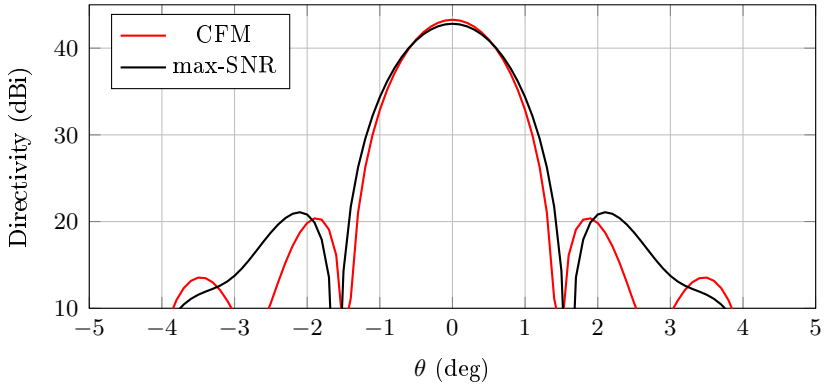

Figure 3.12: Directivity for on-axis, 1° and 2° off-axis using CFM beamforming weights for $\phi = 0°$ scanning.

eters T_{min}, R_n and Γ_{opt} as [35, 49],

$$T_{LNA} = T_{min} + \frac{4T_0R_n}{Z_0}\frac{|\Gamma_s - \Gamma_{opt}|^2}{|1+\Gamma_{opt}|^2(1-|\Gamma_s|^2)}. \tag{3.31}$$

with Γ_s being the reflection coefficient seen by the LNA input, and Z_0 the reference impedance. Optimal noise matching requires having Γ_s equal to the optimum reflection coefficient Γ_{opt} of the LNA, which results in the equivalent temperature T_{LNA} being minimized to T_{min}. With strongly coupled array elements, the situation is complicated somewhat by the fact that the reflection coefficient seen by each LNA is generally different from one another and in fact depends on the beam-scan-angle, or in general, the beamforming weights.

Optimal noise matching for coupled array antennas can be achieved with so the called active-reflection coefficient matching[6]. Qualitatively, it is based on the fact that the noise waves emanating from the LNA inputs (noise vector

6

$\mathbf{c}_1$ from Section 3.2.2), which couples across the array via mutual coupling to eventually be amplified by neighbouring element receiver chains to the receiver output, appear at the beamformer output *as if* they have been reflected at the array ports with active-reflection coefficients that are dependent on the beamformer weights, and by extension, the beam scan angle. The theoretical development of the active-reflection coefficient matching condition can be found in [50], with additional demonstrations found in [51, 52] and a comprehensive proof based on an impedance formulation can be found in [9].

In terms of the notation from developed in Section 3.2.2, the active-reflection coefficient for element n can be expressed as

$$\Gamma_{\text{act},n} = \frac{1}{w_{f,n}^*} \sum_{n=1}^{N} w_{f,m}^* S_{A,nm} \tag{3.32}$$

where $w_{f,n}$ are elements of the weight vector $\mathbf{w}_f \in \mathbb{C}^{N\times 1}$ defined as,

$$\mathbf{w}_f = \mathbf{w}\mathbf{T}^\dagger. \tag{3.33}$$

By choosing or designing all individual LNAs to have optimal reflection coefficients according to $\Gamma_{\text{opt},n} = \Gamma_{\text{act},n}$, this noise matching strategy would result in a minimum beam-equivalent-receiver noise temperature as $T_{\text{rec}} = T_{\text{min}}$ for a single beam direction [52].

A simpler noise matching strategy is to design LNAs with optimal reflection coefficients $\Gamma_{opt,n}$ equal to self-reflection coefficients of the corresponding array element:

$$\Gamma_{\text{opt},n} = S_{A,nn}. \tag{3.34}$$

The advantage of (3.34) is that the array scattering parameters are easily measured. However, this matching strategy would only be optimal when the array scattering matrix $\mathbf{S}_A$ is diagonal, which requires the use of a decoupling networks, or weakly coupled array elements [42].

The resulting beam-equivalent receiver noise temperatures as a result of the various LNA noise matching strategies discussed above is shown in Figure 3.13. The self-reflection coefficient matching from (3.34) produces the most gradual performance across the available scan range, but generally results in the highest noise temperature. The active-reflection coefficient matching condition, which has been chosen for $\theta = 1°$, is seen to obtain an equivalent noise temperature of $T_{\text{min}} = 35\text{K}$ at $\theta = 1°$, but deviates considerably for all other scan angles[7].

[7]Similar results can be found, for example, in [52] and [51]. However, the effects of noise matching in these references are conducted on isolated arrays, and not array feeds. The substantial deviation from T_{min} seen in Figure 3.13 is due to the drastic changes in excitation weights to achieve scanning with.

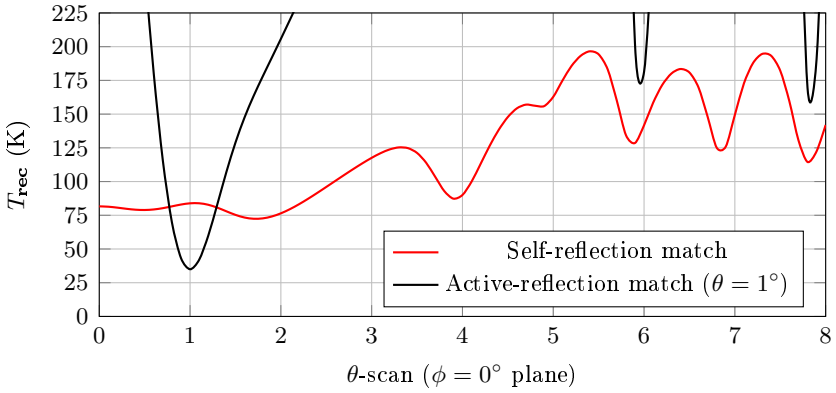

Figure 3.13: Equivalent receiver temperature T_{rec} as a function of θ-scan angle for various noise matching strategies.

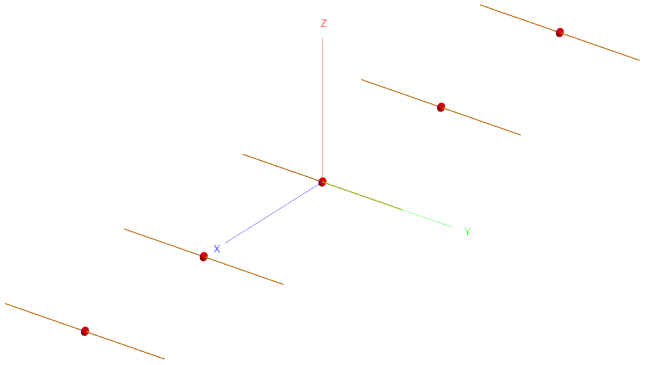

Figure 3.14: 5 element linear dipole array.

3.5 Model Validation

In order to validate the PAF modelling tools that has been developed, a comparison is made against the numerical results from [52]. A linear array of 5 half-wave dipoles is constructed in FEKO, as shown in Figure 3.14, and the array is simulated and modelled according the workflow of Figure 3.5. Next, the beam equivalent receiver noise temperature T_{rec} is calculated as a function of beam steering in the array H-plane. The LNA input impedances are assumed to be matched ($S_{11}^{\text{LNA}} = 0$), and noise parameters are chosen as $R_n = 10\ \Omega$ and $T_{\text{min}} = 20$ K, similar to the set-up in [52, Section IV (B)].

Figure 3.15 shows the resulting beam equivalent receiver noise temperature for the CFM beamforming weights in [52, eq (20)], and for two different noise matching strategies. In the first method, the optimal noise reflection coefficients $\Gamma_{opt,n}$ are chosen so that

$$Z_{opt,n} = Z_{A,nn}, \tag{3.35}$$

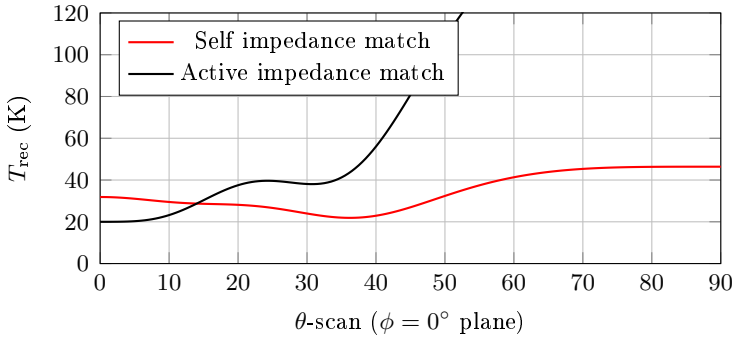

Figure 3.15: Equivalent receiver temperature T_{rec} as a function of θ-scan angle for linear 5 element dipole for comparison to [52].

where $\Gamma_{opt,n} = (Z_{opt,n} - Z_o)/(Z_{opt,n} + Z_o)$, and $Z_{A,nn}$ is the self impedance of element n. Note that this noise matching strategy is similar to (3.34). Also shown in Figure 3.15 is the result obtained for using active-reflection coefficients according to (3.32) for boresight reception ($\theta = 0°, \phi = 0°$). These results agree with that obtained from [52, Figure 5], and slight discrepancies may arise due to the FEKO modelling used here, and theoretical dipole models used in [52].

3.6 Concluding Remarks

This chapter has described the simulation and modeling of PAFs and array receiver networks, and has included some details on the developed numerical model and framework. The example using the 15-element dipole PAF has shown some and beamsteering and beamforming strategy effects, and the effects of different noise matching strategies, when using the developed numerical tools. Finally, the numerical tool accuracy is validated against results obtained from an existing article [52].

Chapter 4

Considerations on Cost Reduction of Array Receivers by Using Passive Elements

A reasonable assumption in phased array feeds is that more feed elements would generally provide better performance in terms of system gain and scanning range, at least while feed blockage is negligible. However, a major concern in multi-receiver systems is the cost of having multiple receiver chains and the additional digital hardware associated with them. In addition, the overall system receiver noise increases as more elements are added. Thus it seems reasonable to investigate possible ways of reducing the amount of receiver channels, while still trying to maintain desired performance results, which is the focus of this chapter.

4.1 General Formulation

The network formulation is perhaps best illustrated with the reciprocity relation and the impedance formulation from Section 3.2.1. Recalling the array receiver from Figure 3.3 in which all elements are beamformed, the output voltage can be expressed as a function of incident plane-wave angle in terms of the array OC-EEPs as,

$$v_{out}(\theta, \phi) = C_k \mathbf{w}^{\dagger} \mathbf{Q} \mathbf{F}_{oc}(\theta, \phi), \tag{4.1}$$

where, in the case of identical receiver chains with input impedances Z_L, $\mathbf{Q}$ can be expressed as

$$\mathbf{Q} = g Z_L (\mathbf{Z}_A + Z_L \mathbf{U})^{-1}. \tag{4.2}$$

This will be considered the "all-active" case. The goal then is to modify (4.2) by reducing the number of active receiver chains by passively terminating some elements. This would result in a new $(M \times N)$ matrix $\mathbf{Q}^{(\mathrm{R})}$ (where

$M < N$), corresponding to only M active receiver channels, which will be called the "reduced-active" case. The beamformed output voltage for the "reduced-active" receiver then takes the general form,

$$v_{out}^{(\mathrm{R})}(\theta,\phi) = C_k \mathbf{w}^{(\mathrm{R})\dagger} \mathbf{Q}^{(\mathrm{R})} \mathbf{F}_{oc}(\theta,\phi) \tag{4.3}$$

where $\mathbf{w}^{(\mathrm{R})} \in \mathbb{C}^{M\times 1}$ contains the beamforming weights applied only to the M active channels.

An interesting point to realize in (4.3) is that all the OC-EEPs are still participating in the beamformed output voltage of the receiver. Stated more formally, v_{out} and $v_{out}^{(\mathrm{R})}$ are ultimately, so long as mutual coupling is present, linear combinations of the same N 'basis' functions $\vec{\boldsymbol{f}}_n^{oc}$, but with different coefficients. From this, it is postulated that it might be possible to achieve close to the same performance of an all-active receiver with less active receiver chains by exploiting the effects of mutual coupling between antenna array elements and their corresponding EEPs.

4.2 Network Formulation Including Passive Elements

Figure 4.1a shows an array receiver for the case where only M array elements have active receiver chains, with the remaining $P = (N-M)$ elements passively terminated. It is convenient to view this array as a *new* antenna with only M ports, and accepting the passive elements as internally part of this new antenna. In view of this, the original array scattering matrix $\mathbf{S}_A$ is decomposed into active- and passive parts [41],

$$\mathbf{S}_A \Rightarrow \begin{bmatrix} \mathbf{S}_A^{\mathrm{actact}} & \mathbf{S}_A^{\mathrm{actpas}} \\ \mathbf{S}_A^{\mathrm{pasact}} & \mathbf{S}_A^{\mathrm{paspas}} \end{bmatrix}. \tag{4.4}$$

Note that $\mathbf{S}_A^{\mathrm{actact}}$, $\mathbf{S}_A^{\mathrm{actpas}}$, $\mathbf{S}_A^{\mathrm{pasact}}$ and $\mathbf{S}_A^{\mathrm{paspas}}$ are matrices of sizes $(M \times M)$, $(M \times P)$, $(P \times M)$ and $(P \times P)$ respectively. A new network relationship for the reduced-active array antenna $\mathbf{S}_A^{(\mathrm{R})}$ can then be formed as (see Figure 4.1b)

$$\mathbf{b}_A^{(\mathrm{R})} = \mathbf{S}_A^{(\mathrm{R})} \mathbf{a}_A^{(\mathrm{R})} + \mathbf{c}_A^{(\mathrm{R})}, \tag{4.5}$$

where $\mathbf{S}_A^{(\mathrm{R})}$ and $\mathbf{c}_A^{(\mathrm{R})}$ are related to the original network parameters according to [45]

$$\mathbf{S}_A^{(\mathrm{R})} = \mathbf{S}_A^{\mathrm{actact}} + \mathbf{S}_A^{\mathrm{actpas}} \left(\mathbf{U} - \mathbf{S}_P \mathbf{S}_A^{\mathrm{paspas}}\right)^{-1} \mathbf{S}_P \mathbf{S}_A^{\mathrm{pasact}} \tag{4.6}$$

$$\mathbf{c}_A^{(\mathrm{R})} = \mathbf{c}_A^{\mathrm{act}} + \mathbf{S}_A^{\mathrm{actpas}} \left(\mathbf{U} - \mathbf{S}_P \mathbf{S}_A^{\mathrm{paspas}}\right)^{-1} \mathbf{S}_P \mathbf{c}_A^{\mathrm{pas}} \tag{4.7}$$

The $(P \times P)$ diagonal matrix $\mathbf{S}_P$ contains the reflection coefficients of the passive element loads[1],

$$S_{P_n} = \frac{Z_{P_n} - Z_o}{Z_{P_n} + Z_o}. \tag{4.8}$$

The resulting receiver network is shown in Figure 4.1c, and the network equations can be set-up as,

$$\begin{bmatrix} \mathbf{b}_{out}^{\text{LNA}} \\ \mathbf{b}_{in}^{\text{LNA}} \\ \mathbf{b}_{A}^{(\text{R})} \end{bmatrix} = \begin{bmatrix} \mathbf{S}_{22}^{\text{LNA}} & \mathbf{S}_{21}^{\text{LNA}} & \mathbf{0} \\ \mathbf{S}_{12}^{\text{LNA}} & \mathbf{S}_{11}^{\text{LNA}} & \mathbf{0} \\ \mathbf{0} & \mathbf{0} & \mathbf{S}_{A}^{(\text{R})} \end{bmatrix} \begin{bmatrix} \mathbf{a}_{out}^{\text{LNA}} \\ \mathbf{a}_{in}^{\text{LNA}} \\ \mathbf{a}_{A}^{(\text{R})} \end{bmatrix} + \begin{bmatrix} \mathbf{c}_2 \\ \mathbf{c}_1 \\ \mathbf{c}_{A}^{(\text{R})} \end{bmatrix}. \tag{4.9}$$

This is quite convenient, since (4.9) is identical to (3.10) (see Figure 3.4) except for the replacement of $\mathbf{S}_A$ and $\mathbf{c}_A$ with $\mathbf{S}_A^{(\text{R})}$ and $\mathbf{c}_A^{(\text{R})}$ respectively, and noting that all matrices and vectors in (4.9) are of size $(M \times M)$ and $(M \times 1)$ respectively. Hence, the same procedure for calculating the signal and noise correlation matrices at the receiver output can be carried out as in Section 3.2.2, which will not be repeated here.

With the end goal of expressing $\mathbf{v}^{(\text{R})}$ in terms of the original array open-circuit voltages $\mathbf{v}_{oc}$, and to properly keep track of active and passive port numbering, two "port mapping" matrices can be defined as,

$$\mathbf{c}_A^{\text{act}} = \mathbf{\Gamma}^{\text{act}} \mathbf{c}_A, \tag{4.10a}$$
$$\mathbf{c}_A^{\text{pas}} = \mathbf{\Gamma}^{\text{pas}} \mathbf{c}_A, \tag{4.10b}$$

where $\mathbf{\Gamma}^{\text{act}} \in \mathbb{N}^{M \times N}$ and $\mathbf{\Gamma}^{\text{pas}} \in \mathbb{N}^{P \times N}$ contain only ones and zeros. Substituting (4.10) into (4.7), and using the transformation matrix $\mathbf{L}$ from (3.15), $\mathbf{v}^{(\text{R})}$ can be expressed as,

$$\mathbf{v}^{(\text{R})} = \sqrt{Z_o}\mathbf{TPL}\mathbf{v}_{oc} \tag{4.11}$$

where,

$$\mathbf{P} = (\mathbf{\Gamma}^{\text{act}} + \mathbf{S}_A^{\text{act pas}}(\mathbf{U} - \mathbf{S}_P\mathbf{S}_A^{\text{paspas}})^{-1}\mathbf{S}_P\mathbf{\Gamma}^{\text{pas}}) \tag{4.12}$$

and (see also (3.12)),

$$\mathbf{T} = \mathbf{S}_{21}^{\text{LNA}}(\mathbf{U} - \mathbf{S}_A^{(\text{R})}\mathbf{S}_{11}^{\text{LNA}})^{-1} \tag{4.13}$$

Hence, a new transformation matrix $\mathbf{Q}^{(\text{R})}$ has been obtained which is defined as,

$$\mathbf{Q}^{(\text{R})} = \sqrt{Z_o}\mathbf{TPL}. \tag{4.14}$$

The network formulation will next be applied to two example arrays.

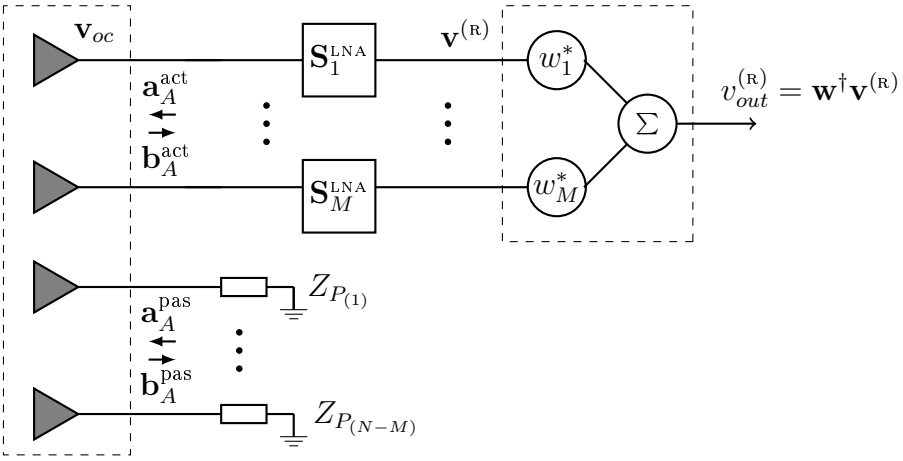

(a) N element array receiver with $P = (N - M)$ passive elements.

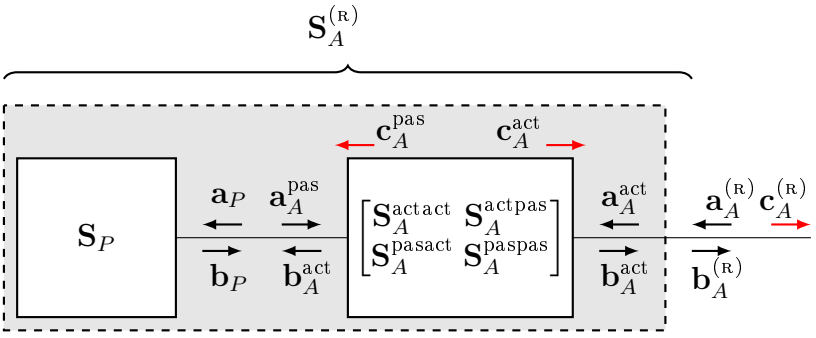

(b) Formation of new antenna scattering matrix $\mathbf{S}_A^{(\text{R})}$.

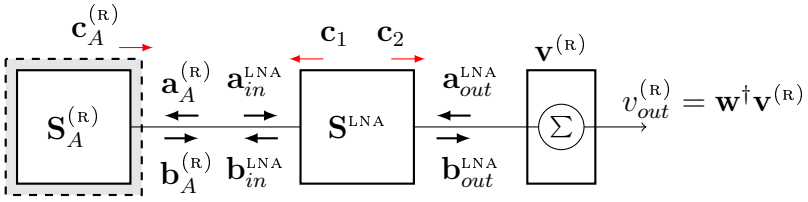

(c) Resulting receiver network model.

Figure 4.1: Scattering parameter description of reduced-active array receiver.

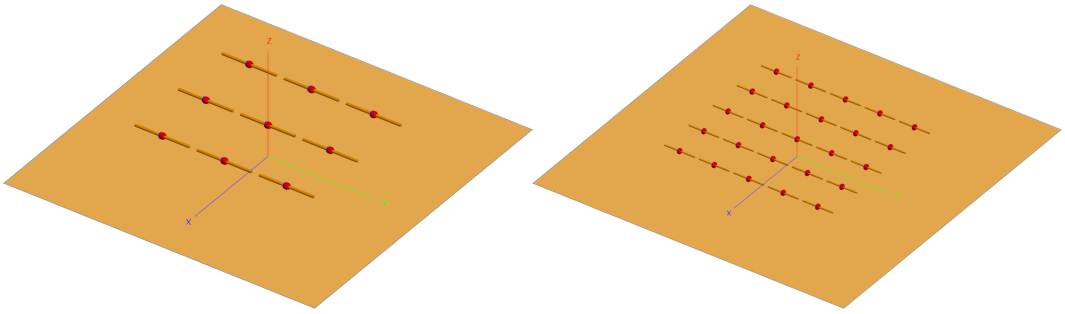

(a) (3×3) (b) (5×5)

Figure 4.2: FEKO models of half-wave dipole arrays above infinite ground plane.

4.3 Dipole Array Example

Shown in Figure 4.2 are FEKO models of (3×3) and (5×5) very simple half-wave dipole arrays above an infinite ground plane[2]. Each dipole is fed at its centre with a wireport, and models are applied as equivalent point sources to a reflector of $D = 50\lambda$ and $F/D = 0.4$. The procedure for the study is as follows:

1. The (3×3) and (5×5) arrays are simulated as "all-active" and the achievable G/T is obtained across some angular region of interest.

2. The (5×5) array is modified to a "reduced-active" case, where only 9 active elements are allowed with the rest passively terminated.

3. A comparison is made between the achievable G/T of the "all-active" and "reduced-active" (5×5) arrays, while also comparing performance to the (3×3) "all-active" array.

Seven different 'reduced-active' cases are considered, shown in Figure 4.3. In each case, the self-reflection coefficient noise matching strategy is used for each LNA, so that $\Gamma_{opt,n} = S^{(\mathrm{R})}_{A,nn}$ (see Section 3.4.3), and with $R_n = 10\,\Omega$ and $T_{min} = 35\mathrm{K}$. Additionally, optimal beamforming weights $\mathbf{w} = \mathbf{w}_{\mathrm{SNR}}$ (see Section 2.5.1) are applied for each scan angle. Three terminations are considered for the passive cases: 1) impedances identical to the LNA input impedances (in this case 50 Ω), 2) short-circuits and finally 3) open-circuits.

[1]Using an S-parameter formulation removes any issues regarding defining infinite impedances/admittances for open/short circuits numerically. The results from Section 2.4 can also be used to overcome these issues.

[2]Naturally, an infinite ground plane is in no way practical. However, this model has only been used to investigate the concept.

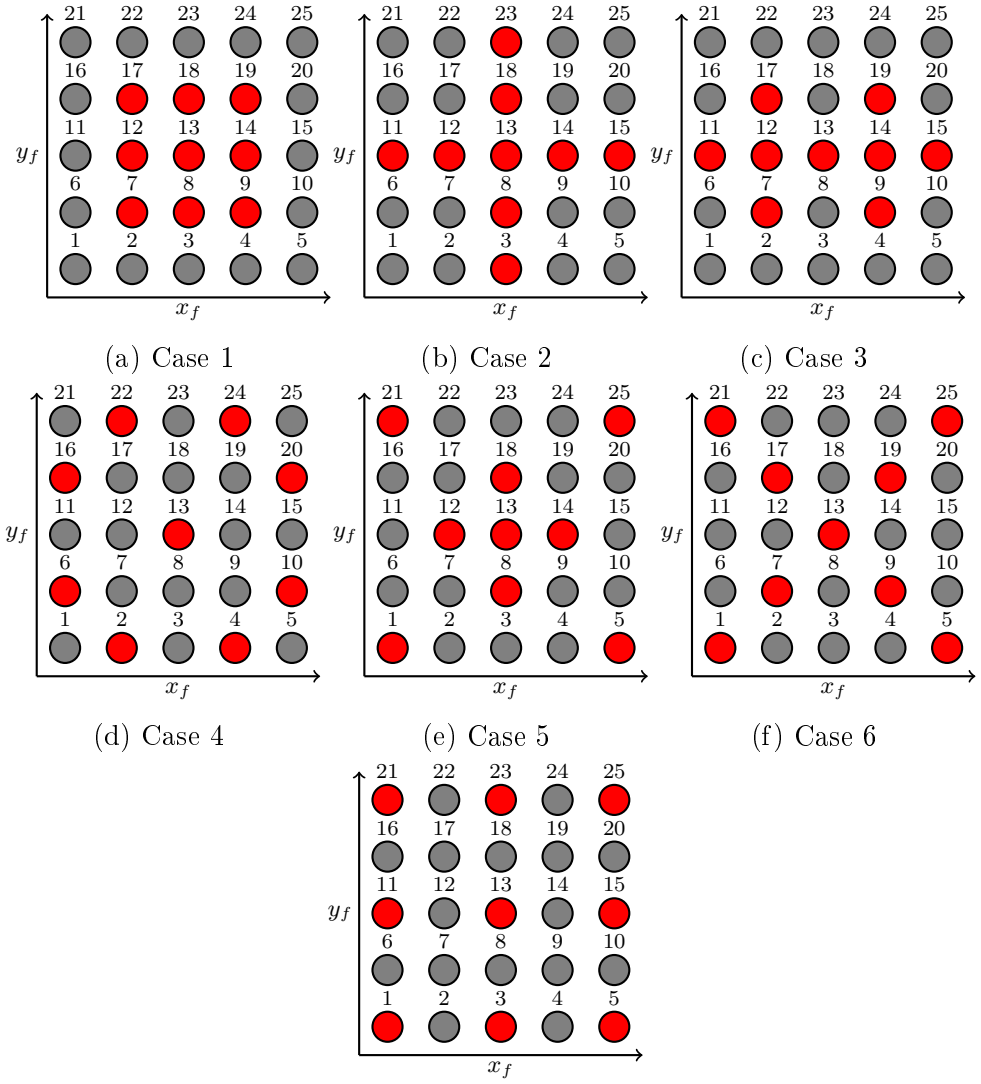

(a) Case 1 (b) Case 2 (c) Case 3

(d) Case 4 (e) Case 5 (f) Case 6

(g) Case 7

Figure 4.3: Different configurations of passive elements possible with two symmetry planes and 9 active receivers. Active and passive elements are indicated in red and black respectively.

Numerical Results

Figure 4.4 shows the achieved system G/T as a function of θ-scan angle for a $\phi = 0°$ plane. Recalling the discussion of focal field distributions from Section 2.2.3, this scan results in the Airy-pattern shifting along x_f, with the main-lobe centre crossing elements 11 - 15. A few comments are in order for these results.

Firstly, for all three terminations from Case 1, the performance and scan range is similar to that of the (3×3) all-active receiver, and in some cases even worse. In addition, clear dips are visible in performance where the focal field distributions would shift across passive elements (compare for instance, the scan range of Cases 2 and 3 to Cases 4 and 6, and the intuitive dip-and-rise of Case 7), although it appears that lower dips results from short-circuit termination as compared to loaded or open-circuits.

In the scenario with 50 Ω terminations on the passive elements (Figure 4.4a), all cases perform rather poorly, even compared to (3×3) 'all-active' receiver. Since the passive array elements are considered *as part* of a new reduced-active array receiver, power dissipated in the passive loads degrades the antenna radiation efficiency η_{rad}, which in turn contributes significantly to noise generated by ambient temperature antenna losses (an ambient temperature of 300K as been used in this case).

Initially, it was believed that short-circuit termination scenario would result in the best performance, the reason being that coupling in this case would be the greatest, since a half-wave dipole with short-circuit at its centre is essentially just a parasitic radiating wire. However, Figure 4.4b shows that, although the performance is in most cases superior to the loaded scenario from Figure 4.4a, it is still relatively poor in terms of G/T. The reason is based on the fact that the short-circuit terminations drastically change the EEPs of the reduced-active receiver.

The open circuit scenario from Figure 4.4c shows the interesting result that in some cases, specifically Cases 2 and 3, the 'reduced-active' receiver actually performs better in terms of G/T than the (5×5) 'all-active' receiver. To explain this anomaly, it should be mentioned that a dipole is considered a single-mode antenna [26], and terminating its centre with an open-circuit essentially forces this single-mode to zero. Loosely, it becomes 'invisible' at its resonant frequency, contributing little in terms of radiation and mutual coupling. The superior performance for open-circuit Cases 2 and 3 in Figure 4.4c results from the fact that, for the $\phi = 0°$ scan-range considered, the negative impact of the outer elements' receiver noise on the overall system temperature T_{sys} outweigh their contribution to the antenna gain; hence, removing those elements would be preferable in this specific case. This is an interesting obser-

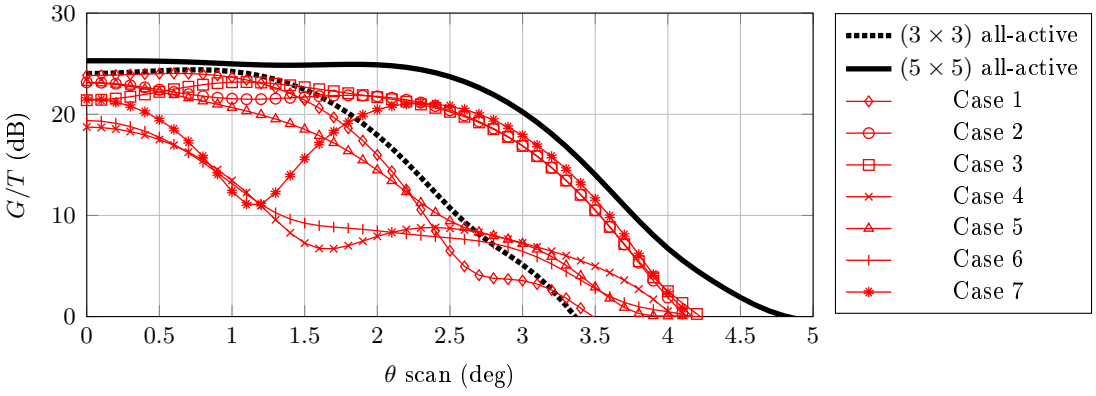

(a) Loaded (50Ω)

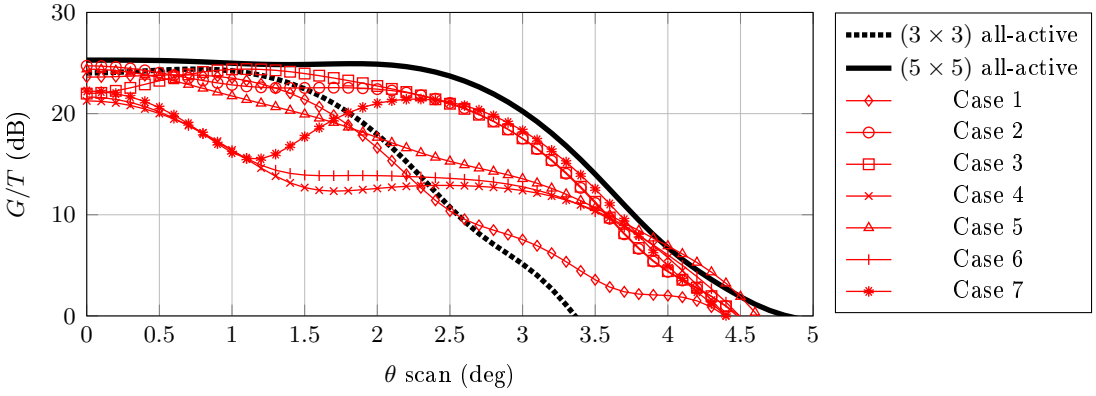

(b) Short-circuits

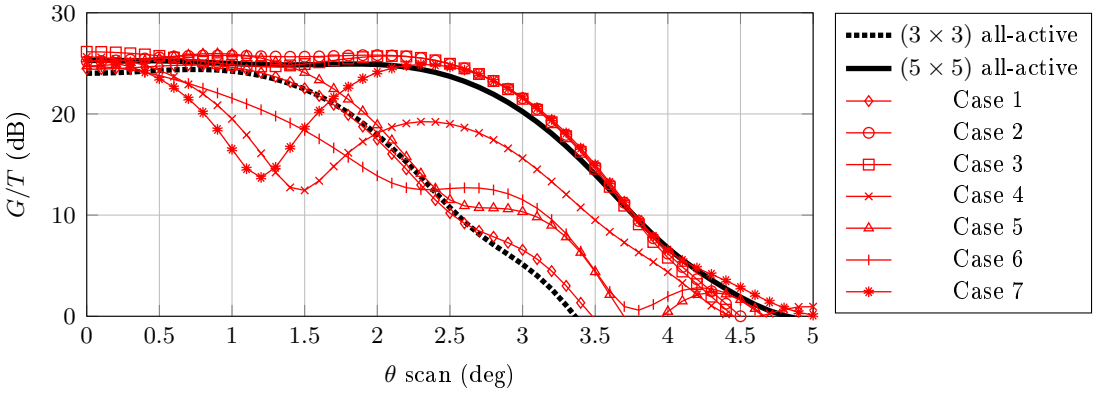

(c) Open-circuits

Figure 4.4: G/T as a function of $\phi = 0°$ scan for dipole array according to various cases of passive elements terminated with impedances a) 50Ω, b) short-circuits c) open circuits.

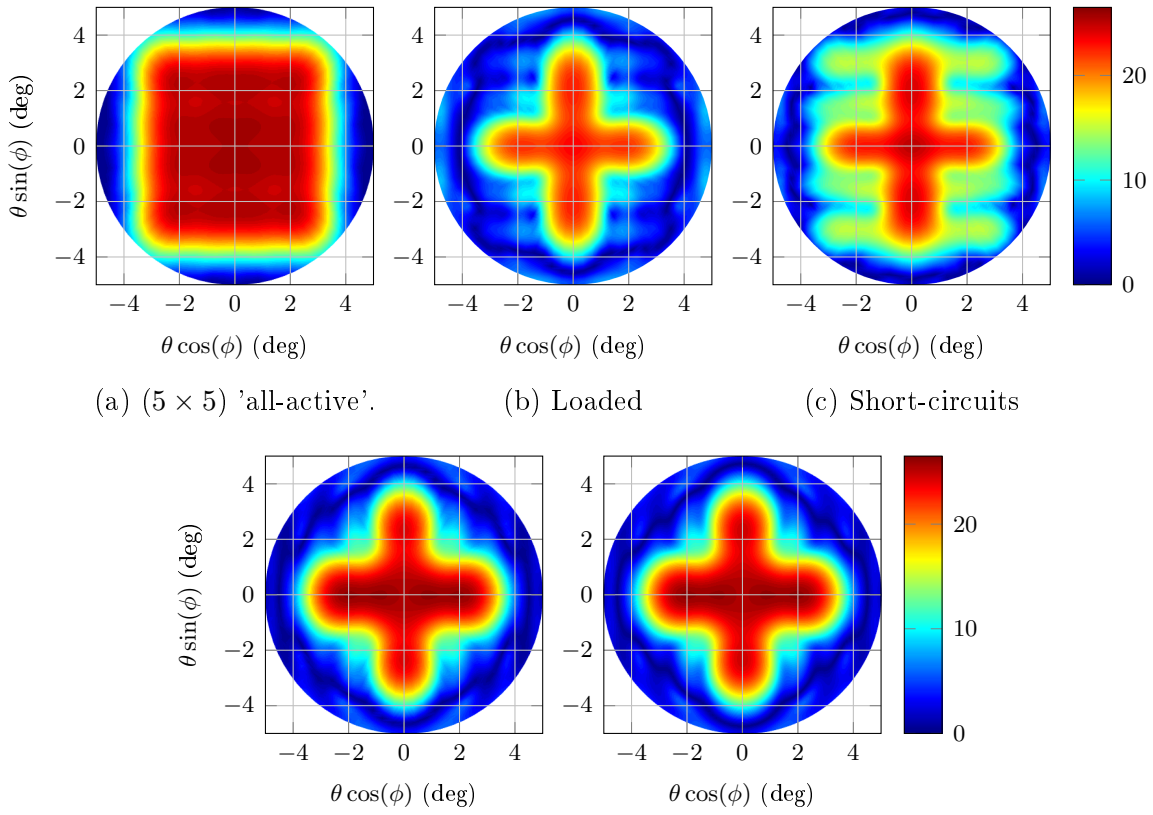

(a) (5×5) 'all-active'. (b) Loaded (c) Short-circuits

(d) Open-circuits (e) 9 element array

Figure 4.5: Calculated G/T (dB) for the a) 'all-active' and 'reduced-active' receiver based on Case 2, with b) passive loads c) short-circuits d) open-circuits and e) 9 element array spaced according to the active locations from Case 2

.

vation, and will be studied further in Chapter 5.

A better overall illustration is included in Figures 4.5 and 4.6, which shows the calculated G/T for the (5×5) all-active receiver along with the three different terminations for Cases 2 and 3 as a function for all ϕ-scan angles. Note how the UV-scan angle plots follow the general shape of active-elements. Here, the effect of stronger coupling for short-circuit terminations is more apparent, as Figures 4.5c and 4.6c seem to show some G/T performance for scan-angles where the loaded and open-circuit scenarios do not. To verify the minimal effect of open-circuited dipoles, additional FEKO models were simulated with only 9 elements arranged according to the active-element positions from Cases 2 and 3, and the calculated G/T is shown in Figures 4.5e and 4.6e, which is seen to be essentially identical to the open-circuit cases.

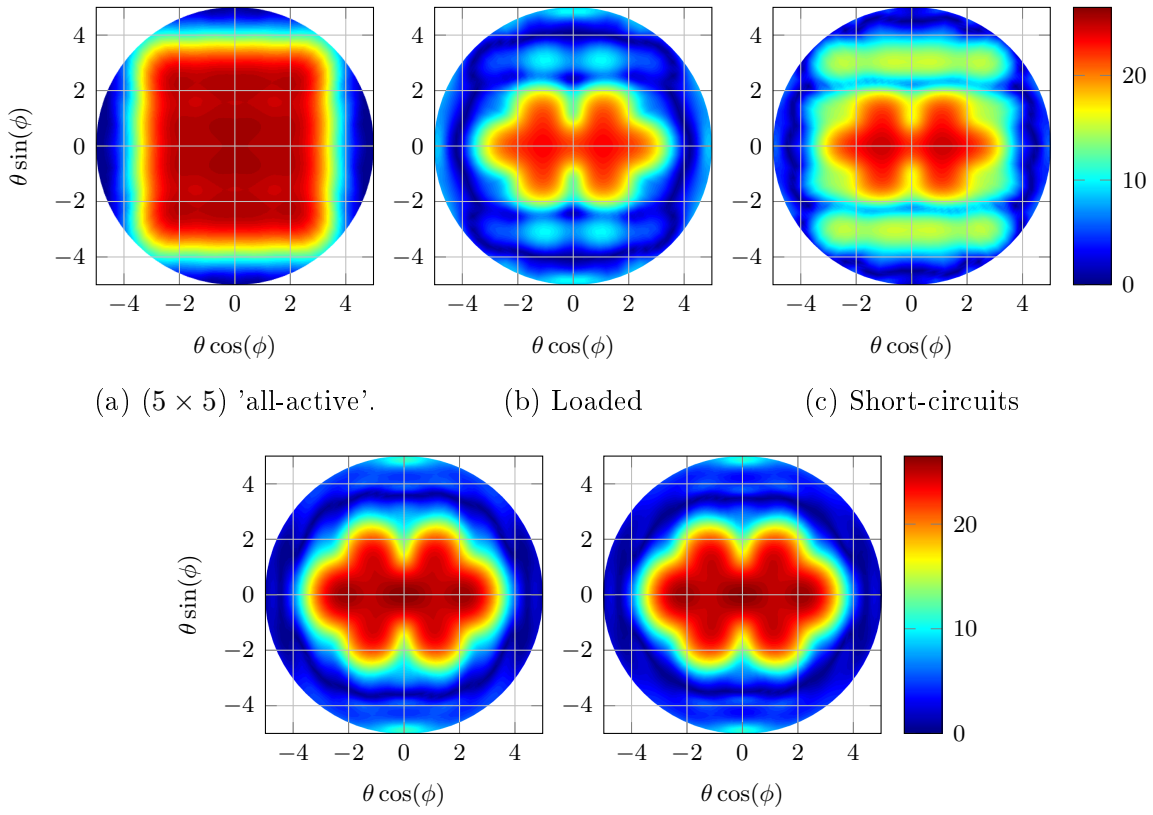

(a) (5×5) 'all-active'. (b) Loaded (c) Short-circuits

(d) Open-circuits (e) 9 element array

Figure 4.6: Calculated G/T (dB) for the a) 'all-active' and 'reduced-active' receiver based on Case 3, with b) passive loads c) short-circuits d) open-circuits and e) 9 element array spaced according to the active locations from Case 3

.

4.4 Concluding Remarks

Admittedly, the results of this study has not entirely satisfied the initial hypothesis, which is the idea that overall comparable performance of an all-active receiver can be obtained with less active elements. While the short circuit scenarios in Figures 4.5c and 4.6c showed some signs of potential performance, the results are in no way refined. Future studies could perhaps include elements with stronger coupling, considered different termination values, and perhaps more complicated passive structures other than identical antenna elements which could couple energy to active receiver channels.

One important factor which has been illustrated in this chapter is the fact that more array elements is not always better in terms of G/T performance, and it is important to consider the amount of array elements in context of intended application and to consider that some elements may generally have a negative impact on system G/T. This idea is studied further in Chapter 5.

Chapter 5

Considerations on the Optimal Number of Elements For Single-Plane Scanning

A potential application for PAFs in downlink satellite communication links is the ability of a ground station to simultaneously resolve several satellites lying on the geosynchronous Earth orbit (GEO). For this specific case, scanning in a single angular-plane is mostly sufficient, as satellites are stacked side-by-side along the orbit arc [11]. If it can be assumed that the feed can be rotated on its axis, orbit arc curvature effects could also be mitigated.

Chapter 4 showed the interesting result of superior G/T performance for a one-dimensional scan when the number of elements was decreased, since the negative impact on receiver noise of some array elements outweigh their contribution to the overall system gain. From this follows an interesting question: for a one-dimensional angular scan requirement, under what conditions would more array elements provide better G/T performance? The results from Section 4.3 seem to suggest that a simple linear array might be the best choice. However, what are the effects when the equivalent noise temperature of the front-end LNAs can be lowered? Is it perhaps possible to decrease receiver noise by combining certain elements into a single-receiver chain? This chapter is an attempt at gaining some insight to these questions, and in context of scanning in a single angular plane.

5.1 Preliminary Details

In this study, simple (slightly shorter than) half-wave dipoles placed a quarter-wavelength ($\lambda/4$) above a finite ground plane are used as array elements. Three different configurations are considered, each with an increasing number of elements, as shown in Figure 5.1.

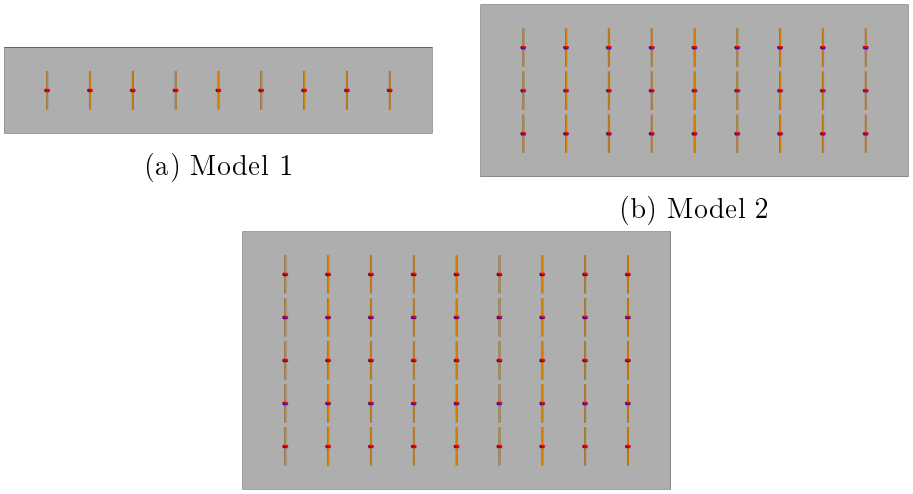

(a) Model 1

(b) Model 2

(c) Model 3

Figure 5.1: Top view of three array configurations configurations of half-wave dipoles.

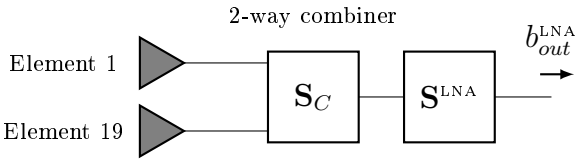

Figure 5.2: Illustration of combining elements 1 and 19 for array Model 2.

The simplest configuration, Model 1, is a linear array consisting of 9 elements, where each element is connected to an individual receiver chain. Hence, a total of 9 LNAs are present in the receiver chain.

In Model 2, two additional element 'rows' are added to form a (9×3) planar array. Additionally, elements across one-another are assumed to be connected together via 2-way power combiners, which results in only 18 receiver chains, and hence 18 LNAs. An illustration of the combiner circuit for elements[1] 1 and 19 is given in Figure 5.2. The combiner scattering matrix model used is defined according to

$$\mathbf{S}_C = \frac{1}{\sqrt{2L}} \begin{bmatrix} 0 & 1 & 1 \\ 1 & 0 & 0 \\ 1 & 0 & 0 \end{bmatrix}, \tag{5.1}$$

where the additional loss factor L is chosen such that the total insertion loss is 3.5 dB[2] in order to account for possible combiner and transmission line losses.

[1] Element indexing follows the convention of Figure 2.9

[2] This is 0.5 dB above the theoretical 3 dB insertion loss inherent in typical passive 2-way combiners.

The combiners are considered as part of the array antenna, and thus any combiner losses will be considered as degrading the antenna radiation efficiency η_{rad}. Details on the network formulation for including computers are omitted here, but can be obtained in a similar way as Chapter 4.

The largest array configuration shown in Model 3 consists of 45-elements arranged in a (9×5) grid, where each element is considered connected to individual receiver chains. Hence a total of 45 LNAs are present in the receiver chain. The configurations have been chosen in this manner so that Models 1 and 3 can be considered as opposite extremes, and Model 2 as some trade-off in between.

The element spacing in all cases is $\lambda/2$, and LNAs are assumed to be match terminated with scattering parameters of $S_{11}^{\text{LNA}} = 0.1$ and $S_{21}^{\text{LNA}} = 15$.

The arrays were simulated in isolation to obtain the primary EEPs, and applied to a reflector of $D = 50\lambda$ and $F/D = 0.4$ as equivalent point sources to obtain the secondary EEPs. The brightness noise temperature model is obtained from [46].

In the upcoming Sections 5.2 and 5.3, two studies are conducted to gain some insight into in the performance differences between the various models caused by different beamforming strategies and receiver noise parameters.

5.2 Effect of Beamforming Technique

In this section, LNA noise parameters are considered fixed with values $T_{\text{min}} = 75$ K, $R_n = 5\ \Omega$ and $\Gamma_{opt} = 0$, and the beam-scanning angle is varied across the H-plane ($\phi = 0°$). For each scan-angle, the system G/T is calculated for both conjugate field matching $\mathbf{w} = \mathbf{w}_{\text{CFM}}$ and maximum-SNR $\mathbf{w} = \mathbf{w}_{\text{SNR}}$ beamforming weights, in order to obtain an indication of the effect on various efficiencies and noise temperatures.

5.2.1 Simulation Results

The simulated aperture- and radiation efficiencies, along with the antenna gain are shown in Figure 5.3 for a θ-scan up to 8°, where CFM- and max-SNR beamforming results are indicated by solid and dashed lines, respectively.

Focusing first on the CFM-case, Figure 5.3a illustrates the expected result that the largest array configuration, Model 3, results in the highest aperture efficiency, owing to the fact that it 'collects' more signal power scattered by the reflector into the focal plane. In contrast, Model 1 performs the poorest in

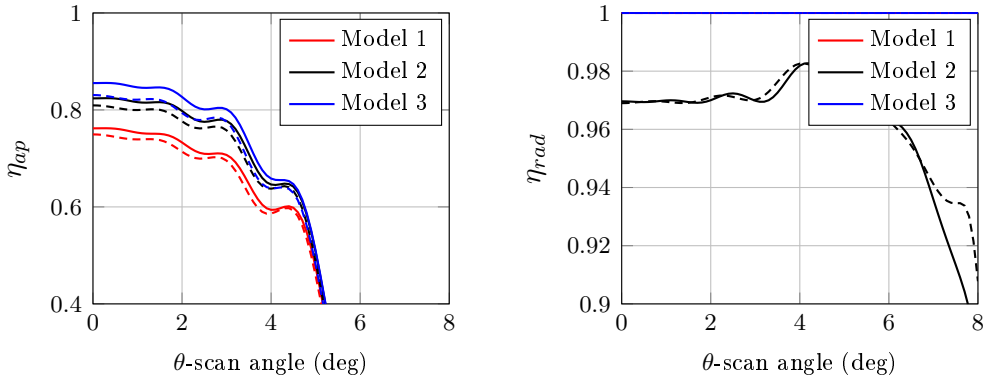

(a) Aperture efficiency.

(b) Radiation efficiency.

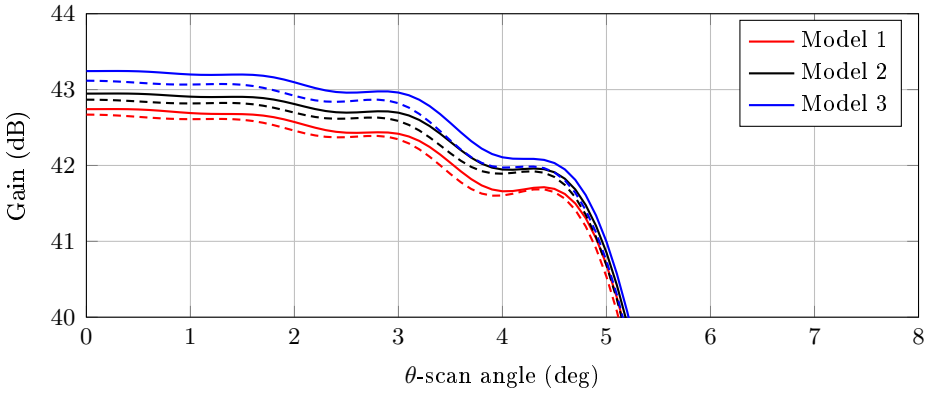

(c) Antenna gain, $G = \eta_{ap}\eta_{rad}D_{o,\max}$

Figure 5.3: Simulated results of a) aperture efficiency b) radiation efficiency and c) gain. Solid and dashed lines represent CFM beamforming and Max-SNR beamforming results, respectively.

terms of aperture efficiency, while Model 2 achieves performance somewhere between these two extremes. For all three models, the max-SNR beamformers results in degrading the aperture efficiency, although the effect thereof seems to be largest for Model 3. This result will be discussed shortly. Note that all Models achieve a similar scan range up to about 5°.

In terms of radiation efficiency, Figure 5.3b indicates that only Model 2 suffers from ohmic losses in the antenna, which is due to the presence of the nine lossy combiners included in its receiver chain. The beamforming strategy used is also seen to have little effect on the radiation efficiency. The dipole elements have been simulated as perfect electric conductors (PEC) in FEKO, hence Models 1 and 3 show no ohmic losses ($\eta_{rad} = 1$). Note that blue and red lines are overlapped in Figure 5.3b.

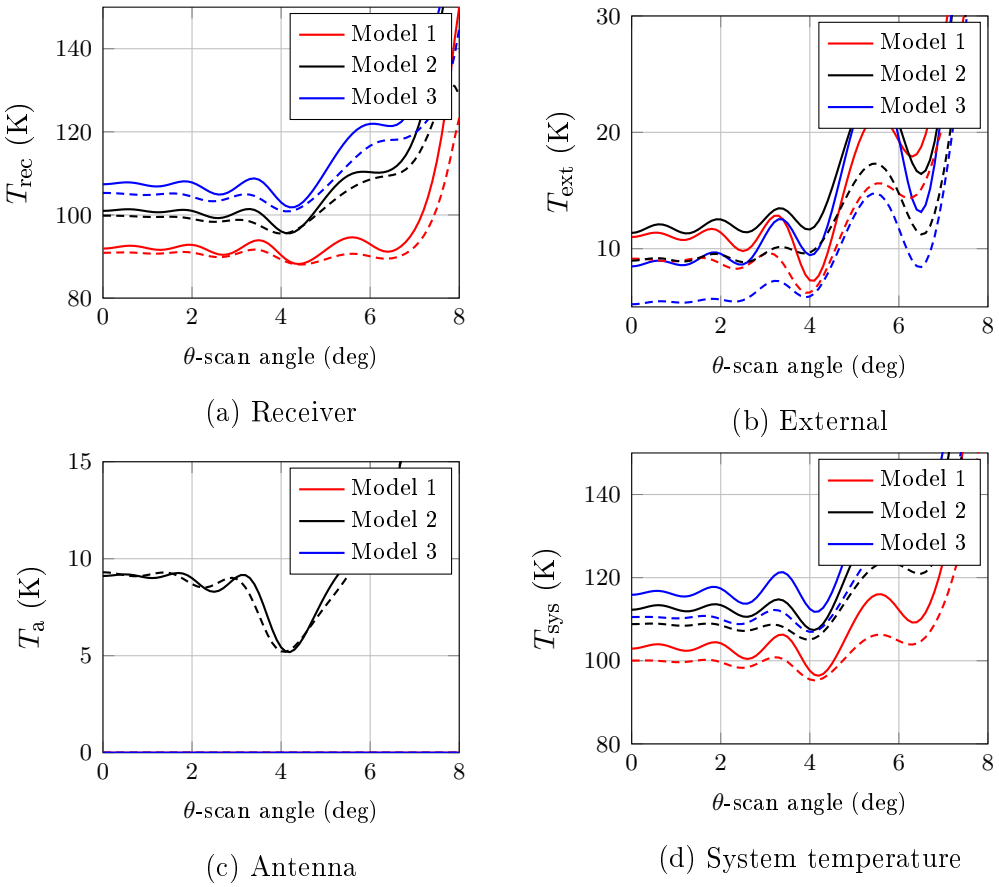

(a) Receiver

(b) External

(c) Antenna

(d) System temperature

Figure 5.4: Beam equivalent noise temperatures of a) receiver noise b) external noise c) antenna ohmic losses d) entire system. Solid and dashed lines represent CFM and Max-SNR beamforming results, respectively.

The various beam-equivalent temperatures are shown in Figure 5.4. Immediately apparent from Figure 5.4a is the effect that the amount of LNAs present in the receiver chains has on the receiver noise, as Models 1 and 3 show a difference of around 20 K for T_{rec}, with Model 2 lying in between. Additionally, the minimizing effect of max-SNR beamforming on T_{rec} seems to be most pronounced for Model 3, which perhaps also explains the larger effect on the aperture efficiency degradation for Model 3 in Figure 5.3a, when considering the fact that mitigating higher amounts of noise mostly likely requires more drastic changes of beamformer weights.

Figure 5.4b shows the superior performance of Model 3 in mitigating external noise, which can be expected due to the ability of the larger array size in constraining the feed pattern within the reflector angular region. Perhaps not so intuitive is the higher external noise temperature for Model 2 compared to Model 1. It would appear that, while the (9×3) grid size of Model 2 achieves

better overall reflector illumination as compared to Model 1, it lacks the ability of Model 3 to properly contain the feed pattern within the reflector angular region.

The total system temperature for the various Models is in Figure 5.4d, and indicates the expected results of Model 3 having the most noise dominated receiver. Additionally, the effect of max-SNR beamforming seems to have the most pronounced effect on Model 3. With max-SNR beamforming, Model 1 obtained a total system temperature of around ≈ 100 K.

All of the above mentioned comments are concisely summarised in Figure 5.5, which shows the achieved beam equivalent system G/T for all models. It appears that by starting with the linear array of Model 1, and adding more elements in an attempt to improve aperture efficiency and system gain, one is brought around full circle in terms of G/T, as Figure 5.5 shows an almost identical performance when using either a 9- or 45-element array. This is a valuable observation, given that there is certainly a difference in cost between 9 and 45 receiver chains. Through the complicated and various trade-offs between efficient reflector illumination and system temperature, it seems that essentially nothing has been gained by adding more elements, and suggests that it is best to make use of a linear array when scanning in only one-dimension is required. Figure 5.5 also reveals that it is most likely best to avoid any attempts at combining elements before LNAs, owing to the lower performance of Model 2 in comparison to either Models 1 and 3, due to the increased antenna losses in Model 2.

These results can not be considered conclusive just yet, as only dipoles elements have been considered here. Array elements with stronger or weaker coupling would perhaps perform entirely different. This study has, however, shown that in some cases less elements are preferable to more. These results have only been possible due to the developed numerical tools during this thesis.

In the next section, an investigation on varying the LNA noise parameters is considered.

5.3 Effect of Varying Receiver Noise Parameters

In the previous section, LNA noise parameters were held fixed, while considering variation in θ-scan angle. The present study will take an opposite approach, by keeping the scan-angle fixed, and varying the LNA noise parameters for the same three models of Figure 5.1. The goal is to discover at what

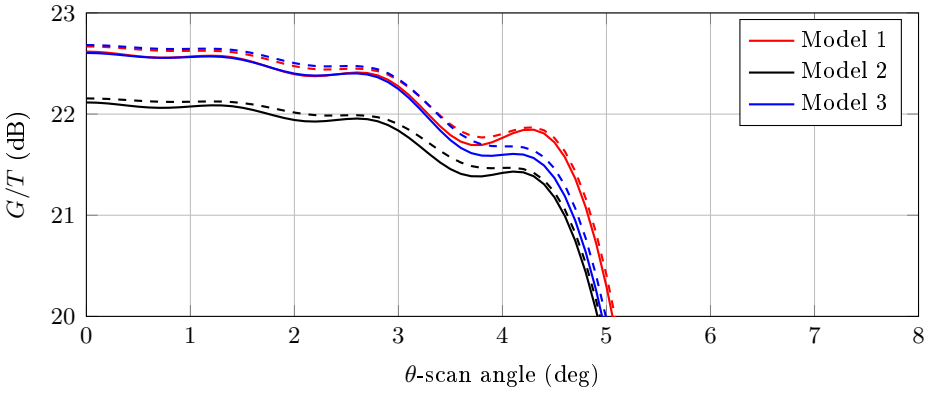

Figure 5.5: Beam equivalent system G/T as a function of θ-scan angle.

receiver noise temperature, if any, more elements would yield superior G/T performance, and then by how much.

The various efficiencies and beam equivalent noise temperatures will be calculated for a fixed scan-angle to boresight ($\theta = 0, \phi = 0$), while varying the minimum equivalent noise temperature T_{min} of all LNAs, for R_n values of 0 Ω, 5 Ω, 10 Ω and 15 Ω. The optimal reflection coefficient is assumed fixed to $\Gamma_{opt} = 0$. Finally, in all cases, max-SNR $\mathbf{w}_{\text{SNR}}$ beamforming weights are applied to ensure optimal SNR performance.

While varying the noise parameters, it is important to keep in mind that physically realizable parameters requires the following constraint condition to be satisfied [52, 49],

$$R_n \geq \frac{T_{\text{min}}}{4G_{opt}T_o}. \tag{5.2}$$

where G_{opt} is the real part of optimal admittance representation, $Y_{opt} = G_{opt} + jB_{opt}$, of the LNA optimal reflection coefficient Γ_{opt}. Thus, the case of $R_n = 0$ Ω is not physically possible, but is merely included for the sake of interest. For $\Gamma_{opt} = 0$, all other cases are possible up until $T_{\text{min}} \approx 115$ K.

5.3.1 Simulation Results

The resulting system G/T for boresight reception and calculated as a function of varying T_{min}, is shown in Figure 5.6 for R_n values of 0 Ω, 5 Ω, 10 Ω and 15 Ω respectively.

In the impossible case of $R_n = 0$ Ω, for extremely low receiver noise, Figure 5.6a indicates the superior performance of Model 3, showing an almost constant 1 dB improvement above Model 1. In hindsight of the previous section, this is an expected result. If the receiver noise can mostly be neglected,

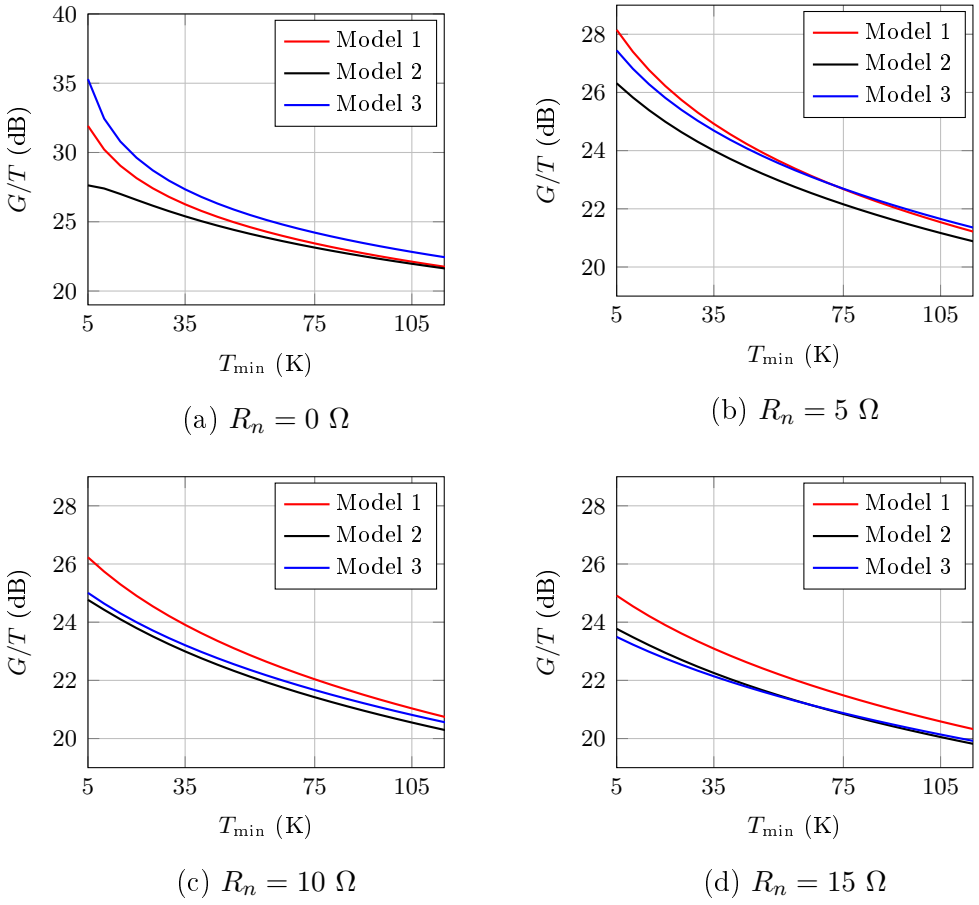

(a) $R_n = 0\ \Omega$ (b) $R_n = 5\ \Omega$

(c) $R_n = 10\ \Omega$ (d) $R_n = 15\ \Omega$

Figure 5.6: System G/T performance for bore-sight reception as a function of LNA equivalent minimum noise temperature T_{min}.

it is expected that the superior aperture efficiency and spill-over noise mitigation of Model 3 shown in Figures 5.3a and 5.4b would result in higher G/T performance.

Coincidently, Figure 5.6b shows that the noise parameters chosen in Section 5.2 lies around some trade-off point between Models 1 and 3. Increasing or lower T_{min} beyond 75 K results either in Model 3 or Model 1 starting to dominate. This is a very unexpected results, as it seems to go against the notion for the case of $R_n = 0\ \Omega$ discussed above. The conclusion for this result is not clear, but it is postulated that the effects of high receiver noise begins to saturate for the 45-element array, due to several of its elements not being used as strongly, allowing more freedom in beamforming weights to mitigate noise.

For Figures 5.6c and 5.6d, a trend starts to appear, as increasing R_n to higher values seems to shift Model 2 and 3 lower in performance, and the effect of Model 1 containing the least number of LNAs starts to become clear.

5.4 Concluding Remarks

The results presented in this chapter have revealed some interesting outcomes in the performance behaviour of various array feed configurations in terms of different beamforming techniques, and LNA receiver noise parameters when beam steering across a single-plane. It would appear that when the requirement is limited for scanning along a single angular plane, a simple linear array is the best option and most cost effective option.

Admittedly, there are various other aspects that can still be investigated, which could include the effects of various reflector F/D ratios, different choices for LNA optimal reflection coefficients Γ_{opt}, antenna tilt, element spacing and different elements to name a few. The study has shown just one of the many possible applications of PAF simulation model that has been developed during this thesis.

Chapter 6

Conclusion

6.1 Summary of Results

This thesis presents a general study on PAFs for paraboloidal reflector antennas. An efficient and versatile numerical simulation model has been developed which can be used to perform various parameters studies. The model accounts for the effects of receiver noise generated by front-end LNAs, as well as noise due to an external brightness temperature scene, and takes all mutual coupling effects into account. Additionally, the effects of including passive elements, as well as combining active elements, can be modelled. The model allows the simulation of the receiver SNR, and by extension the overall system G/T, which is the primary figure of merit for receiving antennas.

An illustration is given on various aspects such as beamsteering and different beamforming techniques by using an example 15-element dipole array PAF. An initial study was conducted regarding the possibility of reducing receiver costs by including passive elements in the array feed.

The possibility of reducing array receiver costs by utilizing passive elements is investigated. Here, it was found that more array elements are not always preferable, as the increase in receiver noise caused by a large number of receiver chains could dominate the overall system sensitivity. While this thesis has not been devoted specifically to a single design and design goal, the developed model can be used in future projects for modelling PAFs and array antenna in general.

Finally, a detailed investigation on the various trade-off between system gain and overall sensitivity shows that these effects are not always intuitive. Here, it was also demonstrated that when scanning only a single plane is required, linear array generally perform well. The thesis is concluded below with some recommendations for possible future projects.

6.2 Possible Topics for Future Work

At present, the developed numerical framework can be viewed as a high-level model, as it assumes linear operation of the entire system. A more rigorous model can include non-linearity effects of amplifiers and receiver chains. Additionally, while many aspects of the developed model are automated and easy to use, further simplifications and deeper integration between different various software packages would be of great benefit.

Another limitation of this study has been that once a PAF or general array model has been simulated in FEKO, parameters such as element positions have to remain fixed. The challenge in modelling different element positions is accurately and quickly accounting for mutual coupling effects after shifting elements around, since this requires recalculating the MoM matrix for the change. Possible solutions could include making use of charactersistic basis functions, or making use of the DGFM [38].

Efficient and rapid calculation of mutual coupling changes due to element position shifts could also be integrated with a more comprehensive study on including passive elements. The study conducted in Chapter 4 was limited to only open-cicuits, short-circuits or loads, but any values between these ranges can be considered. Similar works regarding including passive elements can be found in [53].

While paraboloid reflector antenna are well known and understood, they are not necessarily optimal for beamscanning. In the context of resolving satellites along the GEO arc, future studies could look to optimize reflector shape to obtain a much larger scan range, covering multiple satellites across the arc.

Finally, the investigation conducted in Chapter 5 has shown just one of the many possible parameter studies that can be conducted with the numerical tools developed during this thesis. It is believe that many future projects could benefit from the model.

Appendices

Appendix A

FEKO Lua Scripts

An efficient workflow was made possible by creating various Lua scripts for FEKO. These scripts are reviewed here.

A.1 setupEEP.lua

This script is a somewhat modified version of a script found in the "Multi-port post-processing" plug-in from FEKO [23]. Its purpose is to set-up the required simulation configurations to obtain the scattering parameters and EEPs of a multi-port array. The script can be run on any CADFEKO model which adhered to the following restrictions:

- Only one *Standard configuration* must be present.
- More than one port must be defined.
- Ports must be either of `WirePort`, `Edge Port` or `MicrostripPort` type [38]
- No loads or sources need be included
- A single far-field request must be specified across an angular region of interest.

When executed, it creates an *S-parameter configuration* which includes all ports, with default 50 Ω reference impedances, and with the '*Restore loads after calculation*' option unchecked. Additionally, it creates a separate *Standard configuration* for each element, with a unit voltage source applied to the corresponding element and zero voltage sources on all other elements, and duplicates the requestesd *Far-field* data points to each configuration. The option of exporting the far field `.ffe` is also enabled[1]. If the model has been meshed

[1]This allows easy importing of the simulated primrary embedded element patterns as equivalent point sources when running the `setupREFL.lua` script discussed in Section A.2

properly, the simulation is run.

The *S-parameter configuration* is simulated first, and FEKO automatically adds the reference impedances (50Ω) on all ports. A full MoM matrix calculation and LU-decomposition is carried out in order to calculated the S-parameters. The *N Standard configurations* are simulated afterwards, and each configuration necessitates only a change on the excitation side of the MoM equation. By not restoring the loads after the *S-parameter configuration* execution, the already decomposed MoM matrix can be re-used in calculating the each EEP of the array [38, see section 14.68]. Essentially, the EEPs with unit value Thevenin sources (see Section 2.4) are simulated, with 50 Ω generator impedances.

A.2 setupREFL.lua

This script can be run on a CADFEKO model after it has been simulated according to the `setupEEP.lua` script discussed in the previous section. The script is used to rapidly set-up the EEPs from `setupEEP.lua` as equivalent point source.

When running `setupREFL.lua`, the current CADFEKO model is saved to a new file as `PRJOECTNAME_REFL.cfx`. Next, the existing *S-parameter configuration* as well as all the model geometry is deleted. Finally, the EEPs, which were simulated by `setupEEP.lua`, are important as equivalent point sources, and each point source is assigned to its corresponding *Standard configuration*.

In summary, once the script is completed, the user is left with CADFEKO model containing no geometry, and *N Standard configuration*s, where each each configuration contains a corresponding EEP applied as an equivalent point source. A reflector geometry can be constructed in order to simulate the secondary EEPs.

A.3 exportDataSet.lua

This script can be run in POSTFEKO on a `.fek` file produced after simulating a CADFEKO model (.cfx file) according to `setupEEP.lua`. The `exportDataSet.lua` script produces a dialog which requests the directory for exporting the following files:

- A `.ffe` file for each embedded element pattern simulated, labelled as `PRJOECTNAME_EEP_n.ffe`, where `n` is the corresponding element index
- A `.sNp` Touchstone file containing the simulated N-port scattering-parameters

- A `.txt` file (`EEP_PRIMARY.txt`). The first line contains the number of ports simulated, followed by lines which simply contain the file names of the above mentioned `.ffe` and `.sNp` files

All files are then saved to the same directory. The text file `EEP_PRIMARY.txt` can be helpful when using third-party software, such as MATLAB, to read the FEKO results for further post-processing.

Appendix B

Figures of Merit for Active Receiving Arrays

The IEEE standards and definitions for antennas [15] has recently been updated with terms specifically used for characterizing active receiving arrays. These will only be briefly discussed in the context of notation used in this thesis, and the interested reader is referred to [31] and references therein for a comprehensive description of the terms, and to [54] for an official summary of the newly added terms.

The crux of these new terms lies with the *isotropic noise response* of the array receiver, defined as:

isotropic noise response [15], $P_{\mathrm{t,iso}}$**:** *For a receiving active-array antenna, the noise power at the output of a formed beam with a noiseless receiver when in an environment with a brightness temperature distribution that is independent of direction and in thermal equilibrium with the antenna.*

The noise correlation matrix of isotropic noise response at the receiver output can be labelled $\mathbf{R}_{\mathrm{t,iso}}$ [31]. From Section 3.2.2 and with the help of Bosma's theorem [55] for noise waves propagating from a passive multi-port at uniform temperature T_{iso}, $\mathbf{R}_{\mathrm{t,iso}}$ can be expressed as

$$\mathbf{R}_{\mathrm{t,iso}} = Z_o k_b B T_{\mathrm{iso}} \mathbf{T}(\mathbf{U} - \mathbf{S}_{\mathrm{A}}\mathbf{S}_{\mathrm{A}}^{\dagger})\mathbf{T}^{\dagger} \tag{B.1}$$

Equation (B.1) can be seperated into two contributions, namely,

$$\mathbf{R}_{\mathrm{t,iso}} = \mathbf{R}_{\mathrm{ext,iso}} + \mathbf{R}_{\mathrm{loss}} \tag{B.2}$$

where $\mathbf{R}_{\mathrm{loss}}$ is due to noise generated from the actual antenna array losses at a physical temperature T_{iso}, while $\mathbf{R}_{\mathrm{ext,iso}}$ is due to the external isotropic brightness temperature T_{iso}. With the help of equation (3.21), $\mathbf{R}_{\mathrm{ext,iso}}$ can be expressed as,

$$\mathbf{R}_{\mathrm{ext,iso}} = 8 Z_o k_b B T_{\mathrm{iso}} \mathbf{T}\mathbf{A}_{oc}\mathbf{T}^{\dagger} \tag{B.3}$$

where $\mathbf{A}_{oc}$ denotes the overlap integral matrix of the OC-EEPs [40, 26]

$$\mathbf{A}_{oc} = \frac{1}{2\eta} \iint_{\Omega_o} [\vec{\boldsymbol{f}}_m^{oc} \cdot \vec{\boldsymbol{f}}_n^{oc^*}] d\Omega_o \tag{B.4}$$

. The isotropic noise response is then calculated from $\mathbf{R}_{\mathrm{t,iso}}$ as,

$$P_{\mathrm{t,iso}} = \mathbf{w}^{\dagger} \mathbf{R}_{\mathrm{t,iso}} \mathbf{w} \tag{B.5}$$

From the isotropic noise response, the *active antenna available gain* can be defined;

active antenna available gain [15], $G_{\mathrm{rec}}^{\mathrm{av}}$**:** *For a receiving active array antenna, the ratio of the isotropic noise response to the available power at the terminals of any passive antenna over the same bandwidth and in the same isotropic noise environment.*

The available power (power into a conjugate matched load) for any passive antenna immersed in T_{iso} is $k_b T_{\mathrm{iso}} B$ [35], and so it follows that,

$$G_{\mathrm{rec}}^{\mathrm{av}} = \frac{P_{\mathrm{t,iso}}}{k_b T_{\mathrm{iso}} B} \tag{B.6}$$

Qualitatively, normalizing the beamformer output by the active antenna available gain $G_{\mathrm{rec}}^{\mathrm{av}}$ serves to remove arbitrary gain factors from the receiver chains, even if those chains include different amplifier gains, mixer conversion losses, or analog-to-digital conversion factors. It allows any power quantity at the beamformer output to be defined as an equivalent available power, as though it were referred to input of an equivalent single-port antenna [54].

Without providing further details, the relevant figures of merit which are used throughout the thesis are defined below for the reader's convenience.

System Noise Parameters

Beam equivalent receiver noise temperature:

$$T_{\mathrm{rec}} = T_{\mathrm{iso}} \frac{P_{\mathrm{rec}}}{P_{\mathrm{t,iso}}} \tag{B.7}$$

where P_{rec} is beamformer output receiver noise power.

Beam equivalent external noise temperature:

$$T_{\mathrm{ext}} = T_{\mathrm{iso}} \frac{P_{\mathrm{ext}}}{P_{\mathrm{ext,iso}}} \tag{B.8}$$

where P_{ext} is beamformer output external brightness temperature noise power.

Beam equivalent system noise temperature:

$$T_{\text{sys}} = T_{\text{iso}} \frac{P_{\text{n}}}{P_{\text{t,iso}}} \tag{B.9}$$

where P_n is the noise power due to all noise sources.

System Gain Parameters

Aperture efficiency:

$$\eta_{ap} = \frac{k_b T_{\text{iso}} B}{A_p S_{\text{sig}}} \frac{P_{\text{sig}}}{P_{\text{ext,iso}}} \tag{B.10}$$

where A_p is the physical area of the aperture antenna, and S_{sig} is the power flux density of polarization matched plane-wave incident from the direction of interest.

Radiation efficiency:

$$\eta_{rad} = \frac{P_{\text{ext,iso}}}{P_{\text{t,iso}}} \tag{B.11}$$

Beam equivalent antenna gain:

$$G = \eta_{rad} \eta_{ap} \frac{4\pi A_p}{\lambda^2} \tag{B.12}$$

Bibliography

[1] M. V. Ivashina, M. N. M. Kehn, P. S. Kildal, and R. Maaskant, "Decoupling efficiency of a wideband vivaldi focal plane array feeding a reflector antenna," *IEEE Transactions on Antennas and Propagation*, vol. 57, pp. 373–382, Feb 2009.

[2] A. Mrstik and P. Smith, "Scanning capabilities of large parabolic cylinder reflector antennas with phased-array feeds," *IEEE Transactions on Antennas and Propagation*, vol. 29, pp. 455–462, May 1981.

[3] R. Assaly and L. Ricardi, "A theoretical study of a mulit-element scanning feed system for a parabolic cylinder," *IEEE Transactions on Antennas and Propagation*, vol. 14, pp. 601–605, September 1966.

[4] K. F. Warnick, R. Maaskant, M. V. Ivashina, D. B. Davidson, and B. D. Jeffs, "High-sensitivity phased array receivers for radio astronomy," *Proceedings of the IEEE*, vol. 104, pp. 607–622, March 2016.

[5] R. D. Shaw, "Phased array feed development for askap, with the benefit of hindsight," in *2017 11th European Conference on Antennas and Propagation (EUCAP)*, pp. 3832–3836, March 2017.

[6] W. A. van Cappellen and L. Bakker, "Apertif: Phased array feeds for the westerbork synthesis radio telescope," in *2010 IEEE International Symposium on Phased Array Systems and Technology*, pp. 640–647, Oct 2010.

[7] R. Maaskant, D. J. Bekers, M. J. Arts, W. A. van Cappellen, and M. V. Ivashina, "Evaluation of the radiation efficiency and the noise temperature of low-loss antennas," *IEEE Antennas and Wireless Propagation Letters*, vol. 8, pp. 1166–1170, 2009.

[8] R. Maaskant, E. E. M. Woestenburg, and M. J. Arts, "A generalized method of modeling the sensitivity of array antennas at system level," in *34th European Microwave Conference, 2004.*, vol. 3, pp. 1541–1544, Oct 2004.

[9] C. Craeye, B. Parvais, and X. Dardenne, "Mom simulation of signal-to-noise patterns in infinite and finite receiving antenna arrays," *IEEE Transactions on Antennas and Propagation*, vol. 52, pp. 3245–3256, Dec 2004.

[10] M. N. M. Kehn and L. Shafai, "Characterization of dense focal plane array feeds for parabolic reflectors in achieving closely overlapping or widely separated multiple beams," *Radio Science*, vol. 44, pp. 1–25, June 2009.

[11] A. N. Plastikov, "A high-gain multibeam bifocal reflector antenna with 40 field of view for satellite ground station applications," *IEEE Transactions on Antennas and Propagation*, vol. 64, pp. 3251–3254, July 2016.

[12] S. G. Hay, S. J. Barker, C. Granet, A. R. Forsyth, T. S. Bird, M. A. Sprey, and K. J. Greene, "Multibeam earth station antenna for an european teleport application," in *IEEE Antennas and Propagation Society International Symposium. 2001 Digest. Held in conjunction with: USNC/URSI National Radio Science Meeting (Cat. No.01CH37229)*, vol. 2, pp. 300–303 vol.2, July 2001.

[13] C. K. Hansen, K. F. Warnick, B. D. Jeffs, J. R. Fisher, and R. Bradley, "Interference mitigation using a focal plane array," *Radio Science*, vol. 40, pp. 1–13, Oct 2005.

[14] P.-S. Kildal, *Foundations of Antenna Engineering - A Unified Approach for Line-Of-Sight and Multipath.* Gothenburg: Kildal Antenn AB, 1 ed., 2015.

[15] "IEEE standard for definitions of terms for antennas," *IEEE Std 145-2013 (Revision of IEEE Std 145-1993)*, pp. 1–50, March 2014.

[16] P. S. Kildal, "Factorization of the feed efficiency of paraboloids and cassegrain antennas," *IEEE Transactions on Antennas and Propagation*, vol. 33, pp. 903–908, Aug 1985.

[17] R. Collin, "Aperture efficiency for paraboloidal reflectors," *IEEE Transactions on Antennas and Propagation*, vol. 32, pp. 997–1000, Sep 1984.

[18] K. F. Warnick, "Antenna Efficiency and the Genius of the IEEE Standard for Antenna Terms [Education Column]," *IEEE Antennas and Propagation Magazine*, vol. 54, pp. 236–237, Aug 2012.

[19] C. Balanis, *Antenna theory : Analysis and Design.* Hoboken, NJ: Wiley Interscience, 2005.

[20] P. J. B. Clarricoats and G. T. Poulton, "High-efficiency microwave reflector antennas - a review," *Proceedings of the IEEE*, vol. 65, pp. 1470–1504, Oct 1977.

[21] H. C. Minnett and B. M. Thomas, "Fields in the image space of symmetrical focusing reflectors," *Electrical Engineers, Proceedings of the Institution of*, vol. 115, pp. 1419–1430, October 1968.

[22] W. Watson, "The field distribution in the focal plane of a paraboloidal reflector," *IEEE Transactions on Antennas and Propagation*, vol. 12, pp. 561–569, September 1964.

[23] Altair HyperWorks, FEKO. `https://www.feko.info/`. Accessed: 2017-09.

[24] D. B. Hayman, T. S. Bird, K. P. Esselle, and P. Hall, "Encircled power study of focal plane field for estimating focal plane array size," in *2005 IEEE Antennas and Propagation Society International Symposium*, vol. 3A, pp. 371–374 vol. 3A, July 2005.

[25] A. Zamanifekri and A. B. Smolders, "Optimum configuration of focal plane arrays for satellite communication," in *2013 IEEE Antennas and Propagation Society International Symposium (APSURSI)*, pp. 952–953, July 2013.

[26] C. Craeye and D. González-Ovejero, "A review on array mutual coupling analysis," *Radio Science*, vol. 46, pp. 1–25, April 2011.

[27] P.-S. Kildal, "Equivalent circuits of receive antennas in signal processing arrays," *Microwave and Optical Technology Letters*, vol. 21, no. 4, pp. 244–246, 1999.

[28] S. Searle, *Matrix algebra useful for statistics*. New York: Wiley, 1982.

[29] D. I. L. de Villiers. Private communication.

[30] R. Monzingo, *Introduction to adaptive arrays*. Raleigh, NC: SciTech Pub, 2011.

[31] K. F. Warnick, M. V. Ivashina, R. Maaskant, and B. Woestenburg, "Unified definitions of efficiencies and system noise temperature for receiving antenna arrays," *IEEE Transactions on Antennas and Propagation*, vol. 58, pp. 2121–2125, June 2010.

[32] H. Trees, *Optimum array processing*. New York: Wiley-Interscience, 2002.

[33] F. Gross, *Smart antennas with MATLAB*. New York: McGraw-Hill Education, 2015.

[34] M. V. Ivashina, O. Iupikov, R. Maaskant, W. A. van Cappellen, and T. Oosterloo, "An optimal beamforming strategy for wide-field surveys with phased-array-fed reflector antennas," *IEEE Transactions on Antennas and Propagation*, vol. 59, pp. 1864–1875, June 2011.

[35] D. M. Pozar, *Microwave Engineering*. Wiley, 4 ed., 2011.

[36] J. J. Lee, "G/t and noise figure of active array antennas," *IEEE Transactions on Antennas and Propagation*, vol. 41, pp. 241–244, Feb 1993.

[37] E. Brookner, "Active-phased-array system noise temperature," in *2008 IEEE Radar Conference*, pp. 1–6, May 2008.

[38] Altair, HyperWorks, *User Manual for FEKO 14.0*.

[39] D. J. Ludick, R. Maaskant, D. B. Davidson, U. Jakobus, R. Mittra, and D. de Villiers, "Efficient analysis of large aperiodic antenna arrays using the domain green's function method," *IEEE Transactions on Antennas and Propagation*, vol. 62, pp. 1579–1588, April 2014.

[40] K. F. Warnick and B. D. Jeffs, "Efficiencies and system temperature for a beamforming array," *IEEE Antennas and Wireless Propagation Letters*, vol. 7, pp. 565–568, 2008.

[41] M. V. Ivashina, R. Maaskant, and B. Woestenburg, "Equivalent system representation to model the beam sensitivity of receiving antenna arrays," *IEEE Antennas and Wireless Propagation Letters*, vol. 7, pp. 733–737, 2008.

[42] K. F. Warnick and M. A. Jensen, "Optimal noise matching for mutually coupled arrays," *IEEE Transactions on Antennas and Propagation*, vol. 55, pp. 1726–1731, June 2007.

[43] R. Maaskant, *Analysis of Large Antenna Systems*. PhD thesis, Eindhoven University of Technology, Eindhoven, Netherlands, 2010.

[44] S. W. Wedge and D. B. Rutledge, "Wave techniques for noise modeling and measurement," *IEEE Transactions on Microwave Theory and Techniques*, vol. 40, pp. 2004–2012, Nov 1992.

[45] J. Dobrowolski, *Computer-aided analysis, modeling, and design of microwave networks : the wave approach*. Boston, Mass.: Artech House, 1996.

[46] D. I. L. de Villiers and R. Lehmensiek, "Rapid calculation of antenna noise temperature in offset gregorian reflector systems," *IEEE Transactions on Antennas and Propagation*, vol. 63, pp. 1564–1571, April 2015.

[47] K. F. Warnick, B. D. Jeffs, J. Landon, J. Waldron, D. Jones, J. R. Fisher, and R. Norrod, "Beamforming and imaging with the BYU/NRAO L-band 19-element phased array feed," in *2009 13th International Symposium on Antenna Technology and Applied Electromagnetics and the Canadian Radio Science Meeting*, pp. 1–4, Feb 2009.

[48] D. A. Jones, K. F. Warnick, B. D. Jeffs, J. Landon, J. Waldron, J. R. Fisher, and R. Norrod, "Modeled and measured mutual impedances, element patterns, and sensitivity for a 19 element focal plane array," in *2008 IEEE Antennas and Propagation Society International Symposium*, pp. 1–4, July 2008.

[49] M. W. Pospieszalski, "Interpreting transistor noise," *IEEE Microwave Magazine*, vol. 11, pp. 61–69, Oct 2010.

[50] J. P. Weem and Z. Popovic, "A method for determining noise coupling in a phased array antenna," in *2001 IEEE MTT-S International Microwave Sympsoium Digest (Cat. No.01CH37157)*, vol. 1, pp. 271–274 vol.1, May 2001.

[51] R. Maaskant and E. E. M. Woestenburg, "Applying the active antenna impedance to achieve noise match in receiving array antennas," in *2007 IEEE Antennas and Propagation Society International Symposium*, pp. 5889–5892, June 2007.

[52] K. F. Warnick, B. Woestenburg, L. Belostotski, and P. Russer, "Minimizing the noise penalty due to mutual coupling for a receiving array," *IEEE Transactions on Antennas and Propagation*, vol. 57, pp. 1634–1644, June 2009.

[53] R. Mehmood and J. W. Wallace, "Exploring beamforming performance versus complexity in reconfigurable aperture antennas," in *2010 International ITG Workshop on Smart Antennas (WSA)*, pp. 383–389, Feb 2010.

[54] K. F. Warnick, M. Ivashina, R. Maaskant, and B. Woestenburg, "Noise-based antenna terms for active receiving arrays," in *Proceedings of the 2012 IEEE International Symposium on Antennas and Propagation*, pp. 1–2, July 2012.

[55] H. Bosma, "On the theory of linear noisy systems," *Philips Research Reports Supplement*, no. 10, pp. 1–189, 1967.